8-24-2011

Development of a High Strain-Rate Constitutive Model for Sands and its Application in Finite Element Analysis of Tunnels Subjected to Blast

William T. Higgins IV
University of Connecticut - Storrs, wthigginsiv@gmail.com

Development of a High Strain-Rate Constitutive Model for Sands and its Application in Finite Element Analysis of Tunnels Subjected to Blast

William Higgins

B. S., University of Connecticut

A Thesis

Submitted in Partial Fulfillment of the
Requirements for the
Degree of
Master of Science in Civil Engineering
at the

University of Connecticut
August 2011

APPROVAL PAGE

Master of Science Thesis

Development of a High Strain-Rate Constitutive Model for Sands and its Application in Finite Element Analysis of Tunnels Subjected to Blast

Presented by

William Higgins, B. S.

Major Advisor _____
Prof. Dipanjan Basu, Ph. D.

Associate Advisor _____
Prof. Michael Accorsi, Ph. D.

Associate Advisor _____
Prof. Ramesh Malla, Ph. D.

University of Connecticut
2011

ACKNOWLEDGEMENT

I would like to acknowledge the Department of Homeland Security for the funding for this research. Thanks to my Major Advisor Dr. Dipanjan Basu and my Associate advisors Dr. Ramesh Malla and Dr. Micheal Accorsi. Thanks to everyone in this research; Dr. Dipanjan Basu, Dr. Tanusree Chakraborty, and Mr. Harry Martindale.

William Higgins

Department of Civil and Environmental Engineering
University of Connecticut

Wthigginsiv@gmail.com

August 15, 2011

TABLE OF CONTENTS

ABSTRACT vi
CHAPTER 1 - RATE DEPENDENCE OF SAND: AN OVERVIEW 1
1.0 Introduction 1
1.1 Soil Constitutive Models 2
1.1.1 Rate Independent Models 2
1.1.2 Rate Dependent Models 3
1.2 Effect of Strain Rate on Sand Behavior 5
1.2.1 Testing Methods 5
1.2.2 Rate Effects on Sand 6
1.2.3 Mechanics of Rate Effects 6
1.3 Blast and High Strain-Rate Experimentation 7
1.4 Simulations of Blast in Soil 7
1.5 Scope and Organization of Thesis 8
CHAPTER 2 - CONSTITUTIVE MODEL 10
2.0 Introduction 10
2.1 Formulation of Constitutive Model 10
2.1.1 Application of Critical State Soil Mechanics Concepts 10
2.1.2 Yield Surface 12
2.1.3 Critical State Surface 17
2.1.4 Bounding Surface 19
2.1.5 Dilatancy Surface 20
2.1.6 Stress-Strain Relationship 20
2.1.7 Elastic and Plastic Strains 21
2.1.8 Interaction of Model Surfaces 26
2.2 Cutting Plane Algorithm and Extension to Viscoplasticity 27
2.2.1 Elastic-Plastic Formulation of Cutting Plane Algorithm 28

2.2.2 Modification of Cutting Plane Algorithm for Viscoplasticity 34
2.3 Hierarchy of Algorithms and Error Control 42
2.4 Calibration and Validation 43
2.4.1 Simulation of Triaxial Tests 47
2.4.2 Simulation of SHPB Tests 52
2.5 Conclusions 56
CHAPTER 3 - ANALYSIS OF TUNNELS SUBJECTED TO BLAST 58
3.0 Introduction 58
3.1 Details of Simulation 58
3.2 Results 69
3.2.1 Temporal and Spatial Variation of Stresses and Displacements 69
3.2.2 Effect of Soil Type 74
3.2.3 Effect of Tunnel Depth 83
3.3 Conclusions 89
CHAPTER 4 - RESEARCH SUMMARY AND FUTURE DIRECTIONS 90
4.1 Research Summary 90
4.2 Future Directions 91
REFERENCES 93
APPENDIX A - SPLIT HOPKINSON PRESSURE BAR TEST 110
APPENDIX B - OVERSTRESS FUNCTION 117
APPENDIX C - ERROR CONTROL ALGORITHM 119

ABSTRACT

This thesis describes the development of a constitutive model for simulating the high strain-rate behavior of sands and demonstrates the use of the model by analyzing underground tunnels subjected to blast. The constitutive model is based on the concepts of the critical state soil mechanics and bounding surface plasticity theory. The model captures the behavior of sand under multi-axial loading conditions and predicts both drained and undrained behavior at small and large strains. Perzyna's overstress theory is incorporated in the model to simulate the viscoplastic behavior of sand under high strain rate. The model follows a nonassociated flow rule.

The model parameters are determined for Ottawa and Fontainebleau sands from the available experimental data of rate-independent triaxial compression test and split Hopkinson pressure bar test. The model is implemented in the finite element software Abaqus through user defined material subroutines. Finite element simulations of the split Hopkinson pressure bar experiments on Ottawa and Fontainebleau sands are performed in which the maximum axial strain rate was 2000/sec. These simulations demonstrate the model's ability to capture the high strain-rate behavior of sands.

Subsequently, finite element analyses of tunnels embedded in sandy soils and subjected to internal blast loading are performed using Abaqus in which the developed

constitutive model is used. Blast induced pressure loading, simulated with the JWL explosive material model, is applied on the internal tunnel boundary. The effects of soil type, depth of tunnel and quantity of explosive on the blast induced stresses, strains and deformations in the soil surrounding the tunnel are investigated. These analyses demonstrate the use of the constitutive model in the study of soil-structure interaction problems under blast induced dynamic loading.

CHAPTER 1 - RATE DEPENDENCE OF SAND: AN OVERVIEW

1.0 Introduction

The development of sustainable and resilient civil infrastructure requires that structures can not only withstand anticipated design loads but also encounter extreme and unanticipated loads with minimal endangerment of individuals and properties. Extreme loading can be caused by nature in the form of tornados, tsunamis, earthquakes or other natural disasters, or be caused by human activities such as bomb blasts, collisions or industrial accidents. A common feature of these extreme loading scenarios is that they can create very large strains in the surrounding material in a very short period of time. Because so many structures interact with soil which is the weakest of all civil engineering materials, it is necessary to be able to model the effect of these extreme, high-rate loads on soil.

In this thesis, a constitutive model is developed for sand that can simulate the high strain-rate behavior of sands under multi-axial loading conditions. The constitutive model is subsequently integrated in a finite element framework and the response of tunnels embedded in sandy soils and subjected to blast loads is studied.

1.1 Soil Constitutive Models

1.1.1 Rate Independent Models

In the early days of soil constitutive modeling, the most widely used models were the Drucker-Prager model (Drucker and Prager 1952) and Mohr-Coulomb model. These models have a single yield surface involving a relationship between the shear stress and the mean stress. When the stress state reaches this yield surface, the material strains plastically. Developments in the modeling of soil at Cambridge University in the 1950s led to the development of the Cam-Clay and Modified-Cam-Clay models. These models were based on the concepts of the critical state soil mechanics (Roscoe et al. 1958, Roscoe and Burland 1968). These models could be calibrated to account for the nonlinear relationship between the volumetric stresses and strains experienced during loading and unloading of a soil. Several models have been developed by modifying the Modified-Cam-Clay model. CASM (Clay and Sand Model) (Yu 1998) is one such model which modified the use of the calculation of the distance from the current to the critical state void ratios in order to better capture the different behaviors of contractive and dilative soil specimen.

Another important advancement in the constitutive modeling of soils was the development of the bounding-surface and other multi-surface models. The bounding surface plasticity theory was developed by Dafalias and Popov (1975) and Krieg (1975) to model metal plasticity. The concept was later extended for use in soil by Dafalias and Herman (1982). Several multi-surface models have since been developed based on the work of Dafalias for simulating soil behavior (Loukidis 2006, Chakraborty 2009, Manzari and Dafalias 1997, Martindale 2011). These models can realistically simulate

the nonlinear pre-peak behavior and the post-peak behavior up to the critical state. This is a distinct improvement over the single yield surface models (e.g., Mohr-Coulomb and Cam-Clay models), which generally assume the pre-yield behavior to be elastic.

1.1.2 Rate Dependent Models

The early rate-dependent models for soils were developed to simulate creep and stress relaxation primarily for modeling foundation settlement. These low strain-rate models were typically rheological (springs, viscous dashpots and sliders) or empirical in nature (Murayama and Shibata 1958, Christensen and Wu 1964, Abdel-Hady and Herrin 1966). However these models were seldom able to capture the multi-axial behavior needed for the accurate simulation of field boundary value problems. More advanced models based on these methods were later developed that were capable of simulating the creep and stress relaxation behavior of sand (Borja and Kavanzanjiian 1985, Hsieh et al. 1990, Borja et al.1990, Borja 1992, Tatsuoka et al. 2000 and 2002, Cristescu 1991, Di Bendetto et al. 2002, Boukpeti et al. 2002 and 2004).

Viscoplasticity has also been used to simulate the rate effects in soil. A rigorous way of incorporating viscous behavior into constitutive models is the use of Perzyna's overstress theory (Perzyna 1963, 1966). In viscoplasticity, the stress state extends beyond the yield surface during loading. According to Perzyna's overstress theory, an overstress function can be defined based on the distance of the stress point beyond the yield surface. This overstress governs the time dependant straining of the material. This approach has been used in numerous soil constitutive models (Oka and Adachi 1985, Desai and Zhang 1987, Adachi et al. 1987, 1990, 1996, 1997, Oka et al. 1994, 2002 and 2004, di Prisco and Imposimato 1996, 2003, di Prisco et al. 2000, 2002, Zienkiewicz and

Cormeau 1974, Adachi and Okano 1974, Zienkiewicz et al. 1975, Adachi and Oka 1982a, 1982b, Dafalias 1982, Oka et al. 1988, Kaliakin 1985, Kaliakin and Dafalias 1990a, 1990b,1991, Kutter and Sathialingam 1992, Tong and Tuan 2007).

Viscous behavior in soil models has also been achieved through the nonstationary flow surface theory (Naghdi and Murch 1963, Olszak and Perzyna 1966a, 1966b, 1970). In the flow surface theory, a nonassociated plastic potential surface moves based on the changes in the stress and stress history. This theory did not gain much popularity because it required the knowledge of the stress history of the soil, which creates difficulties in the simulation of boundary value problems.

Recently, a few constitutive models have been developed specifically for the purpose of simulating high strain-rate behavior of soil. One approach considers a three-phase model for the soil solids, air and water, which accounts for the different wave speeds in the different materials (Wang 2004, Laine and Sandvik 2001). A common feature in these models is the incorporation of the strain rate effects by creating the direct dependence of a model parameter on the strain rate. Wang (2004) created a three phase model using the Drucker-Prager yield condition for the solid phase — the yield surface in this model is directly dependent on the strain rate. Sekiguchi (1984) created a free flow surface model in which the yield surface grows with the strain rate. A common way of incorporating the strain rate into models for clays is to make the undrained shear strength a direct function of the strain rate (Zhou and Randolph 2007, Jung and Biscontin 2006, Mitchel and Soga 2005, Einav and Randolph 2005). The shortfall of adjusting the undrained shear strength is that the effect multi-axial loading on clay cannot be properly captured. Recent models by Chakraborty (2009) and Martindale (2011) incorporated the

rate effects into a two-surface plasticity model (Manzari and Dafalias 1997, Dafalias et al. 2004) by allowing the critical state line to translate with the strain rate.

1.2 Effect of Strain Rate on Sand Behavior

1.2.1 Testing Methods

Various testing apparatus have been used to study the transient behavior of soil — these include devices based on pendulums on springs, weights on dashpots, or oil under thermal expansion (Cassagrande and Shannon 1948). Yamamuro and Lade (1993) used high speed camera to capture the movements of soil samples reacting to weights dropped on them. By analyzing the photographs, the displacement and deceleration of the weight could be measured, and thus, the load on the sample could be calculated.

Before the use of computers, most testing methods were load controlled — only the applied pressure or the energy imparted on the soil sample could be decided by the experimenter. Thus, the strain rate, which is dependent on the mechanical properties of soil, could not be directly controlled. But with the development of computer controlled loading rigs, the applied load can be controlled to generate the strain rate prescribed by the experimenter (Sheahan 1991).

In order to create very large strain rates, of the order 1000 per second, researchers often use projectile methods. An example of such high-rate experimental apparatus is the split Hopkinson pressure bar (Kolksy 1948) in which a compression wave is generated by the collision of a projectile on a bar that transmits the energy to the sample. The split Hopkinson pressure bar test is described in greater detail in appendix A.

1.2.2 Rate Effects on Sand

The principal observation of the effect of strain rates on sand is that the faster the strain rate is the greater the strength is (Lee et al. 1969, Seed and Lundgren 1954, Whitman and Healy 1962, Yamamuro and Abrantes 2003, Cassagrande and Shannon 1948). The increase in strength is manifested through an increase in the peak strength and initial stiffness (Lee et al.1969). The peak stress also occurs at a lesser value of strain as the applied rate of strain increases. This effect of increased strength and stiffness is more pronounced in samples with greater relative density and confining stress (Lee et al. 1969, Seed and Lundgren 1954, Whitman and Healy 1962, Yamamuro and Abrantes 2003).

1.2.3 Mechanics of Rate Effects

As soil shears, there are different mechanisms of movement activated within the soil, namely, sliding/rolling friction, dilation and particle crushing. Friction develops as adjacent particles slide or roll over each other and some amount of energy is dissipated in the process. Soil dilates as particles shear over other particles and dissipates more energy than sliding. Particle crushing occurs when adjacent particles are not able to move over each other and the particles are fractured in order to allow for movement. Particle crushing consumes the most energy out of all these mechanisms.

Particle crushing is more prevalent in tests conducted at higher strain rates. Nash and Dixon (1961) observed sudden jumps in the stress-strain plots which they suspected were due to mass particle collapse. These sudden jumps appeared to be more concentrated in faster tests. They conjectured that, rather than the occasional mass particle failure that occurs in slow tests, the soil was not able to dilate quickly enough in faster tests. Slow dilation at faster rates led to a constant pulse of crushing failures.

Similar results were reported in Lee et al. (1969). They conducted a series of undrained one dimensional compression tests on K_0 consolidated specimens (K_0 is the coefficient of earth pressure at rest) with and without transient loading. Lee et al. (1969) found that, as the loads were varied with time, the pore pressure remained constant although there were significant changes in the axial strain. Because the pore pressure remained unchanged, Lee et al. (1969) concluded that dilation was not responsible for the change in the strain — the change must have been caused by increased particle crushing.

1.3 Blast and High Strain-Rate Experimentation

The testing of soil under high strain rates is often dependent on blast and projectile methods. The centrifuge test is a common way of scaling down the use of explosives so that dangerous and expensive experiments can be avoided yet the desired results are obtained. Several researchers have conducted centrifuge tests on scaled models of underground tunnels subjected to blast on the soil surface (Holsapple and Schmidt 1980 and 1982, Schmidt and Holsapple 1980, Kutter et al. 1988, Preece et al. 1998, Charlie et al. 2005, De and Zimmie 2006, 2007, and De 2008). The effect of shockwaves caused by buried explosives on buried structures was studied by Davies (1994). The penetration of projectiles into soil was also studied using centrifuges (Fragaszy and Taylor 1991, Zelikson et al. 1986, Savvidou and Schofield 1986).

1.4 Simulations of Blast in Soil

There is a scarcity of published results on the boundary value problems involving blast loading in/on soil. The loading from explosive blasts are often simulated using the Jones-Wilkens-Lee (JWL) model (Lee et al. 1973). Nagy et al. (2010) used the finite

element method along with the JWL model to simulate the wave propagation through soil to a buried concrete structure due to an explosion on the ground surface. In their analysis, Nagy et al. (2010) simulated the soil behavior using the Drucker-Prager model. Yang et al. (2010) simulated the propagation of blast in soil using a single surface soil plasticity model of Krieg (1972). Lu et al. (2005) simulated blast propagating through soil with a coupled three phase analysis. They used a modified, non-viscous Drucker-Prager model with a yield surface that expands with strain rate and coupled it with a rheological damage model. Bessette (2008) compared test data from experiments on the propagation of blast from buried C4 explosive material with simulations performed by using the JWL model to simulate blast and a three-phase model to simulate the soil behavior. Fedgun et al. (2008a, 2008b) and Karinski et al. (2008) used the variational difference method to study underground tunnels and cavities subjected to blast loading.

1.5 Scope and Organization of Thesis

In this thesis, a constitutive model is developed for simulating the high strain-rate behavior of sand. The model is calibrated to simulate the behavior of Ottawa sand and Fontainebleau sands and is verified by simulating triaxial compression and split Hopkinson pressure bar tests. The constitutive model is then implemented in a finite element software and underground tunnels subjected to blast are analyzed.

The thesis is presented in four chapters and three appendices. Chapter 2 discusses the details and calibration of the constitutive model. Chapter 3 discusses the finite element analyses of tunnels under blast loads. Chapter 4 contains a research summary and a discussion of possible future work on this topic. Appendix A gives a detailed description of the split Hopkinson pressure bar test. Appendices B and C discuss the

overstress function and the error control algorithm used in the formulation of the constitutive model.

CHAPTER 2 - CONSTITUTIVE MODEL

2.0 Introduction

The sand constitutive model developed in this study is based on the concepts of the bounding surface plasticity theory, Perzyna's overstress theory of viscoplasticity and the critical state soil mechanics. The model is formulated in a multi-axial stress space that is appropriate for generalized loading conditions. It is calibrated for Ottawa and Fontainebleau sands based on the results of a variety of laboratory tests that include the triaxial compression test and the split Hopkinson pressure bar test.

2.1 Formulation of Constitutive Model

2.1.1 Application of Critical State Soil Mechanics Concepts

This model is based on critical state soil mechanics. The critical state is representative of a state where soil can shear without any change in volumetric strain under drained loading or in pore pressure under undrained loading. The critical state of a soil can be determined by conducting triaxial tests at various initial void ratios and confining pressures. When the pore pressure or volumetric strain stabilizes in a certain test, a point can be located in terms of the equilibrium void ratio e and the corresponding effective mean stress p' in the e-p' space [$p' = (\sigma_{11}' + \sigma_{22}' + \sigma_{33}')/3$ where σ_{ij}' is the effective stress tensor]. A line joining all the equilibrium points in the e-p' space represents the

critical state line. Traditionally this line is plotted in terms of the log of p' (Been and Jefferies 1985). However, in this study, a power law relating the critical state e and p' is chosen, as was done in Loukidis (2006), because it provides a better description of the critical state line (Li and Wang 1998):

$$e_c = \Gamma - \lambda \left(\frac{p'}{p_a} \right)^{\zeta} \tag{2.1}$$

where e_c is the void ratio at the critical state as illustrated in Figure 2.1 and p_a is the atmospheric pressure. The parameter Γ is the intercept of the critical state line at zero pressure and λ and ζ are fitting parameters. The value of Γ is not fixed and can vary based on the anisotropy of the soil and on the current loading direction — this is described in equation (2.39). The location of the critical state line has a significant effect on the model. When a sand sample with a void ratio less than its value at the critical state is sheared, the sample dilates causing an increase in e or p' until the critical state line is reached. Conversely samples with $e > e_c$ contract with shrinking values of e or p' until the critical state line is reached. This behavior is quantified through the state parameter $\psi (= e - e_c)$ defined by Been and Jefferies (1985). Thus, the sign of ψ dictates whether the shear induced volumetric strain will be dilative or contractive. It is the variable ψ that controls the dilatancy relative to the critical state surface (see section 2.1.5).

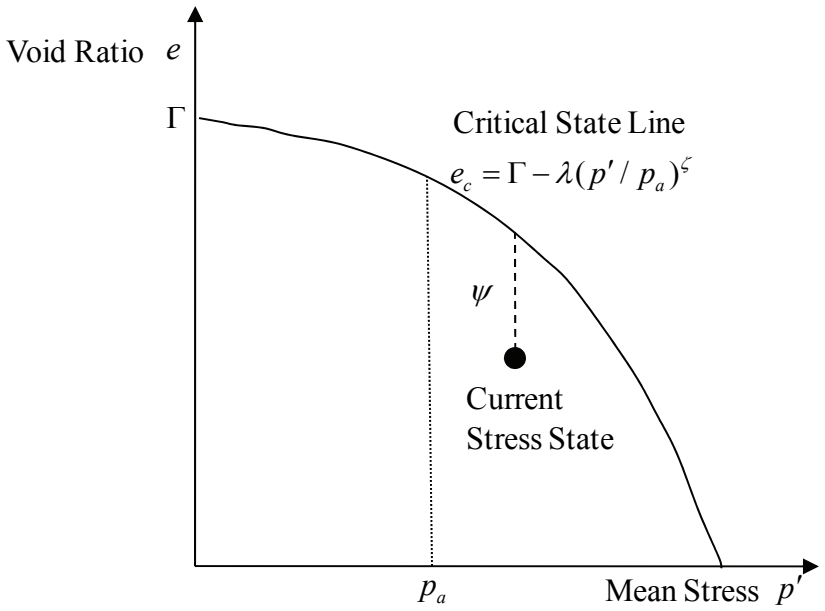

Figure 2.1. Critical state line and state parameter

2.1.2 Yield Surface

The yield surface in the current model is a cone with its apex at the origin of the effective principal stress ($\sigma'_1 - \sigma'_2 - \sigma'_3$) space. The yield surface is illustrated along with the other surfaces of the model in Figure 2.2. The cross-sectional radius of the yield surface increases with increasing mean pressure; the proportionality of this relationship is controlled by an input parameter *m*. In this analysis, *m* is kept constant as the model does not have isotropic hardening. Without any hardening, the central axis of the yield surface stays on a fixed line which is determined by the initial conditions of the soil element. The cone is, however, free to move in the stress space due to kinematic hardening governed by the kinematic hardening tensor α_{ij}. α_{ij} represents the coordinate of the

center of the yield surface on the deviatoric plane (i.e., the plane normal to the hydrostatic axis).

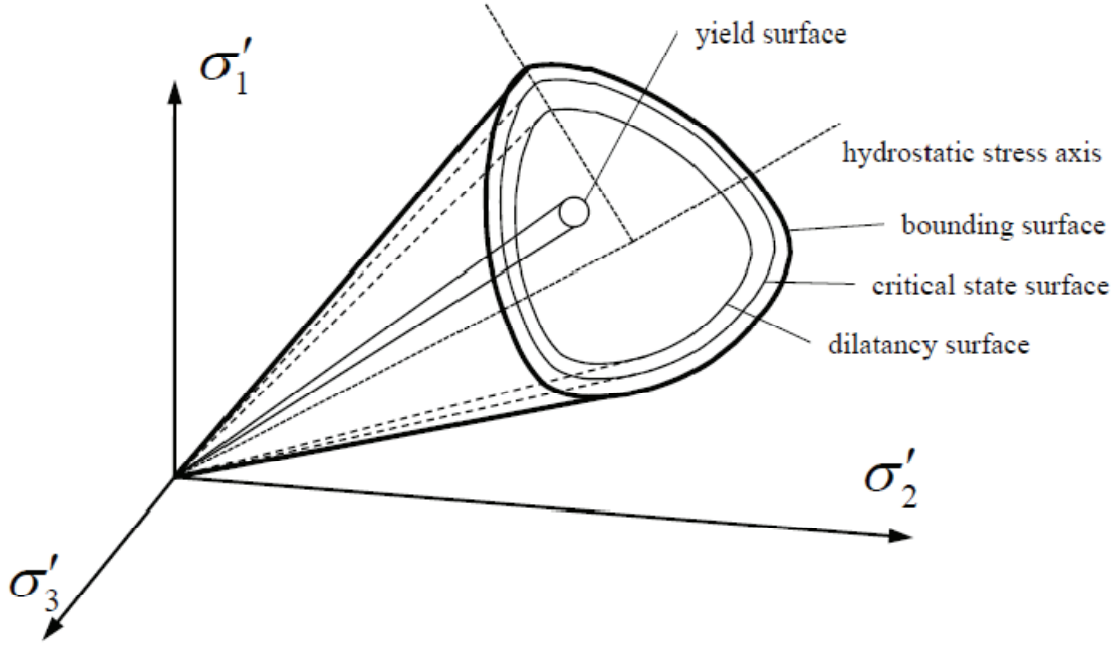

Figure 2.2. Model surfaces in three dimensional stress space

The yield function in the principal deviatoric stress plane is expressed as (Figure 2.2)

$$f = \sqrt{\chi_{ij}\chi_{ij}} - \sqrt{\frac{2}{3}}mp' \tag{2.2}$$

where

$$\chi_{ij} = s_{ij} - \alpha_{ij}p' \tag{2.3}$$

in which s_{ij} is the deviatoric stress tensor. The yield function f has the units of stress. When equated to zero, it gives the shape of the yield surface. The numerical value of f can be related to the distance of the stress state to the yield surface. The yield function can also be expressed in a normalized form as

$$\frac{f}{p'} = \sqrt{\rho_{ij}\rho_{ij}} - \sqrt{\frac{2}{3}}m \tag{2.4}$$

where

$$\rho_{ij} = r_{ij} - \alpha_{ij} \tag{2.5}$$

and

$$r_{ij} = s_{ij} / p' \tag{2.6}$$

where r_{ij} is the deviatoric stress ratio (the term stress ratio in this thesis means stress normalized with respect to the effective mean stress p').

In order to visualize the relationships between the different variables of this model it is convenient to consider a normalized deviatoric plane with coordinates defined by the principle values of r_{ij} (Figure 2.3). Because r_{ij} is a deviatoric tensor, its principle values can be viewed as vectors on the deviatoric plane. In Figure 2.3, r_{ij} represents the location of the current stress state on the normalized deviatoric plane, while α_{ij}, the kinematic hardening tensor, represents the location of the center of the yield surface on the normalized deviatoric plane.

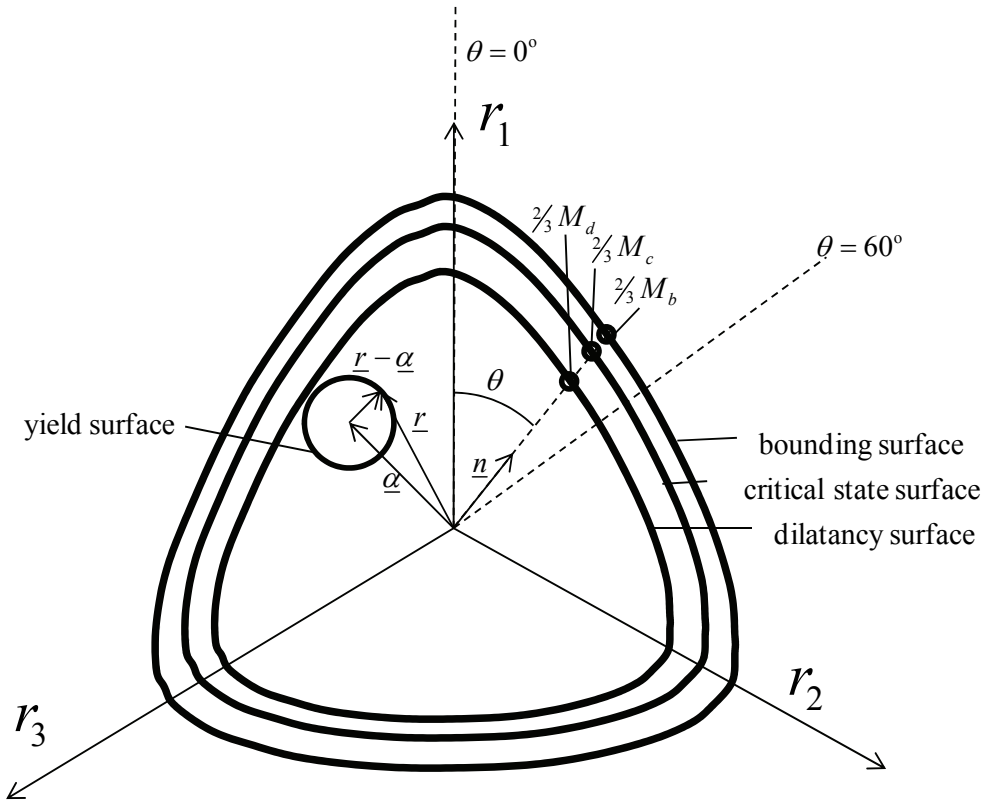

Figure 2.3. Model surfaces on normalized deviatoric plane

In an analysis, the value of f may vary depending on the material state (i.e., whether the material is elastic, elasto-plastic or visco-plastic). Initially, when the material is elastic, the stress state is within the yield surface and f is negative. When the stress point is on the yield surface, the material is elasto-plastic and $f = 0$ in a static analysis where the material follows the theory of classical plasticity (the value of f cannot exceed zero in classical plasticity). However, during a viscous (e.g., viscoplastic) analysis, the stress state can temporarily exceed the yield surface and f can attain a positive value — this is discussed in more detail in section 2.2.

Taking the derivative of f with respect to time gives

$$\dot{f} = \dot{\sigma}_{ij} \frac{\partial f}{\partial \sigma_{ij}} + \dot{\xi}_i \frac{\partial f}{\partial \xi_i} \tag{2.7}$$

where ξ_i represents any plastic variable such as the tensor α_{ij}. In the theory of classical, rate-independent plasticity, it is necessary to calculate the derivative of the yield function with respect to stress and make it equal to zero in order to keep the stress state within the yield surface. This is called the rate-independent consistency condition (Lubliner 2005) given by

$$\dot{f} = \dot{\sigma}_{ij} \frac{\partial f}{\partial \sigma_{ij}} + \dot{\xi}_i \frac{\partial f}{\partial \xi_i} = 0 \tag{2.8}$$

In classical plasticity, the change in the plastic variables is given by

$$\dot{\xi}_i = \dot{\lambda} h_i \tag{2.9}$$

where h_i gives the direction of ξ_i and $\dot{\lambda}$ is the plastic multiplier. Therefore,

$$\dot{f} = \dot{\sigma}_{ij} \frac{\partial f}{\partial \sigma_{ij}} + \dot{\lambda} h_i \frac{\partial f}{\partial \xi_i} = 0 \tag{2.10}$$

which gives

$$\dot{\sigma}_{ij} \frac{\partial f}{\partial \sigma_{ij}} = \dot{\lambda} K_p \tag{2.11}$$

where

$$K_p = -h_i \frac{\partial f}{\partial \xi_i} \tag{2.12}$$

is the plastic modulus.

In order to differentiate the yield function, it is first expressed as shown below

$$f = \sqrt{\left(s_{ij} - p'\alpha_{ij}\right)\left(s_{ij} - p'\alpha_{ij}\right)} - \sqrt{2/3}m\,p' \tag{2.13}$$

The derivative of f with respect to stress, L_{ij} ,which gives the loading direction is given by

$$\begin{aligned} L_{ij} = \frac{\partial f}{\partial \sigma'_{ij}} &= \frac{(s_{ij} - p'\alpha_{ij})}{\sqrt{(s_{kl} - p'\alpha_{kl})(s_{kl} - p'\alpha_{kl})}} \\ &\quad -\frac{1}{3}\left[\frac{(s_{pq} - p'\alpha_{pq})\alpha_{pq}}{\sqrt{(s_{kl} - p'\alpha_{kl})(s_{kl} - p'\alpha_{kl})}} + \sqrt{2/3}m\right]\delta_{ij} \end{aligned} \tag{2.14}$$

which on simplifying gives

$$L_{ij} = \frac{\partial f}{\partial \sigma'_{ij}} = n_{ij} - \frac{1}{3}\left(n_{kl}\alpha_{kl} + \sqrt{2/3}m\right)\delta_{ij} \tag{2.15}$$

where δ_{ij} is the Kronecker's delta and n_{ij} is the loading tensor given by

$$n_{ij} = \frac{\rho_{ij}}{\sqrt{\rho_{kl}\rho_{kl}}} = \frac{(s_{ij} - p'\alpha_{ij})}{\sqrt{(s_{kl} - p'\alpha_{kl})(s_{kl} - p'\alpha_{kl})}} \tag{2.16}$$

The trace of n_{ij} has a magnitude of 1. It is used to describe the direction of loading in the deviatoric plane.

2.1.3 Critical State Surface

The model features a conical critical state surface in the three-dimensional stress space. The apex of the critical state surface is at the origin of the stress space and it is a cone opening along the hydrostatic axis. Unlike the yield surface, the critical state surface is not a "circular" cone in three dimensional stress space. The advantage of a noncircular surface is that different stress paths (e.g., uniaxial compression, triaxial compression, triaxial extension and simple shear) will reach the critical state at different stress ratios. So, by keeping the critical state surface at different distances from the hydrostatic axis for different loading directions, the difference in sand behavior along

different stress paths can be taken into account. The shape of the critical state surface in the deviatoric plane is given by a function of Lode's angle θ. The generic critical state stress ratio M_c defines the angle at which the cone of the critical state surfaces opens, it is given by

$$M_c = M_{cc} g(\theta) \tag{2.17}$$

where M_{cc} is the critical state stress ratio for triaxial compression and $g(\theta)$ is a function of θ defined by Loukidis and Salgado (2009) as

$$g(\theta) = \frac{\left(1 - \frac{1 - C_1^{1/n_s}}{1 + C_1^{1/n_s}}\right)^{n_s}}{\left(1 - \frac{1 - C_1^{1/n_s}}{1 + C_1^{1/n_s}} \cos(3\theta)\right)^{n_s}} \tag{2.18}$$

in which the input parameter n_s is used to control the convex shape of the critical state surface (Loukidis 2006), C_1 is the ratio the critical state stress ratio in triaxial extension and triaxial compression given by

$$C_1 = \frac{M_{ce}}{M_{cc}} \tag{2.19}$$

where M_{ce} is the critical state stress ratio on triaxial extension. The Lode's angle θ in equation (2.18), which represents the direction of loading in the deviatoric plane, can be determined by either of the two following equations:

$$\theta = \tan^{-1}\left(\frac{1}{\sqrt{3}}\left(2\frac{n_2 - n_3}{n_1 - n_3} - 1\right)\right) + \frac{\pi}{6} \tag{2.20}$$

$$\theta = \frac{1}{3}\cos^{-1}\left(\frac{3\sqrt{3}}{2} J_{3n}\right) \tag{2.21}$$

where J_{3n} is the third invariant of the loading tensor n_{ij} and n_1, n_2 and n_3 are the principal values of n_{ij}. Using the above equations, $\theta = 0$ during triaxial compression which yields $g(\theta) = 1$ and $M_c = M_{cc}$. During triaxial extension, $\theta = \pi / 3$ which makes $g(\theta) = C_1$ so that $M_c = C_1 M_{cc} = M_{ce}$. In the implementation of the model, M_{cc} is allowed to vary with increasing confining pressures because it was experimentally observed that, as the confining pressure increases, the effective value of M_{cc} decreases (Graham et al. 2004, Cheng et al. 2005). Input parameters M_{cc}^{MAX} and M_{cc}^{MIN} are selected for the maximum and minimum values of M_{cc}, respectively, and M_{cc} is expressed as

$$M_{cc} = M_{cc}^{MAX} \exp(-0.000015 p') + M_{cc}^{MIN} \left[1 - \exp(-0.000015 p')\right] \tag{2.22}$$

2.1.4 Bounding Surface

This model features a bounding surface which is used to control the magnitude of the plastic strains generated during yielding. An image stress is projected from the current stress state onto the bounding surface in the loading direction. The distance between the two points is used to quantify the plastic modulus K_P defined in equation (2.34).

The bounding surface in the deviatoric stress space is given by

$$M_b = g(\theta) M_{cc} e^{(-\psi k_b)} \tag{2.23}$$

where k_b is a fitting parameter. The shape of the surface is similar to that of the critical state surface and the size of the surface is determined by the parameters ψ and k_b. When the stress state reaches the critical state line in the *e*- *p*' space so that $\psi = 0$, the bounding surface collapses onto the critical state surface. The parameter k_b is given as input and it

takes into account the effect of the bounding surface while the stress state is not on the critical state line.

2.1.5 Dilatancy Surface

The dilatancy surface is also an open cone with its apex at the origin; its shape depends on that of the critical state surface. The dilatancy surface is a function of the stress ratio, the state parameter and a fitting parameter k_d:

$$M_d = g(\theta) M_{cc} e^{k_d \psi} \tag{2.24}$$

When $\psi = 0$, the dilatancy surface collapses onto the critical state surface. However, as the exponents k_b and k_d in the definitions of bounding and dilatancy surfaces are associated with opposite signs, these surfaces are on the opposite sides of the critical state surface. When the stress state in the *e-p′* space lies to the left of the critical state line resulting in a negative value of ψ, the dilatancy surface is inside the critical state surface and the bounding surface is outside the critical state surface. Conversely, when the stress state lies to the right of the critical state line and ψ is positive, the bounding surface is inside the critical state surface and the dilatancy surface is outside the critical state surface.

2.1.6 Stress-Strain Relationship

In the further discussion of the stress variables involving the constitutive model the prime sign (′) will be dropped due to the fact that all the stresses considered in this study are effective stresses. In this model, the incremental stresses are based on the incremental elastic strains as determined by Hooke's law:

$$\dot{\sigma}_{ij} = 2G\left(\dot{\varepsilon}_{ij} - \dot{\varepsilon}_{ij}^{p}\right) + \left(K - \frac{2}{3}G\right)\left(\dot{\varepsilon}_{kk} - \dot{\varepsilon}_{kk}^{p}\right)\delta_{ij} = D_{ijkl}\left(\dot{\varepsilon}_{kl} - \dot{\varepsilon}_{kl}^{p}\right) \tag{2.19}$$

where $\dot{\sigma}_{ij}$ is the incremental stress tensor, $\dot{\varepsilon}_{ij}$ is the incremental total strain tensor, $\dot{\varepsilon}_{ij}^{p}$ is the incremental plastic strain, $\dot{\varepsilon}_{kk}$ and $\dot{\varepsilon}_{kk}^{p}$ are respectively the total and plastic volumetric strain increments, G and K are the shear and bulk moduli and D_{ijkl} is the elastic stiffness matrix. G and K are related to each other by a constant Poisson's ratio ν. The shear modulus is given by (Hardin and Richart 1963)

$$G = C_g \frac{\left(e_g - e\right)^2}{1+e}\left(p'\right)^{n_g} p_a^{1-n_g} \tag{2.25}$$

where C_g, n_g and e_g are input parameters. The bulk modulus is related to the shear modulus as

$$K = G\frac{2+2\nu}{3-6\nu} \tag{2.26}$$

2.1.7 Elastic and Plastic Strains

As previously noted, this model accounts for the development of plastic strains by dividing the total strain into elastic and plastic parts:

$$\dot{\varepsilon}_{ij} = \dot{\varepsilon}_{ij}^{e} + \dot{\varepsilon}_{ij}^{p} \tag{2.27}$$

where $\dot{\varepsilon}_{ij}^{e}$ is the elastic strain increment. While within the yield surface the strain increments remain totally elastic. Decomposition the elastic strain into its volumetric and deviatoric components gives

$$\dot{\varepsilon}_{ij}^{e} = \dot{\varepsilon}_{v,ij}^{e} + \dot{\varepsilon}_{q,ij}^{e} \tag{2.28}$$

where the volumetric component of the elastic strain, $\dot{\varepsilon}_{v,ij}^{e}$, is given by

$$\dot{\varepsilon}^e_{v,ij} = \left(\dot{\varepsilon}^e_{kk} / 3\right)\delta_{ij} \tag{2.29}$$

and the deviatoric component $\dot{\varepsilon}^e_{q,ij}$ is given by

$$\dot{\varepsilon}^e_{q,ij} = \dot{\varepsilon}^e_{ij} - \left(\dot{\varepsilon}^e_{kk} / 3\right)\delta_{ij} \tag{2.30}$$

When the stress state reaches the yield surface, the material undergoes plastic straining. The magnitude and direction of the plastic strain is determined by the flow rule

$$\dot{\varepsilon}^p_{ij} = \dot{\lambda} R_{ij} \tag{2.31}$$

where $\dot{\lambda}$ is the plastic multiplier and R_{ij} is the gradient of the plastic potential surface. The flow rule is based on Dafalias and Manzari (2004) as

$$R_{ij} = R'_{ij} + \frac{1}{3} D\delta_{ij} \tag{2.32}$$

where D is the dilatancy and

$$R'_{ij} = R'^{*}_{ij} / \sqrt{R'^{*}_{kl} R'^{*}_{kl}} \tag{2.33}$$

where

$$R'^{*}_{ij} = \left[1 + \frac{3}{2}\left(\frac{1-c_2}{c_2}\right) g_2(\theta)\cos(3\theta)\right] n_{ij} - \left[3\sqrt{\frac{3}{2}}\left(\frac{1-c_2}{c_2}\right) g_2(\theta)\right]\left(n_{ik}n_{kj} - \frac{1}{3}\delta_{ij}\right) \tag{2.34}$$

in which

$$g_2(\theta) = \frac{2c_2}{\left[(1+c_2) - (1-c_2)\cos(3\theta)\right]} \tag{2.35}$$

and c_2 is a user defined parameter the value of which is set at 0.78 for all sands following Loukidis (2006). The function $g_2(\theta)$ determines the shape of the plastic potential surface in the deviatoric plane under different loading directions. The dilatancy D is given by (Li and Dafalias 2000)

$$D = \frac{D_0}{M_{cc}}\left(\sqrt{\frac{2}{3}}\left(M_d - m\right) - \alpha_{ij} n_{ij}\right) \tag{2.36}$$

Dilatancy is a function of the distance between the current stress state and the dilatancy surface measured along the loading direction. The quantity $\sqrt{\frac{2}{3}}(M_d - m)$ represents the distance of the hydrostatic axis from the center of the yield surface in the deviatoric plane when the yield surface touches the dilatancy surface. Therefore, $\sqrt{\frac{2}{3}}(M_d - m) - \alpha_{ij} n_{ij} = 0$ ensures that the stress point is on the dilatancy surface. The fitted parameter D_0 is used to calibrate the dilatancy to a specific sand type.

By algebraically manipulating equation (2.11), the plastic multiplier $\dot{\lambda}$ is defined as

$$\dot{\lambda} = \frac{1}{K_p}\frac{\partial f}{\partial \sigma_{ij}}\dot{\sigma}'_{ij} \tag{2.37}$$

where K_p is the plastic modulus, previously described in equation (2.12). In this formulation, K_p is a function of the current stress state and the distance to the bounding surface:

$$K_p = h_0 h_k \frac{G \cdot \exp(k_b \psi)}{\left[\frac{3}{2}\sqrt{(r_{ij} - \alpha_{ini,ij})(r_{ij} - \alpha_{ini,ij})}\right]^{\mu}} \sqrt{\frac{2}{3}}\left(\sqrt{\frac{2}{3}}(M_b - m) - \alpha_{ij} n_{ij}\right) \tag{2.38}$$

In the above equation, the term $\left(\sqrt{\frac{2}{3}}(M_b - m) - \alpha_{ij} n_{ij}\right)$ represents the distance between the current stress state and the bounding surface in the direction of n_{ij}. Equation (2.38) is based on Li and Dafalias (2002) with the addition of an input parameter μ used as an

exponent in the denominator (Loukidis 2006). The term h_0 is used to account for the effect of the void ratio as a looser sandl will develop plastic strains with more ease than a dense sand. It is described by the following equation

$$h_0 = \left(\frac{e_{\lim} - e}{h_2} \right)^{h_1} \tag{2.39}$$

where h_1, h_2 and $e_{\lim}$ are input parameters (Loukidis 2006). The variable h_k is used to account for fabric anisotropy of the soil (Dafalias et al. 2004):

$$h_k = k_h \exp\left(\frac{A_{fc} - A_f}{A_{fc} - A_{fe}} \right) \tag{2.40}$$

where k_h is an input parameter and

$$A_f = g(\theta)\left[F_{ij} n_{ij} \right] \tag{2.41}$$

$$A_{fc} = \sqrt{3/2}\ (\alpha - 1/3) \tag{2.42}$$

$$A_{fe} = C_1 A_{fc} \tag{2.43}$$

in which α is an input parameter and F_{ij} describes the preferred particle alignment of the soil. When expressed in matrix notation F_{ij} is given by

$$\underline{F} = \begin{pmatrix} 0.5(1-\alpha) & 0 & 0 \\ 0 & \alpha & 0 \\ 0 & 0 & 0.5(1-\alpha) \end{pmatrix} \tag{2.44}$$

In addition to the effect of fabric anisotropy on the plastic potential, the fabric anisotropy also affects the location of the critical state line. Consequently, in this model, Γ is not a constant but is given by

$$\Gamma = \Gamma_c \exp(A_{fc} - A_f) \tag{2.45}$$

where Γ_c is the value of Γ in triaxial compression.

Setting the input parameters $\alpha = 1/3$ and $k_h = 1$ makes the model behave without fabric anisotropy. The selection of the input parameters so as to remove the effect of fabric anisotropy was made in the course of this research because there was not sufficient information available regarding the particle alignment in the tests that were simulated.

The hardening tensor α_{ij} controls to location of the center of the yield surface on the deviatoric plane. When the stress state reaches the yield surface causing the material to yield, the excess stress is dissipated through plastic straining and the yield surface moves in the direction of loading. This movement of the yield surface is called kinematic hardening and is governed by the following equation

$$\dot{\alpha}_{ij} = \dot{\lambda} \frac{K_p}{p'} \frac{\sqrt{\frac{2}{3}}(M_b - m) n_{ij} - \alpha_{ij}}{\sqrt{\frac{2}{3}}(M_b - m) - \alpha_{ij} n_{ij}} \tag{2.46}$$

The above equation for hardening is so set up that the movement of the yield surface on the deviatoric plane is zero whenever the stress state is on the bounding surface and the loading direction n_{ij} is pointing towards the yield surface. This is enforced by the term $\sqrt{\frac{2}{3}}(M_b - m) n_{ij} - \alpha_{ij}$ which becomes zero when the stress point is on the yield surface and the loading direction n_{ij} is pointing towards the bounding surface.

It may be noted that when the term $\sqrt{\frac{2}{3}}(M_b - m) n_{ij} - \alpha_{ij}$ in the numerator of equation (2.46) becomes equal to zero, the term $\sqrt{\frac{2}{3}}(M_b - m) - \alpha_{ij} n_{ij}$ in the denominator also becomes equal to zero. However, $\sqrt{\frac{2}{3}}(M_b - m) - \alpha_{ij} n_{ij}$ is also present in the

numerator of the term K_p so that, when equation (2.46) is implemented in a code, the right hand side of equation (2.46) is simplified to eliminate these terms thereby avoiding any division by zero.

2.1.8 Interaction of Model Surfaces

In order to summarize the effects that the different model surfaces have, two possible scenarios are discussed. First, consider a soil element which currently has a negative state parameter ($\psi < 0$) and is subjected to shear loading. This soil element is packed more densely than its critical state void ratio. Because the value of ψ is negative, the dilatancy surface is inside the critical state and bounding surfaces. This allows for the stress state to exceed the dilatancy surface on the deviatoric plane which gives negative values of D through equation (2.36). As the stress state approaches the bounding surface the value of K_p decreases allowing for plastic straining during yield. As the soil is in yield with a negative value of D, the volumetric plastic strains will cause the soil to dilate. This dilation is observed in densely packed soils when, upon shearing, the soil particles need to spread apart in order to shear past each other (Salgado 2008). This dilation causes the soil to loosen and increase the void ratio which, in turn, moves the stress point closer to the critical state line thereby changing the value of ψ closer to 0. As the stress point moves closer to the critical state line, both the dilatancy and bounding surfaces move closer to the critical state line. As this happens, the distance of the stress point from both the bounding and dilatancy surfaces decreases which, in turn, leads to less dilation and more plastic strain. Eventually, equilibrium is reached when the

dilatancy and bounding surfaces, as well as the stress state converge on the critical state surface.

Now consider a very loose sample of sand with $\psi > 0$. Initially, the bounding surface is inside the critical state and dilatancy surfaces. This means that the stress state will be far from the dilatancy surface leading to a large and positive value of D. As the soil begins to reach the bounding surface and strains more plastically, the large positive value of D causes the soil to experience contractive volumetric plastic strains. This causes a decrease the void ratio and ψ which, in turn, causes the bounding and dilantancy surfaces to move towards the critical state surface. As the soil sample continues to be strained, it eventually reaches equilibrium when the stress state, the dilatancy surface and the bounding surface merges with the critical state surface.

2.2 Cutting Plane Algorithm and Extension to Viscoplasticity

The constitutive model is used in conjunction with the cutting plane algorithm proposed by Ortiz and Simo (1986). The cutting plane algorithm (Ortiz and Simo 1986) is a semi implicit algorithm that uses explicit elastic predictions with an iterative plastic correction loop. The algorithm is designed for use with yield surface type plasticity models — its framework is general enough so that it can be used with a wide variety of constitutive models with rate-independent plasticity or viscoplasticity.

The formulation of the cutting plane algorithm considers strain controlled loading, i.e., incremental strain is an input parameter in this algorithm. In a finite element analysis, the input strain values get transferred from the boundary value problem to the constitutive model. Incremental stresses are calculated from the incremental strains using the constitutive model. It is advantageous to use a strain based approach because, as a

material becomes plastic, strain may increase without any increase in stress. A stress controlled numerical approximation can suffer from problems of convergence due to plastic instability because the incremented stress may be greater than a possible state of equilibrium.

2.2.1 Elastic-Plastic Formulation of Cutting Plane Algorithm

A requirement of the algorithm is that the strain ε can be additively decomposed into elastic and plastic parts ε^e and ε^p:

$$\varepsilon = \varepsilon^p + \varepsilon^e \tag{2.47}$$

The stress is considered a function of the elastic strain and the internal plastic variables ξ_i (e.g., kinematic hardening variable α_{ij}):

$$\sigma_{ij} = \sigma_{ij}(\varepsilon^e, \xi) \tag{2.48}$$

The plastic strain is obtained from the flow rule:

$$\dot{\varepsilon}_{ij}^p = \dot{\lambda} R_{ij}(\sigma, \xi) \tag{2.49}$$

where R_{ij} (= $\partial G_p / \partial \sigma_{ij}$) is the derivative of the plastic potential function G_p. The evolution of the plastic strain and the plastic variables are both assumed to be functions of σ and ξ. Thus,

$$\dot{\xi}_i = \dot{\lambda} h_i(\sigma, \xi) \tag{2.50}$$

where h_i defines the direction of the change of ξ (Ortiz and Simo 1986).

The calculations begin with an elastic prediction step. During this step, the strain is incremented and the stress increases based on the assumption that the strain is completely elastic. During the elastic prediction the following equations are valid:

$$\dot{\varepsilon} = \dot{\varepsilon}^e \tag{2.51}$$

$$\dot{\sigma}_{ij} = D_{ijkl}\dot{\varepsilon}_{kl} \tag{2.52}$$

$$\dot{\varepsilon}^p = 0 \tag{2.53}$$

$$\dot{\xi}_i = 0 \tag{2.54}$$

Once the stress and strain increments have been calculated, the tensors are updated using the following the equations

$$\sigma_{ij} = \dot{\sigma}_{ij} + \sigma_{ij} \tag{2.55}$$

$$\varepsilon_{ij} = \dot{\varepsilon}_{ij} + \varepsilon_{ij} \tag{2.56}$$

In addition to updating the stresses and strains, parameters such as the void ratio, stress invariants, and the state parameter ψ are updated (note that D_{ijkl} is not updated and stays at the same value as used during the elastic prediction). Using the new values of σ_{ij} and α_{ij}, the position of the stress state relative to the yield surface is checked by calculating the yield function f. The value of the function is checked against the yield surface error tolerance *FTOL,* where *FTOL* is a small positive number. If the stress state is within the yield surface or sufficiently close to it such that the yield function is less than or equal to *FTOL* ($f \le FTOL$), then the increment is accepted and the algorithm is complete. However, if during the elastic prediction step, the stress state exceeds the boundary of the yield surface (i.e., $f > FTOL$), then the algorithm enters into an iterative plastic correction loop. The value of *FTOL* can be determined by the user and should be calibrated based on anticipated levels of stress, required degree of

accuracy and available computational resources — in this study, a value of 0.1 Pa was used.

The correction phase of the algorithm is illustrated in Figure 2.4. In this illustration, the stress state begins within the yield surface. An elastic prediction is made which moves the stress state outside the yield surface at $\sigma^{i=0}$, where the superscript *i* counts the iterations of the correction loop. The yield function $f^{i=0}$, which gives the distance between the stress state and the edge of the yield surface, is greater than *FTOL* causing the algorithm to enter the plastic correction loop. After an iteration of the correction loop, the stress is decreased to $\sigma^{i=1}$ and the plastic variables $\xi^{i=1}$ are adjusted causing the yield surface to kinematically harden and move towards the current stress state. These adjustments work together to decrease the yield function, but because $f^{i=1}$ is still greater than *FTOL* the correction loop iterates again. After the second iteration in this illustration, $f^{i=2}$ is less than *FTOL* and the algorithm is complete.

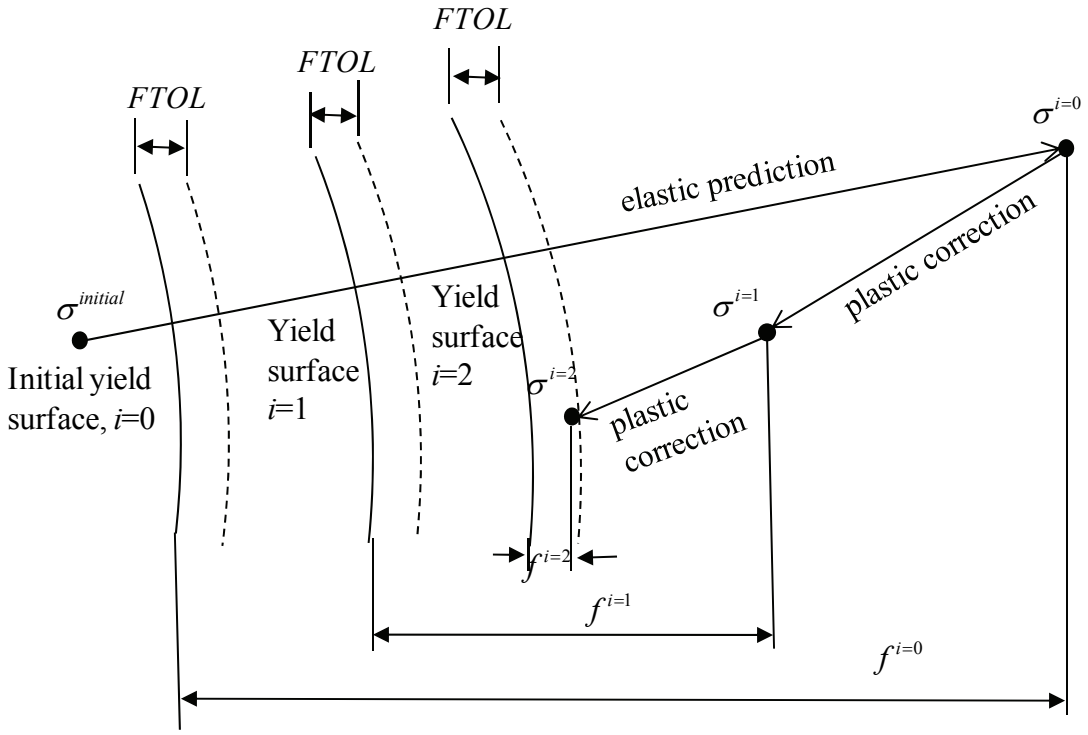

Figure 2.4. Illustration of correction phase of cutting plane algorithm

During the iterative plastic correction loop, the total strain remains fixed. In order for the stress state to return to the yield surface, plastic strains are generated. Since the total strain is fixed, the generation of plastic strain causes a decrease in the elastic strain from the predicted amount and this causes the stress to dissipate resulting in a decrease in the value of f^i. In addition to the decrease in stress, the hardening parameters move the yield surface closer to the current stress state which also works to decrease value of f^i.

The equations governing the plastic correction loop are

$$\dot{\varepsilon} = \dot{\varepsilon}^p + \dot{\varepsilon}^e = 0 \tag{2.57}$$

$$\dot{\sigma}_{ij} = -D_{ijkl}\dot{\varepsilon}^p_{kl} \tag{2.58}$$

$$\dot{\varepsilon}_{ij}^{p} = \dot{\lambda} R_{ij} \tag{2.59}$$

$$\dot{\xi}_{i} = \dot{\lambda} h_{i} \tag{2.60}$$

During the plastic correction algorithm the elapsed time stays constant. Therefore, in the plastic correction algorithm, $dt = 0$ and the derivatives within the loop must be taken with respect to a pseudo time. So, although it is still appropriate to use the plastic equations (2.57)-(2.60) (which are all derivatives with respect to time) when referring to a complete increment of the cutting plane algorithm, these equations are not strictly valid in the plastic correction loop. In order to describe the derivatives with respect to the pseudo time of the iterations of the correction loop, the superscript "*i*" is used to denote the increment within the correction loop and the change is denoted by Δ. Thus, equations (2.58)-(2.60) can be rewritten as:

$$\Delta\sigma_{ij} = -D_{ijkl}\Delta\varepsilon_{kl}^{p} \tag{2.61}$$

$$\Delta\varepsilon_{ij}^{p} = \Delta\lambda R_{ij} \tag{2.62}$$

$$\Delta\xi_{i} = \Delta\lambda h_{i} \tag{2.63}$$

Note that, for the correction loop, $\dot{\lambda}$ is expressed as $\Delta\lambda$ and is calculated using a Taylor series approximation of the yield function (equation (2.2):

$$f^{i+1} = f^{i} + \left(\frac{\partial f}{\partial \sigma_{ij}}\right)^{i} (\sigma_{ij}^{i+1} - \sigma_{ij}^{i}) + \left(\frac{\partial f}{\partial \xi_{k}}\right)^{i} (\xi_{k}^{i+1} - \xi_{k}^{i}) \tag{2.64}$$

In classical plasticity, it is assumed that loading occurs at a slow rate. Hence, the consistency condition is violated marginally and, in each increment, the material is able to fully relax — the stress state comes back to the yield surface. The value of $\Delta\lambda$ is

calculated based on the premise that the stress state will return to the yield surface. Thus, the target value of the yield function f^{i+1} is set to 0:

$$f^{i+1} = 0 \tag{2.65}$$

which makes

$$\Delta f = -f^{i} \tag{2.66}$$

Combining equations (2.64)-(2.66) gives

$$0 = f^{i} + \left(\frac{\partial f}{\partial \sigma_{ij}}\right)^{i} \Delta\sigma_{ij} + \left(\frac{\partial f}{\partial \xi_{k}}\right)^{i} \Delta\xi_{k} \tag{2.67}$$

The derivative with respect to the plastic variables is calculated from equation (2.10) and (2.12) as

$$\frac{\partial f}{\partial \xi_{i}} \Delta\xi_{i} = \Delta\lambda \frac{\partial f}{\partial \xi_{k}} h_{i} = \Delta\lambda K_{P} \tag{2.68}$$

Combining equations(2.61)-(2.63), (2.67) and (2.68), $\Delta\lambda$ can be obtained as

$$\Delta\lambda = \frac{f^{i}}{K_{p} + \frac{\partial f}{\partial \sigma_{ij}} D_{ijkl} R_{kl}} \tag{2.69}$$

Because $\Delta\lambda$ is calculated by taking an approximation of f^{i+1}, the correction loop may take several iterations to return to the yield surface. After calculating $\Delta\lambda$, the stresses are incremented and the value of the yield function is checked. If the stress state is outside the yield surface the correction loop will iterate again. If the stress state is within the yield surface, then the algorithm is completed and the adjusted stress state is recorded as the output.

2.2.2 Modification of Cutting Plane Algorithm for Viscoplasticity

The extension of the cutting plane algorithm for use in viscoplasticity also follows the work of Ortiz and Simo (1986). The extension of this algorithm to viscoplasticity requires the consideration of the actual time (and not the pseudo time) during the correction loop. In the rate-independent plasticity formulation, there was the assumption that the material has sufficient time to relax in each time increment. This ensures that the correction loop will iterate until the stress state has relaxed all the way back to the yield surface. In the viscoplastic formulation, however, the time of relaxation is limited to the duration of the elastic prediction step and the stress state may not return to the yield surface.

In the viscoplastic correction loop, the plastic multiplier $\dot{\lambda}$ is replaced by f/η_v where η_v is the viscosity coefficient (see appendix B) [1]. The elastic prediction part of the algorithm remains the same as explained in the previous section. In the plastic correction loop, the equations for stress and plastic variable increments with respect to t (this is actual time and not the pseudo time of the rate-independent correction loop) become

$$\frac{\partial \sigma_{ij}}{\partial t} = -\frac{f}{\eta_v} D_{ijkl} R_{kl} \tag{2.70}$$

$$\frac{\partial \xi_i}{\partial t} = \frac{f}{\eta_v} h_i \tag{2.71}$$

Using the chain rule of differentiation, the change in the yield function is given by

$$\frac{\partial f}{\partial t} = \frac{\partial f}{\partial \sigma_{ij}} \frac{\partial \sigma_{ij}}{\partial t} + \frac{\partial f}{\partial \xi_i} \frac{\partial \xi_i}{\partial t} \tag{2.72}$$

[1] In the general formulation of overstress function, Φ is used instead of f (Perzyna 1963) where Φ is a function of f. However in the present formulation $\Phi(f) = f$ so the symbol Φ is dropped. This is explained in appendix B.

Combining equations (2.70), (2.71) and (2.72) gives

$$\frac{\partial f}{\partial t} = -\frac{f}{\eta_v}\left[\frac{\partial f}{\partial \sigma_{ij}} D_{ijkl} R_{kl} - K_p\right] \tag{2.73}$$

A term $\bar{t}$ representing instantaneous time (Ortiz and simo 1986) is introduced by combining the terms in equation (2.73) as

$$\bar{t} = \frac{\eta_v}{\frac{\partial f}{\partial \sigma_{ij}} D_{ijkl} R_{kl} - K_p} \tag{2.74}$$

which modifies equation (2.73) to

$$\frac{\partial f}{\partial t} = -\frac{f}{\bar{t}} \tag{2.75}$$

Solving the above differential equation gives

$$f^{i+1} = f^i \exp(-\Delta t / \bar{t}) \tag{2.76}$$

where $\Delta t = t^{i+1} - t^i$ is the time elapsed within an iteration of the correction loop. Equation (2.76) implies

$$\Delta t = \bar{t} \ln\left(\frac{f^i}{f^{i+1}}\right) \tag{2.77}$$

In order to obtain the plastic multiplier $\Delta\lambda$, the Taylor series approximation of the yield function (equation (2.2)) is considered:

$$f^{i+1} = f^i + \frac{\partial f}{\partial t}(t^{i+1} - t^i) \tag{2.78}$$

Substituting equation (2.75) in equation (2.78) and setting $f^{i+1} = 0$ gives

$$0 = f^i - \frac{f^i}{\bar{t}^i}\Delta t \tag{2.79}$$

so that

$$\Delta t = \bar{t}^{\,i} \tag{2.80}$$

In this way, the size of the time step in the correction loop is chosen as the instantaneous time $\bar{t}$. It should be noted though that the above equality between Δt and $\bar{t}^{\,i}$ is only valid for the Taylor series approximation of the change in the yield function.

In order to calculate the change in stress and the internal variables over one iteration of the viscous correction loop, the change in λ is calculated as

$$\begin{aligned}\Delta\lambda_{\text{viscoplastic}} &= \dot{\lambda}\Delta t \\ &= \frac{f}{\eta_v}\bar{t} = \frac{f}{\dfrac{\partial F}{\partial \sigma_{ij}} D_{ijkl} R_{kl} - K_p} = \Delta\lambda_{\text{rate-independent}}\end{aligned} \tag{2.81}$$

It is interesting to note that the expression of $\Delta\lambda$ is identical with that used in the rate-independent correction loop described in the previous section.

In order to solve for the next values of stress and internal variables, the value of $\Delta\lambda$ from equation (2.81) is used to quantify the change in the variables between the iterations of the correction loop. In this way, equations (2.70) and (2.71) can be modified to

$$\sigma_{ij}^{i+1} = \sigma_{ij}^{i} - \Delta\lambda D_{ijkl} R_{kl} \tag{2.82}$$

$$\xi_i^{i+1} = \xi_i^i + \Delta\lambda h_i \tag{2.83}$$

Then, after the new stress state is calculated, the actual elapsed time of the increment Δt is calculated. This is necessary because the variable $\bar{t}$ is a Taylor series approximation of the relaxation time required for the value of the yield function to decrease to zero. The actual elapsed time over the increment Δt is calculated using equation (2.77) based on $\bar{t}$ and the ratio of the values of f^i and f^{i+1} calculated in the course of the correction. It

should be noted that theoretically infinite time is required for the overstress to decrease to zero.

When the summation of the elapsed time increments $\sum_i \Delta t^i$ becomes equal to the total time step *dt* of the analysis (which is controlled from outside of the algorithm either by the user or by the finite element analysis) the total relaxation time expires. Thus, when $\sum_i \Delta t^i = dt$, the program exits the correction loop.

If after updating the stresses it is found that $\sum_i \Delta t^i > dt$ then too much time has elapsed and the current stress state is invalid. If that happens (i.e., if $\sum_i \Delta t^i > dt$), then the set of iterations is rejected and the algorithm returns to the previous values of stresses and state parameters and tries again with a decreased value of $\Delta\lambda$ (the decreased value is assumed to be $\Delta\lambda/10$ in this research). Decreasing the value of $\Delta\lambda$ does not affect the solution to the final stress value that is converged upon, only the number of iterations required to reach that value changes. This process is continued until $\sum_i \Delta t^i$ falls within some tolerance of dt. This tolerance was so set that, in order for the program to exit the correction loop, the total elapsed time has to meet the condition $(1-TTOL)dt < \sum_i \Delta t^i \le dt$ where *TTOL* is the tolerance used (the value of *TTOL* is assumed to be 0.0001 in this research).

An illustration of the viscoplastic correction algorithm is shown in Figure 2.5. In this illustration (Figure 2.5), the cutting plane algorithm is entered with the stress state $\sigma^{initial}$ all ready outside the yield surface. At this initial point, an elastic prediction is

made which moves the stress state further outside the yield surface to $\sigma^{i=0}$. Because at the start of this iteration the yield function $f^{i=0}$ is still greater that *FTOL*, the cutting plane algorithm enters the viscoplastic correction loop. In the first iteration, the stress decreases by a relatively large amount to $\sigma^{i=1}$ and the elapsed time $\Delta t^{i=1}$ is calculated. In this illustration, $\Delta t^{i=1}\left(=\sum_{i=1}^{1}\Delta t^{i}\right)<dt$ so that the iteration is accepted. At the next iteration, a new stress is again calculated but this time $\Delta t^{i=2}$ is so large that $\sum_{i=1}^{2}\Delta t^{i}>dt$. Consequently, the relaxed stress state $\sigma^{i=2}$ (shown with a hollow circle in Figure 2.5) is not permissible and a decreased value of $\Delta\lambda$ is used to obtain a new relaxed value of the stress state $\sigma^{i=2}$ (shown by a filled circle in Figure 2.5). For this second attempt, $\sum_{i=1}^{2}\Delta t^{i}<dt$ because of which $\sigma^{i=2}$ is accepted and the next iteration starts. The iterations are continued until the condition $(1-TTOL)dt<\sum_{i}\Delta t^{i}\le dt$ is met.

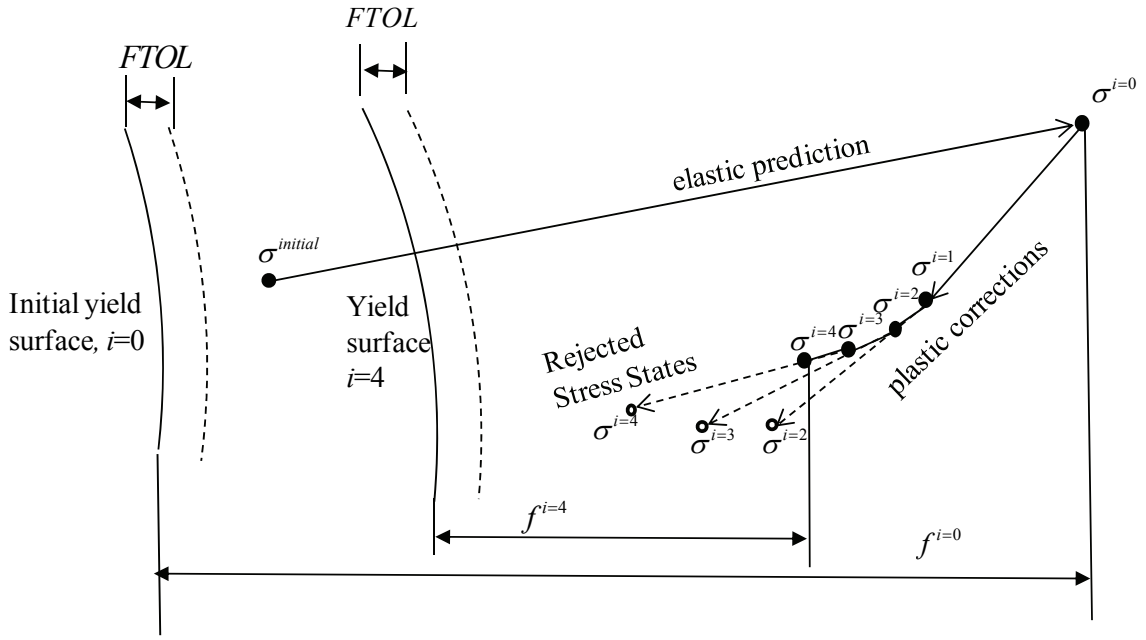

Figure 2.5. Illustration of the viscoplastic correction phase of cutting plane algorithm

It is possible in the course of the plastic correction that the position of the final relaxed stress state is inside the yield surface. This is theoretically not possible, since the material should cease to relax as soon as the stress state reaches the yield surface. Therefore, an additional check is done to make sure that the value of $f^{i+1} > 0$. Numerical problems occur if $f^{i+1} \le 0$ because of a negative logarithm or division by zero in the computation of equation (2.77). So when the predicted value of $\Delta\lambda$ causes the overstress to move inside the yield surface resulting in $f^{i+1} \le 0$, the iteration is rejected and the stress state returns to the values of the previous iteration and a decreased value of $\Delta\lambda$ is used to move further.

In addition to being forced to exit the viscoplastic correction loop when the total relaxation time expires, the correction loop also ends when the value of the yield function is decreased to within the tolerance of the yield surface (i.e., when $f \leq FTOL$). This occurs because, even if more relaxation time is available, negligible change in the values of stress and plastic variables will occur with further relaxation when $f \leq FTOL$. Figure 2.6 shows the flowchart of the viscoplastic cutting plane algorithm used in this research.

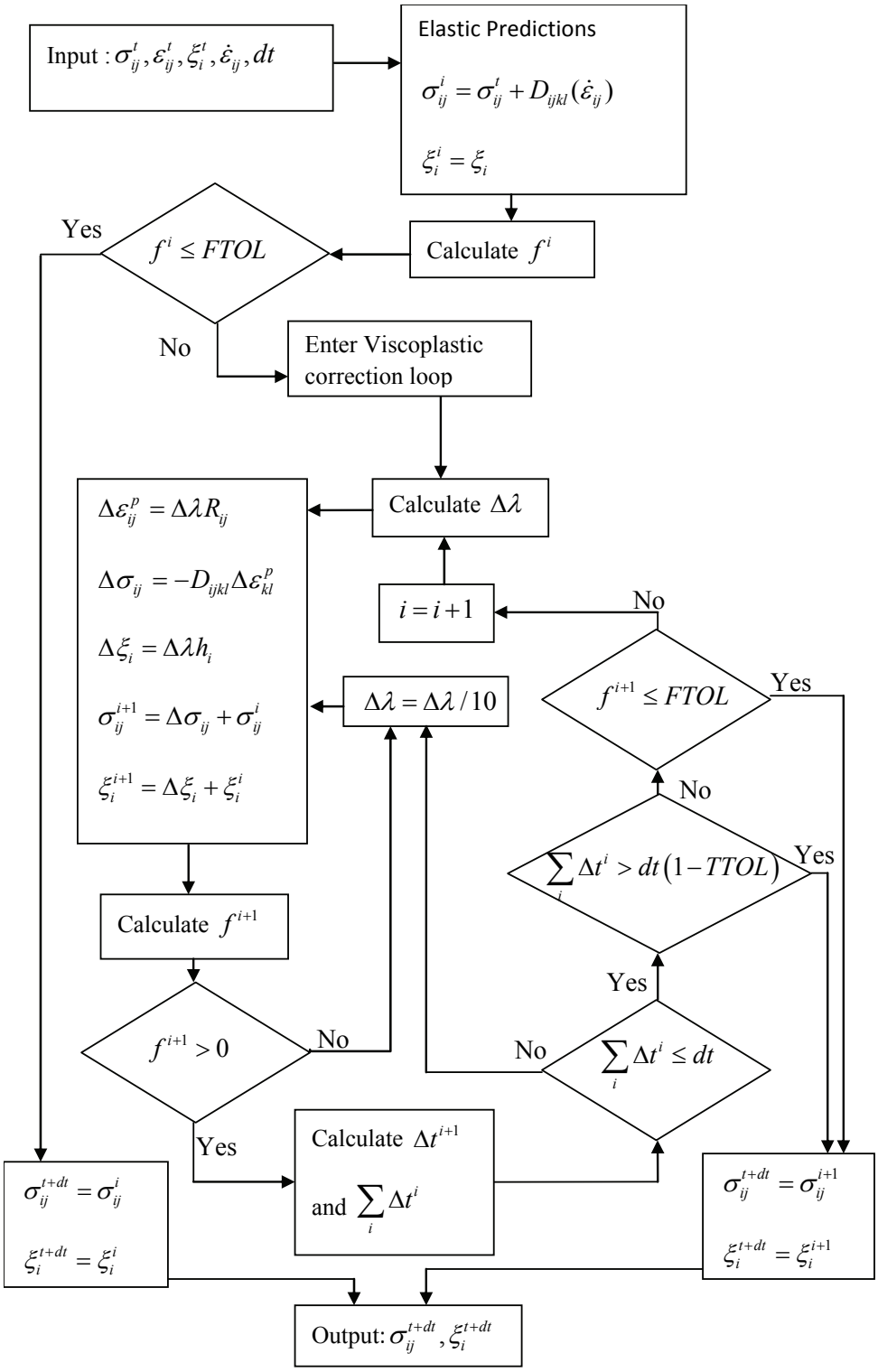

Figure 2.6. Flow chart of the viscoplastic correction phase of cutting plane algorithm

2.3 Hierarchy of Algorithms and Error Control

There are multiple components used to create the user material subroutine that implements this constitutive model. In addition to the constitutive equations and cutting plane algorithm described above, there is an error control algorithm used in the implementation of the model. The error control algorithm works by comparing the solution obtained using the cutting plane algorithm with a time step prescribed by the finite element software with the solution obtained after two successive cutting plane algorithms with a time step equal to half of that prescribed by the finite element software (Loukidis 2006, Herrmann et al. 1987, Sloan and Booker 1992). If the error between these two solutions is too large, then the time step is further divided into smaller sub steps, the results of which are subsequently added in order to find the total change in stresses and internal variables. Appendix C explains the error control algorithm in more details.

The hierarchy of the algorithms used in the implementation of the constitutive model is presented in Figure 2.7. The finite element software executes the user subroutine after it has solved for incremental strains over a given time step. This, along with the current stresses and internal variables are passed on to the error control algorithm. The error control algorithm passes the reduced values of the time step and the stress increment into the cutting plane algorithm which in turn uses the equations of the constitutive model to solve for changes in stress and internal variables.

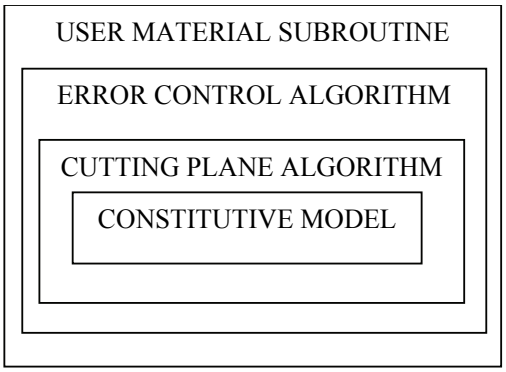

Figure 2.7. Hierarchy of algorithms in the user subroutine

2.4 Calibration and Validation

The developed constitutive model was used to simulate the drained triaxial compression tests and Split Hopkinson Pressure Bar (SHPB) tests performed on Ottawa and Fontainebleau sands. The parameters used in the simulations are given in Table 2.1.

Table 2.1 Parameters used in the simulations of Ottawa and Fontainebleau sand tests

Parameters	Ottawa sand	Fontainebleau sand
ν	0.15	0.3
C_g	611	650
e_g	2.17	2.17
n_g	0.437	0.437
Γ_c	0.85	2
λ	0.12	1.1
ζ	0.275	0.1
M_{cc}^{MAX}	1.31	1.157
M_{cc}^{MIN}	0.9	0.9
k_b	1.9	3
h_1	2.2	1.2
h_2	0.24	0.2
e_{lim}	0.81	1
m	0.05	0.05*
C_1	0.71	0.71*
c_2	0.78	0.78
n_s	0.35	0.35*
D_0	1.31	0.5
k_d	2.2	2
μ	1.2	1.2*
η_v (kPa·sec)	50	5

*Assumed to be the same as that of Ottawa sand

The parameters used for the Ottawa sand were mostly obtained from Loukidis (2006) where the calibrations were done based on triaxial compression tests (Carraro et al. 2004, Murthy et al. 2006), triaxial extension tests (Murthy et al. 2006) and Bender element tests (Carraro et al. 2003). The data used in the calibration of critical state the parameters Γ_c, λ, and ζ were originally obtained from triaxial tests with mean stresses

ranging from 100 to 1000 KPa (Murthy et al. 2006). Because the mean stress in an SHPB test can reach up to 100 MPa, it was found that the critical state line proposed by Loukidis (2006) did not extrapolate well to greater values of mean stress. Consequently, modifications were made to the critical state parameters Γ_c, λ, and ζ so as to better capture the sand behavior at high strain rates and at high pressures experienced in the SHPB test. The new values of the parameters governing the critical state line were found by optimizing the critical state line to capture the behavior of the SHPB tests (Veyera and Ross 1995) while maintaining good agreement with the triaxial tests. The critical state line obtained in this study and that proposed by Loukidis (2006) along with the experimental data of Murthy et al. (2006) are shown in Figure 2.8.

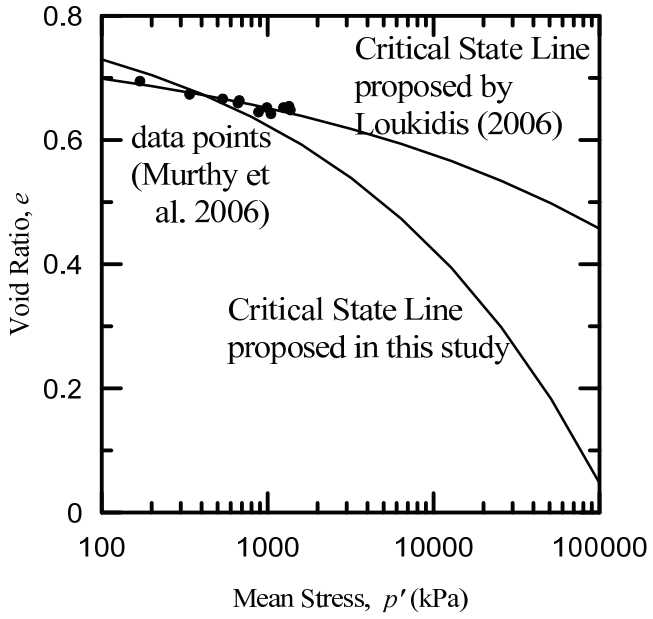

Figure 2.8. Critical state line proposed in this study and that proposed by Loukidis (2006) based on the data of Murthy et al. (2006)

The calibration of Fontainebleau sand was done using the data from triaxial compression tests (Luong 1980, Dano et al. 2004, Hircher et al. 2008, Gaudin et al. 2003), triaxial extension tests (Luong 1980), torsional hollow cylinder tests (Georgiannou and Tsomokos 2008) and SHPB tests (Semblat et al. 1999). Certain parameters for Fontainebleau sand, marked with an asterisk (*) in Table 2.1, were assumed to be identical to those of Ottawa sand due to lack of available test data. Again, the critical state parameters had to be adjusted to account for the higher stresses encountered in the SHPB tests (Semblat et al. 1999).

The parameter η_v was calibrated using the results of the SHPB tests (Veyera and Ross 1995, Semblat et al. 1999). The greater the dependence of the soil properties on the strain rate is, the greater the value of η_v is. The values of η_v and strain rate can cause the material behavior to range between two extremes: (1) when η_v and the strain rates are very low, the material is able to fully relax at every increment and the behavior tends towards rate-independent plastic behavior and (2) when η_v and the strain rates are both very high, the material cannot relax at all and the behavior tend towards elastic behavior. This is illustrated in Figure 2.9 in which simulations of Ottawa sand in uniaxial compression with a strain rate of 1000/s is shown. In the figure, the leftmost plot was generated without letting the model to enter the corrective plastic loop of the cutting plane algorithm (this creates a perfectly elastic behavior). For the rightmost plot, the constraints on the elapsed time of the cutting plane algorithm were removed which created a nonviscous elastic-plastic behavior. It can be seen that a variation of η_v causes the results to fall between these two extreme plots.

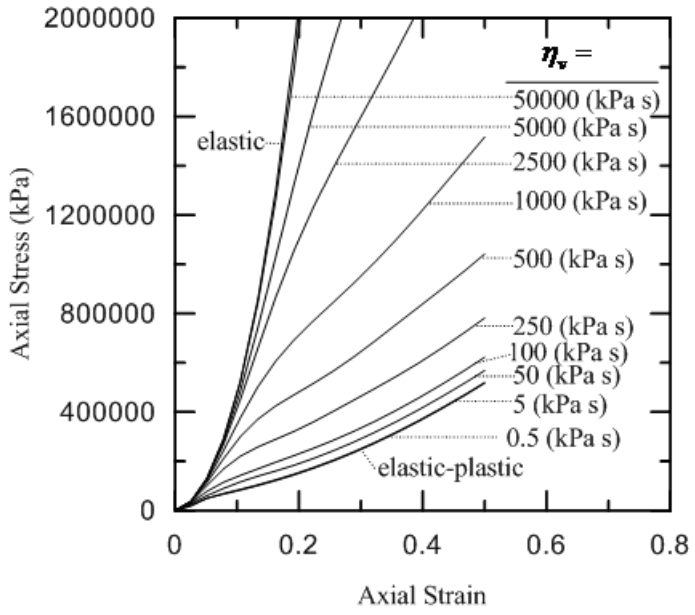

Figure 2.9. Effect of the variation of η_v on Ottawa sand in uniaxial compression with an axial strain rate of 1000/second

2.4.1 Simulation of Triaxial Tests

The triaxial tests were simulated using a single axisymmetric element in the finite element software Abaqus version 6.91 (Abaqus User's Manual 2009). The element was fixed against vertical movement at its bottom boundary. The element was given an initial stress with the outer radial boundary subjected to a constant pressure. The analysis was driven by applying vertical displacement at the top boundary of the element. A schematic illustration is given in Figure 2.10.

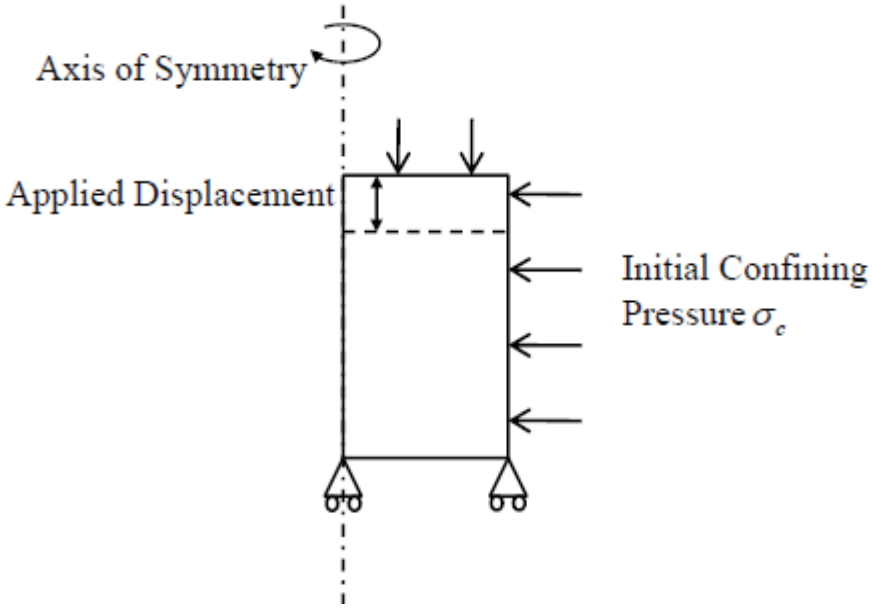

Figure 2.10. Schematic of element loading and boundary conditions for simulation of drained triaxial tests

The triaxial tests for Ottawa sand are based on the test data of Carraro (2004). The initial confining pressure in these tests was set at 100 KPa and tests were run at initial void ratios of 0.7 and 0.55. Figures 2.11 and 2.12 show the shear stress versus axial strain and the volumetric strain versus axial strain plots, respectively. The definition of shear stress used to plot the results is that of the deviatoric stress q commonly used in soil mechanics:

$$q = \frac{1}{\sqrt{2}}\sqrt{(\sigma_1 - \sigma_2)^2 + (\sigma_1 - \sigma_3)^2 + (\sigma_2 - \sigma_3)^2} = \sqrt{3J_2} \tag{2.83}$$

where σ_1, σ_2 and σ_3 are the principal stresses and J_2 is the second invariant of the deviatoric stress tensor. Note that, for triaxial compression tests, equation (2.83) reduces to $q = \sigma_1 - \sigma_3$. In this thesis, the shear stresses are plotted in terms of q. It is evident

from Figures 2.11 and 2.12 that the constitutive model differentiates between dilative and contractive behavior of Ottawa sand at different void ratios quite well and provides an adequate match to the peak and critical state stress values.

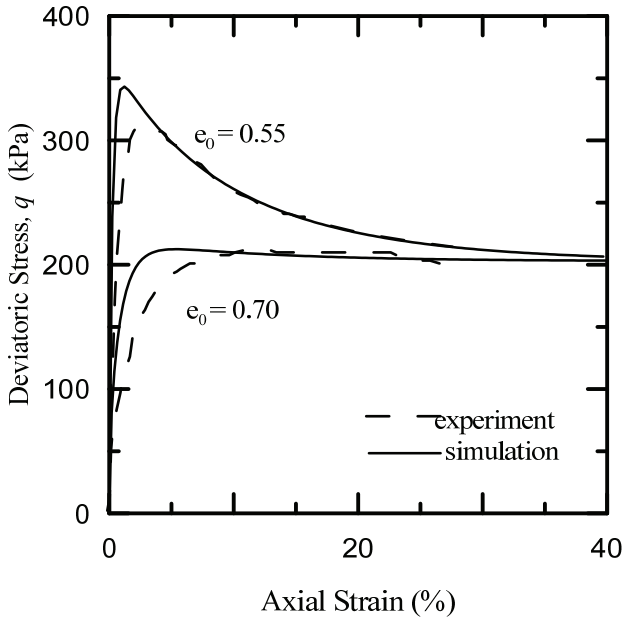

Figure 2.11. Shear stress versus axial strain of Ottawa sand in drained triaxial test with initial confining pressure of 100 kPa

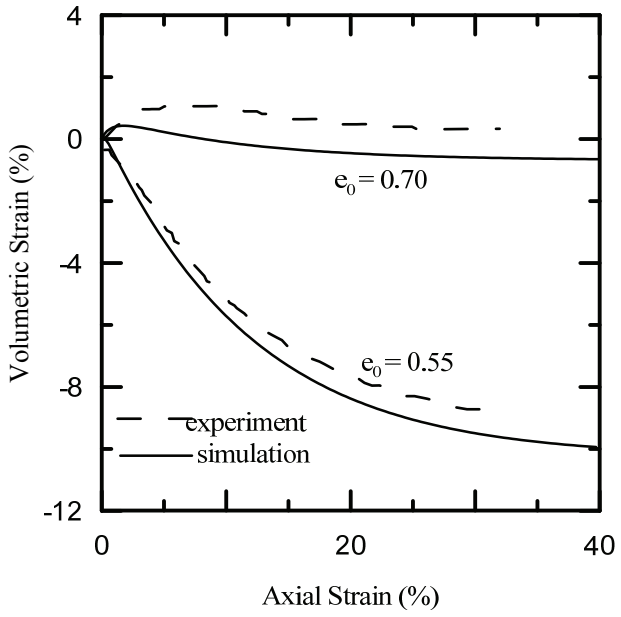

Figure 2.12. Volumetric strain versus shear strain of Ottawa sand in drained triaxial test with initial confining pressure of 100 kPa

Figures 2.13 and 2.14 show the shear stress versus axial strain and volumetric strain versus axial strain plots, respectively, of the simulations of triaxial tests on Fontainebleau sand. The triaxial compression test data for Fontainebleau sand is obtained from Luong (1980). The initial confining pressure was set at 100 kPa and the tests were run at the void ratios of 0.72 and 0.92. Although the peak stresses are not well captured, the model is still able to capture the contractive and dilative behavior of loose and dense sand samples with reasonable accuracy, and the relationship between the volumetric and axial strains is captured very well.

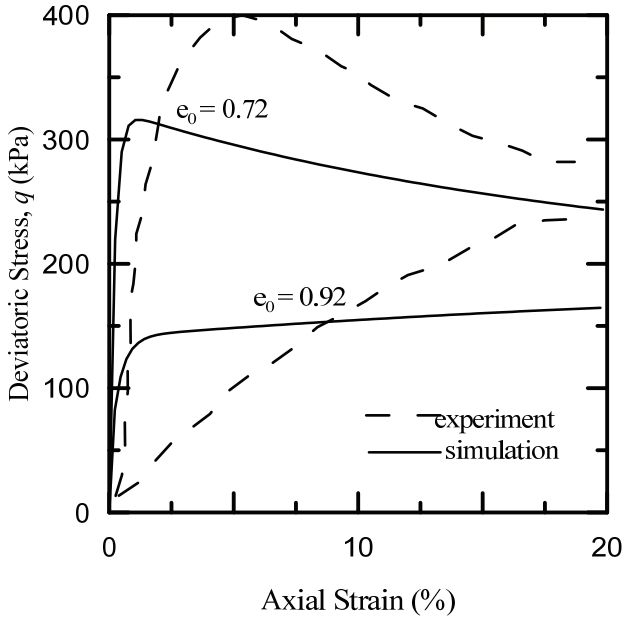

Figure 2.13. Shear stress versus axial strain of Fontainebleau Sand in drained triaxial test with initial confining pressure of 100 kPa

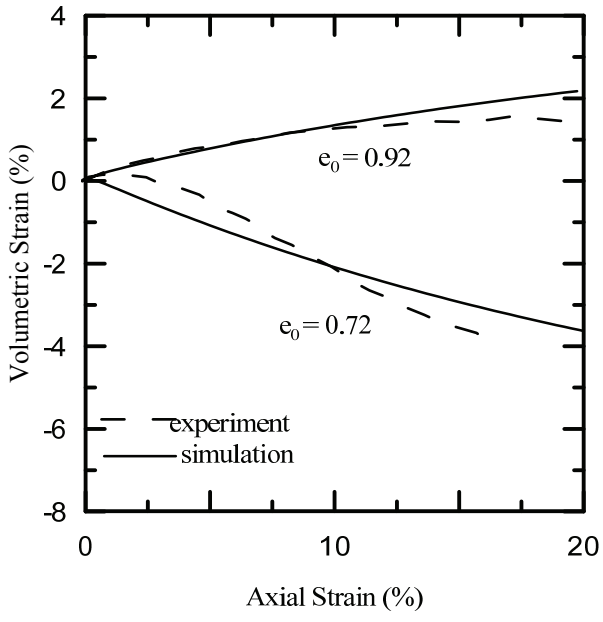

Figure 2.14. Volumetric strain versus axial strain of Fontainebleau Sand in drained triaxial test with initial confining pressure of 100 kPa

2.4.2 Simulation of SHPB Tests

The SHPB tests were simulated using an explicit dynamic analysis scheme in the finite element software Abaqus. Four separate axisymmetric parts were created to simulate the striker bar, incident bar, transmitted bar and the soil sample. The bars were simulated using the elastic material model in Abaqus and the soil specimen was simulated as a user defined material that follows the constitutive model developed in this research. The magnitude of the impulse wave was controlled by adjusting the initial velocity of the striker bar in Abaqus. In the actual experiments, the soil sample was confined against transverse displacement with a rigid collar. In the simulations, this effect was accounted for by directly applying boundary condition to soil sample so that the transverse displacement was restrained. The contact between the bars and the specimen were modeled using hard contact. A schematic of the simulation set up is given in Figure 2.15. In the analysis, the stresses and strains were recorded directly from the elements of the soil sample instead of calculating the values of stress and strain based on the strains in the incident and transmitted bar, as is done in the physical experiments (Al-Mousawi et al. 1997).

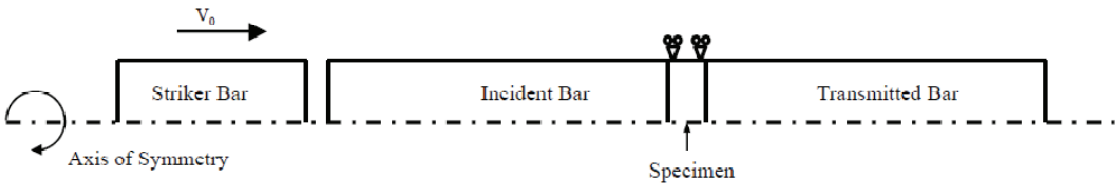

Figure 2.15. Schematic of geometry and boundary conditions used to simulate SHPB tests (not to scale)

Veyera and Ross (1995) conducted SHPB tests with different sample lengths, sands and water contents. They achieved strain rates between 1000/s and 2000/s. The Ottawa sand samples they tested were compacted to a void ratio of 0.545 (corresponding to a relative density D_r = 100%) with lengths L_0 = 1.27 cm and 0.635 cm and a diameter equal to 5.08 cm. The samples were confined laterally with a rigid thick-walled container. The SHPB set up had stainless steel bars with a diameter of 5.08 cm. The material properties used for simulating the bars are Young's modulus = 207 GPa and density = 7850 kg/m^3. The striker bar had a length, of 0.635 m, the incident bar had a length of 3.66 m and the transmitted bar had a length of 3.35 m. Veyera and Ross (1995) described the stress history of their impulse wave as 225 MPa with a pulse length of 250 μs (Figure 2.16). By using an initial striker bar velocity of 12 m/sec in the simulation, an impulse wave was produced that is comparable to the one reported by Veyera and Ross (1995). The impulse waves of the experiments of Veyera and Ross (1995) and of the simulations done in this research are presented in Figure 2.16.

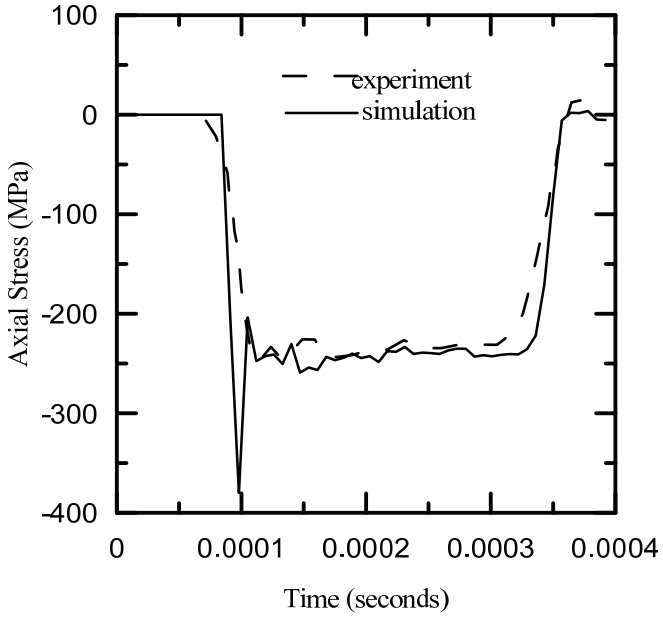

Figure 2.16. Impulse used in the simulations of SHPB tests on Ottawa sand

Figure 2.17 shows the axial stress versus axial strain plots of the SHPB tests performed on Ottawa sand samples. The stress-strain plots show that a sample subjected to a faster strain rate achieves greater stresses. There is a reasonably good match between the experimental data and the simulation results.

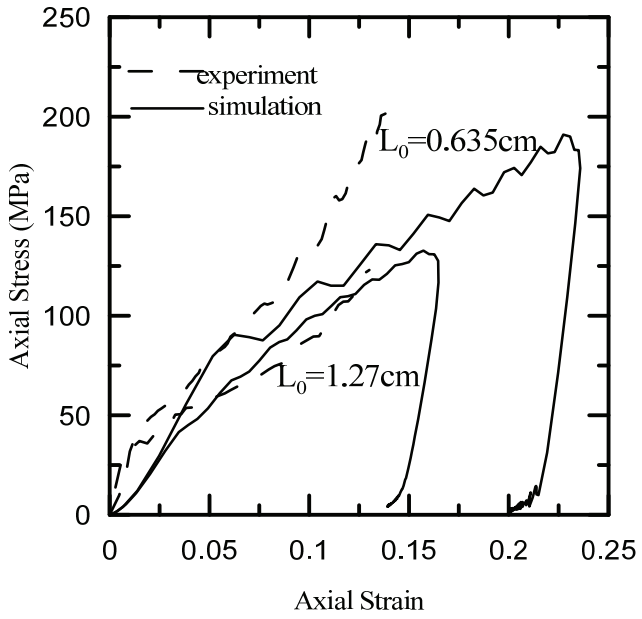

Figure 2.17. Simulations of SHPB tests on Ottawa sand

The simulations for Fontainebleau sand were based on the tests done by Semblat et al. (1999). Semblat et al. (1999) ran tests with different lengths of soil sample and with different velocities of the striker bar to create different strain rates in their samples. The stress-strain plots are shown in Figure 2.18 for tests with samples of length 10 cm and diameter 40 mm with the initial striker bar velocity V_0 = 6.8 m/sec, 11.6 m/sec and 19.8 m/sec. The samples had an initial void ratio of 0.667. The bars used in the SHPB set up had a diameter of 40 mm, Young's modulus of 70 GPa, and density of 2820 Kg/m^3. The striker bar had a length of 0.85 m while the impulse and transmitted bar had a length of 2 m each. The simulated stress-strain plots match the experimental results well.

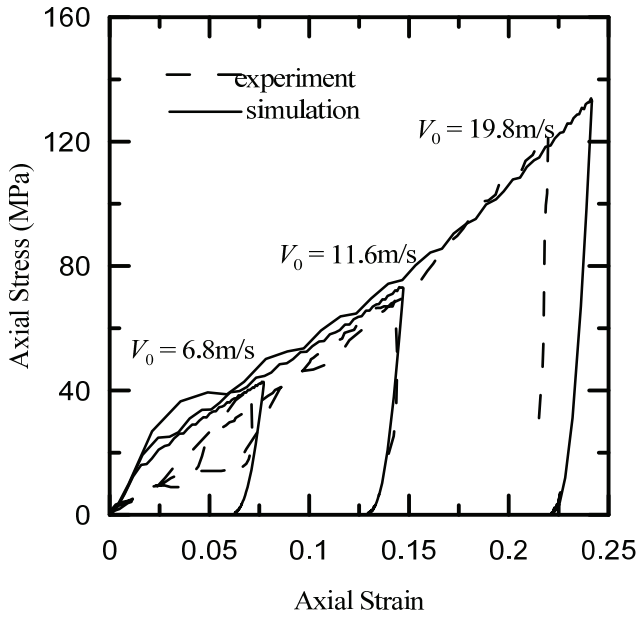

Figure 2.18. Simulations of SHPB tests on Fontainebleau sand

2.5 Conclusions

In this chapter, the formulation and implementation of a constitutive model are described that can simulate the high strain-rate behavior of sands. The model is based on the concepts of the critical state soil mechanics, the bounding surface plasticity theory and the overstress theory of viscoplasticity. The model parameters were determined for Fontainebleau and Ottawa sands. The model was used to simulate the drained triaxial tests and the split Hopkinson pressure bar tests performed on Fontainebleau and Ottawa sands. The simulations were performed using the finite element method in which a single element is used to represent the soil sample.

The constitutive model is capable of differentiating between the contractive and dilative behavior of sand and predicts the pre- and post-peak behavior of Fontainebleau

and Ottawa sands in triaxial tests with reasonable accuracy. The model is also capable of simulating the high strain-rate behavior of sand, as exhibited in the split Hopkinson pressure bar tests, with reasonable accuracy.

CHAPTER 3 - ANALYSIS OF TUNNELS SUBJECTED TO BLAST

3.0 Introduction

In this chapter, underground tunnels subjected to internal blasts are analyzed using the finite element method. Explosions are simulated in the tunnels and the resulting stress wave propagating through the surrounding soil is analyzed. The purpose of this exercise is to demonstrate the ability of the constitutive model to simulate real field problems and to investigate how the ground surrounding the tunnel behaves if it has properties similar to Ottawa and Fontainebleau sands.

3.1 Details of Simulation

Two tunnel geometries were considered in this study. In one case, the center line of the tunnel was at 5 m below the ground surface and, in the other case, the center line was at a depth of 10 m. For both the cases, the tunnel had an internal radius of 2.85 m with a 0.15 m thick concrete lining. Two dimensional plane strain finite element analyses were performed. Thus, plane sections of circular tunnels embedded in sand were assumed in the analysis. A dynamic pressure was applied on the inner lining of the tunnel — this generates stress waves that propagate out through the sand. The applied pressure inside the tunnel was obtained by simulating the explosion of C4.

The finite element analyses were performed using rectangular, plain strain, reduced integration (CPE4R) elements in Abaqus. The finite element meshes used in the analysis are shown in Figures 3.1 and 3.2. In order to save on the computation time, only half of the domain was analyzed by imposing a symmetry boundary condition along the left vertical boundary of the mesh. The top horizontal boundary was free to displace while the bottom horizontal boundary was fixed. The vertical boundary on the right allowed vertical displacements but not horizontal displacements. The fixed bottom boundary can be imagined to represent very stiff bed rock underlying the soil layer. This boundary was located at a sufficient distance so that it had no impact on the results of the analysis — the results were obtained at a time when the pressure wave from the loading was far from the bottom boundary. The right horizontal boundary was also at sufficient distance as the results were obtained well before the pressure wave reached this boundary. The mesh for the 5 meter deep tunnel consists of 1624 elements and 1718 nodes and the mesh for the 10 meter deep tunnel consists of 2306 elements and 2414 nodes. In all the analysis, the tunnel lining was meshed with one row of elements.

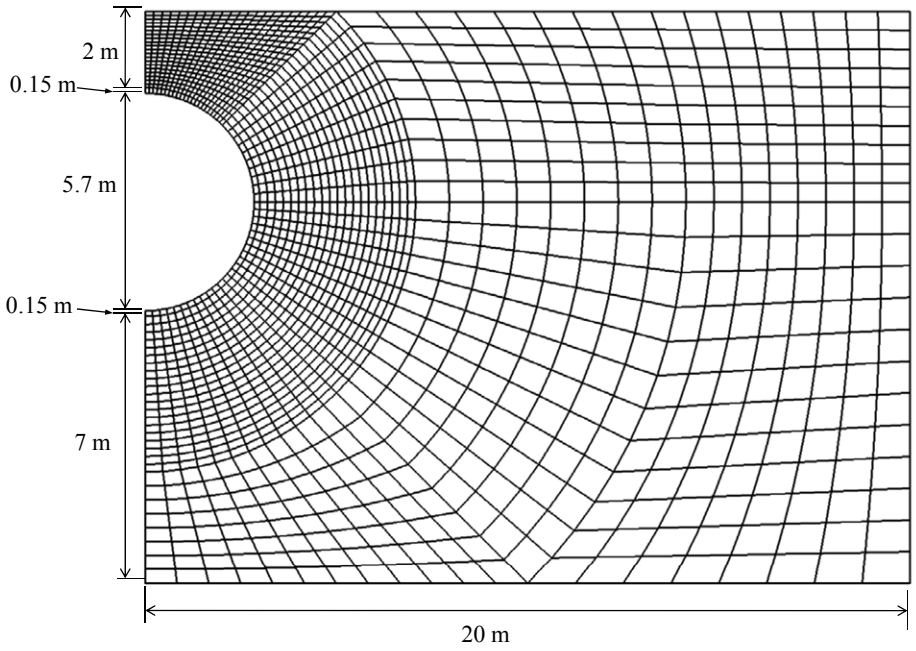

Figure 3.1. Finite element mesh used in the analysis of tunnel with the center line at a depth of 5 m below the ground surface

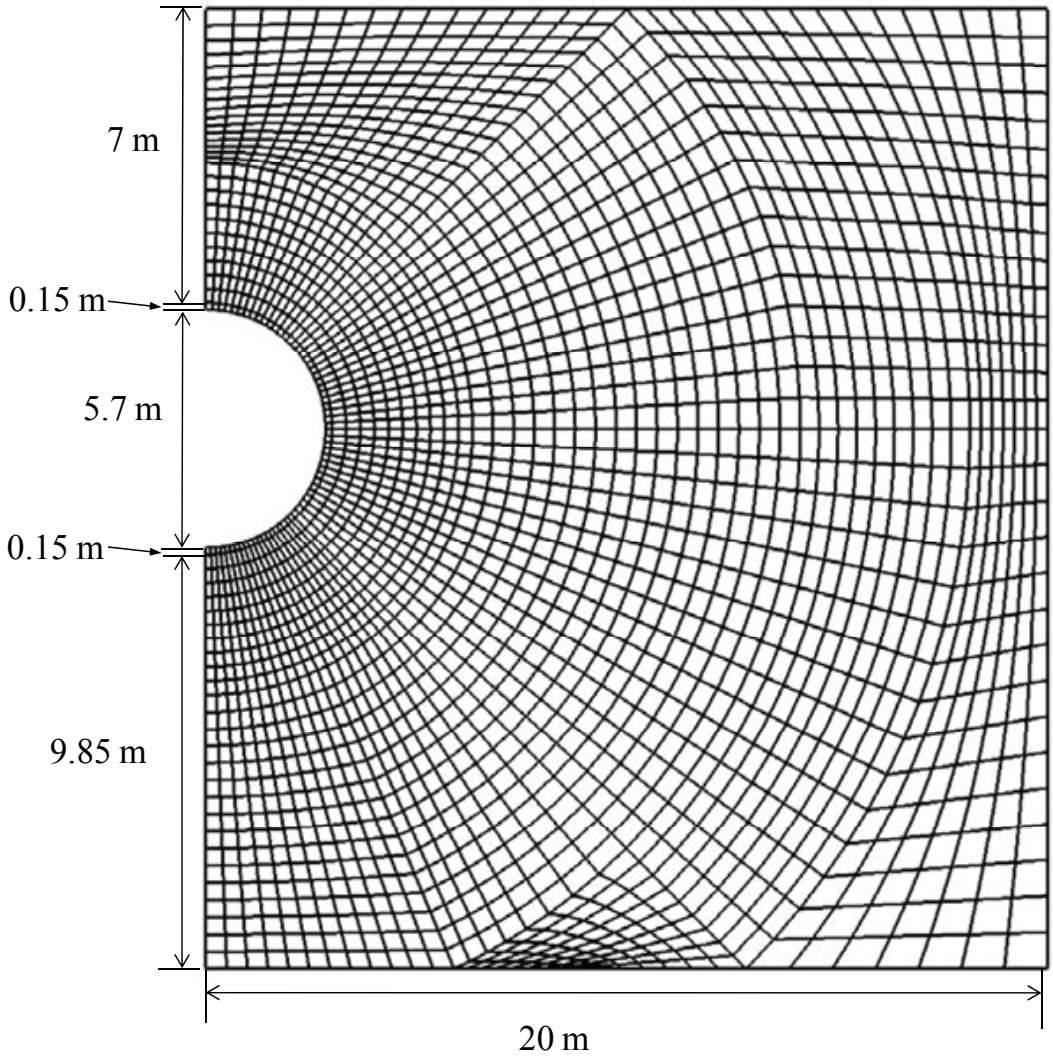

Figure 3.2. Finite element mesh used in the analysis of tunnel with the center line at a depth of 10 m from the ground surface

The blast loads were applied to the tunnels along the inner lining as a uniformly distributed pressure that varies with time. The pressure amplitude curves that give the variation of the applied pressure as a function of time were obtained by simulating the explosive material with the Jones-Wilkens-Lee (JWL) model (Lee et al. 1973) in a dynamic explicit analysis. The JWL material model is an equation of state where the

pressure is governed by the internal energy and density of the exploding material (Lee et al. 1973). In order to simulate an explosion using the JWL model, the explosive material is modeled in its solid, pre-detonation state and meshed using several elements. Upon detonation there is a rapid increase in pressure causing the explosive material to expand outwards. When the material detonates, the generated pressure is given by

$$P = A\left(1-\frac{\omega\rho}{R_1\rho_0}\right)\exp\left(-R_1\frac{\rho_0}{\rho}\right)+B\left(1-\frac{\omega\rho}{R_2\rho_0}\right)\exp\left(-R_2\frac{\rho_0}{\rho}\right)+\frac{\omega\rho^2}{\rho_0}E_m \qquad (3.1)$$

where A, B, R_1, R_2 and ω are material constants the values of which are available for several common explosive materials, ρ is the current density of the explosive, ρ_0 is the density of the explosive in the solid state before the detonation and E_m is the internal specific energy of the explosive. The model requires additional inputs for simulations — these include the initial value E_{m0} of the internal energy (before the explosion), the detonation wave speed C_d, and an initial point at which the detonation begins.

In this study, the explosive C4 was assumed to be circular in cross section located at the center of the tunnel and the surrounding air was modeled as an ideal gas with the assumption that the tunnel lining and the ground followed elasticity. The average length of the elements used to mesh the C4 was 5 mm before the detonation. The air was meshed using Arbitrary Euler-Lagrange adaptive meshing in order to prevent element distortion. The radial length of the air elements before detonation ranged from 35 mm to 450 mm. Once the explosion occurs at the initial detonation point, the surrounding points in the mesh of the explosive material progressively detonates — the time lags between the detonation at these points and the initial point are equal to the corresponding distances between them divided by the detonation speed C_d. In this analysis, the initial detonation

point of the C4 was set at its center. The pressure generated from the explosion propagates through the air onto the tunnel lining. For this study, the simulations were run with the radius of C4 equal to 0.05 m and 0.1 m, which represent approximately 12.6 Kg/m and 50.3 Kg/m of C4, respectively. The JWL parameters for C4 used in the simulations are given in Table 3.1.

Table 3.1 JWL parameters used in modeling C4 explosive material (Larcher and Casadei 2010)

Parameter	Value
C_d	8500m/sec
A	598.155 GPa
B	13.75 GPa
R_1	4.5
R_2	1.5
ω	0.32
E_{m0}	5.4341 MJ/Kg
ρ_0	1601 kg/m^3

A typical mesh used in the JWL simulations is shown in Figure 3.3. This figure corresponds to the case in which the radius of the C4 is 0.05 m. The mesh of the surrounding soil is not shown in these figures.

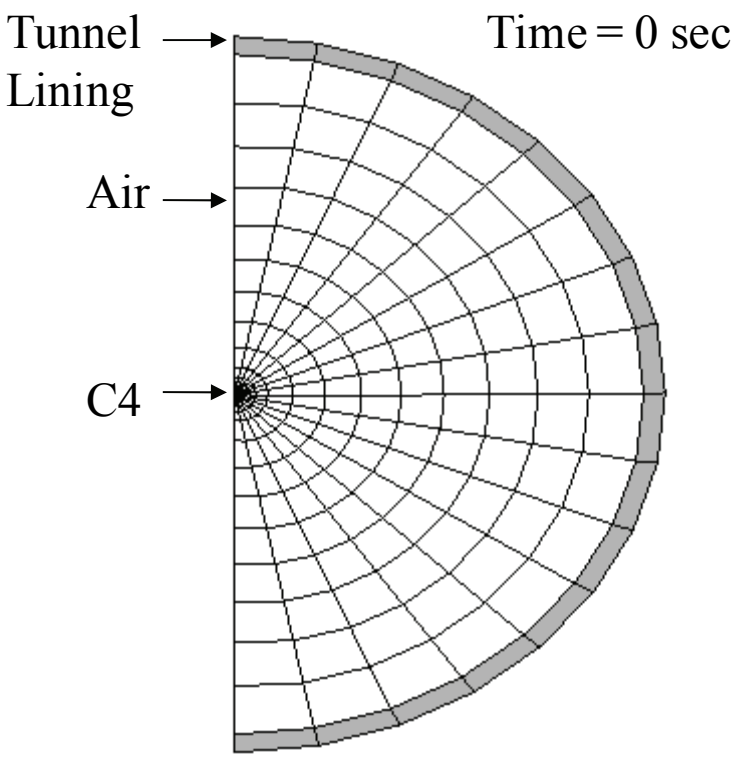

Figure 3.3. Undistorted mesh used in the JWL simulation of C4 explosive

Figure 3.4 shows the same mesh as in Figure 3.3 after it has deformed over a period of 0.001 sec. In this figure, the C4 has expanded radially by thirty-five times its initial size. As the C4 expands, the elements of air resize themselves to prevent distortion. It is interesting to note from Figures 3.3 and 3.4 that, over the elapsed time of 0.001 seconds, the outer circular boundary of the explosive material has moved by 1.75 m — the expansion speed is significantly greater than the speed of sound (i.e., the wave speed of the air) which is 340.29 m/sec.

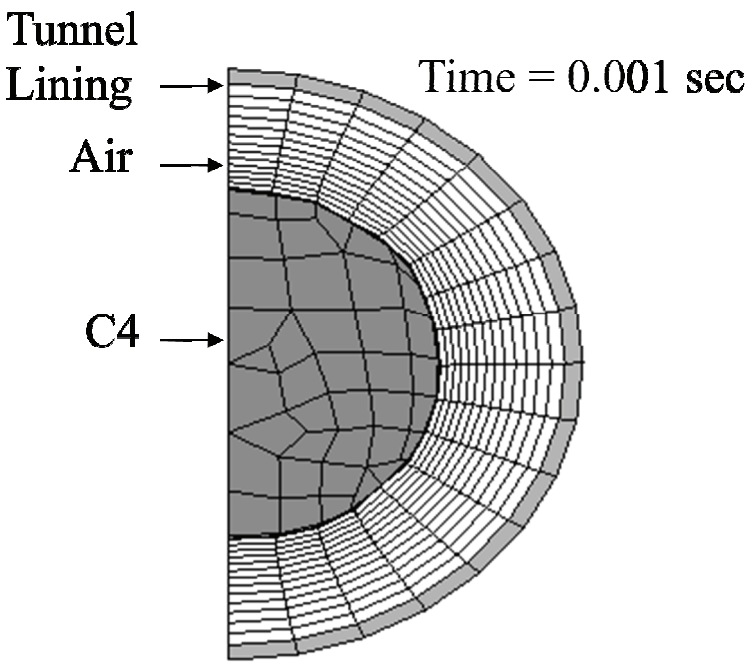

Figure 3.4. Distorted mesh used in the JWL simulation of C4 explosive

Figures 3.5 and 3.6 show the pressure generated immediately adjacent to the inner lining of the tunnels as a function of time from the JWL explosion analysis of the C4. The air pressure on the elements adjacent to the tunnel lining were recorded and used as the applied pressure on the tunnel lining. The air elements were greatly deformed due to the explosion so that the centroids of the air elements adjacent to the tunnel lining moved very close to the tunnel. Hence, minimal error was incurred in approximating the air pressure adjacent to the tunnel lining as the applied pressure on the tunnel walls. A consequence of the C4 expanding faster than the wave speed in air (as noted in the discussion of Figure 3.3 and 3.4) is that the pressure histories of the air elements adjacent

to the tunnel lining exhibits multiple peaks due to the pressure wave reflecting back and forth between the tunnel lining and the JWL material.

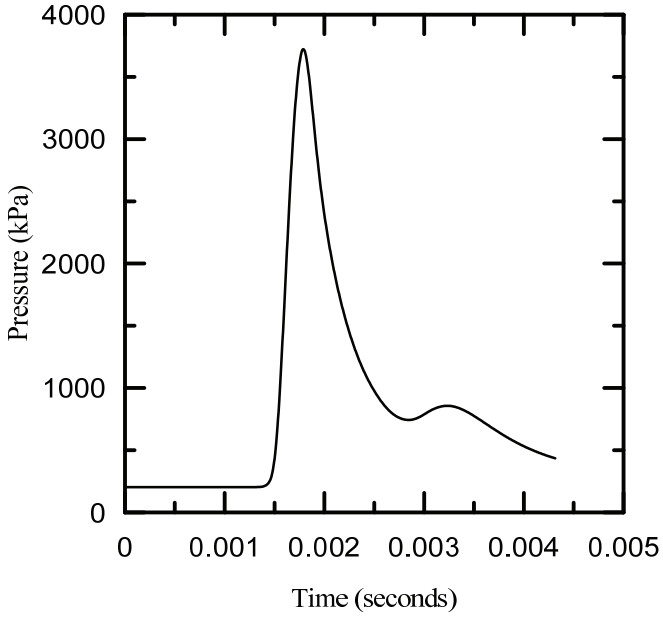

Figure 3.5. Pressure amplitude curves from C4 of radius 0.05 m in a tunnel with 2.85 m internal radius

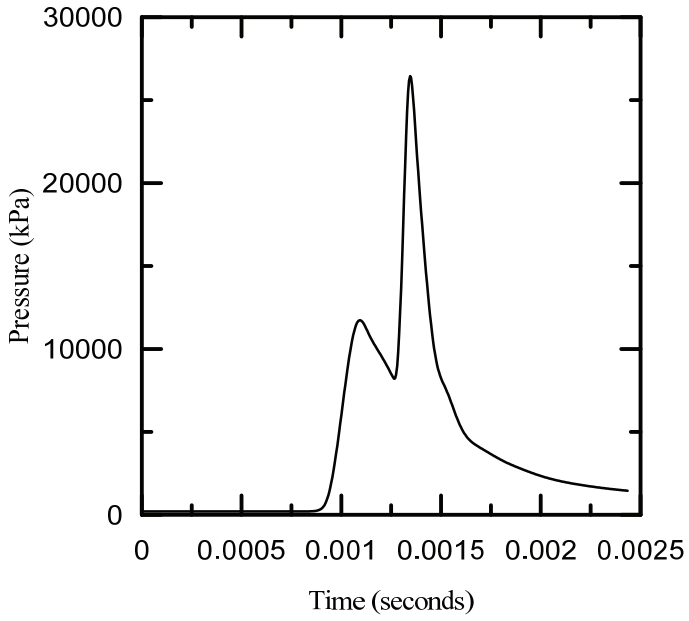

Figure 3.6. Pressure amplitude curves for C4 of radius 0.1 m in a tunnel with 2.85 m internal radius

In the finite element simulations of the tunnels subjected to blast, the above pressure versus time plots (also called the pressure amplitude curves) were applied directly to the tunnel lining as uniformly distributed pressure loadings. A more rigorous approach would be to integrate the JWL modeling with the finite element analysis of the tunnel. However, such a coupled analysis created numerical difficulties.

The concrete lining of the tunnel was modeled using the concrete damaged plasticity model in Abaqus — the material properties for concrete used in the analysis are given in Table 3.2. The soil surrounding the tunnel was modeled using the properties of Ottawa and Fontainebleau sand (see Table 2.1 for the soil parameters).

Table 3.2 Material properties for concrete tunnel lining

Parameter	Value
E, Young's Modulus	31.027 GPa
ν, Poisson's Ratio	0.15
Tensile Yield Stress	2.9 MPa
Compressive Yield Stress	13 MPa

In the finite element analysis, the initial void ratios of Ottawa and Fontainebleau sands were set at 0.545 and 0.667, respectively. The initial confining pressure was set by slowly increasing the gravitational forces on the analysis domain. This caused the effective stress to increase with depth as each element of soil had to bear the self weight as well as the weight of the elements on top of it. Before gravity was applied, a small hydrostatic pressure of 10 kPa was applied over the entire soil domain. This was necessary because the sand constitutive model requires a confining pressure to work. The additional pressure of 10 kPa was maintained throughout the analysis so that the confining pressure on the ground surface remained greater than zero (otherwise, numerical problems arise). Because the stresses were calculated by the constitutive model, the horizontal stresses due to applied gravity could not be determined a priori. It was found from the analysis that the coefficient of earth pressure at rest $K_0 (= \sigma'_h / \sigma'_v$, where σ'_h and σ'_v are the effective horizontal and vertical stresses, respectively) varied with depth. The plot of K_0 versus depth for the simulations with Ottawa sand is shown in Figure 3.7. The plotted values in Figure 3.7 were obtained along the right vertical

boundary of the finite element domain. The values of K_0 for Fontainebleau sand ranged from 0.45 to 0.7. As gravity was applied, the soil strained causing a slight spatial variation of the void ratio. The initial void ratio in the simulations of Ottawa sand ranged from 0.542 to 0.545 and that for Fontainebleau sand ranged from 0.664 to 0.667.

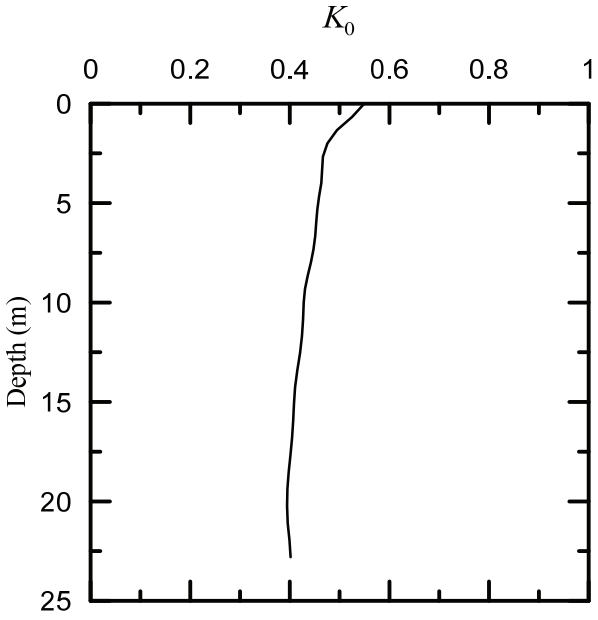

Figure 3.7. Coefficient of earth pressure at rest K_0 versus depth for the ground comprising of Ottawa Sand

3.2 Results

3.2.1 Temporal and Spatial Variation of Stresses and Displacements

The focus of this research is to investigate how the tunnel and the adjacent ground respond to the blast loads. Consequently, stresses and deformations generated in the

ground due to the blast were investigated — the study was mostly done along a horizontal path as shown in Figure 3.8.

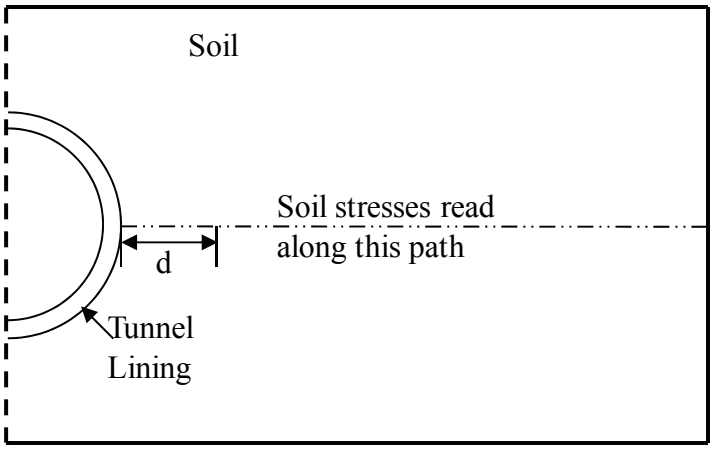

Figure 3.8. Path along which stresses were investigated

Figure 3.9 shows the variation of the mean stress with time at three different points in the ground at a distance d = 0.5 m, 1.5 m and 2.5 m from the interface of the tunnel and ground along the horizontal path shown in Figure 3.8. The center line of the tunnel is located at a depth of 10 m below the ground surface. The ground is assumed to have the same properties as that of Ottawa sand. The blast is simulated for C4 with a radius of 0.1 m. As the stress wave propagates, the mean stress reaches a maximum and then decreases. Also, the maximum value of the stress decreases with increasing distance from the tunnel.

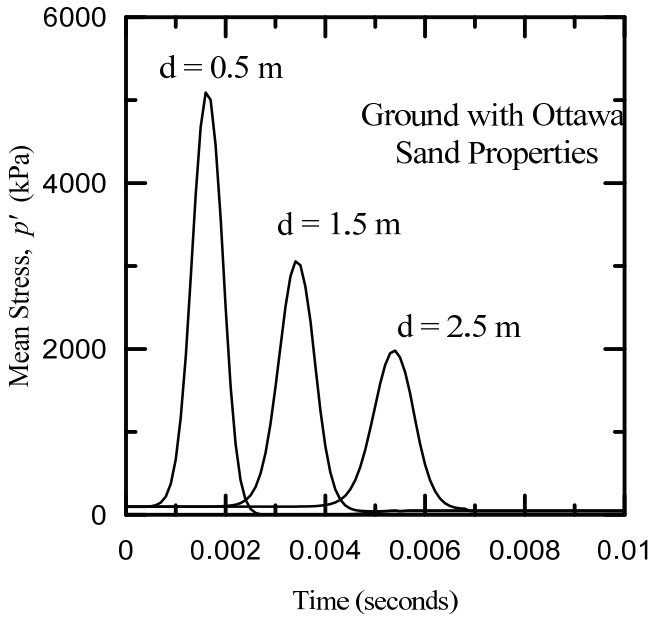

Figure 3.9. Mean stress at three points in the ground at different horizontal distance d radially outward from the outer edge of a 10 m deep tunnel subjected to a blast of C4 with a radius of 0.1 m

Figures 3.10 shows similar temporal variations of the deviatoric (shear) stress q for the same problem described above. The variation and dissipation of the shear stress is similar to that of the mean stress.

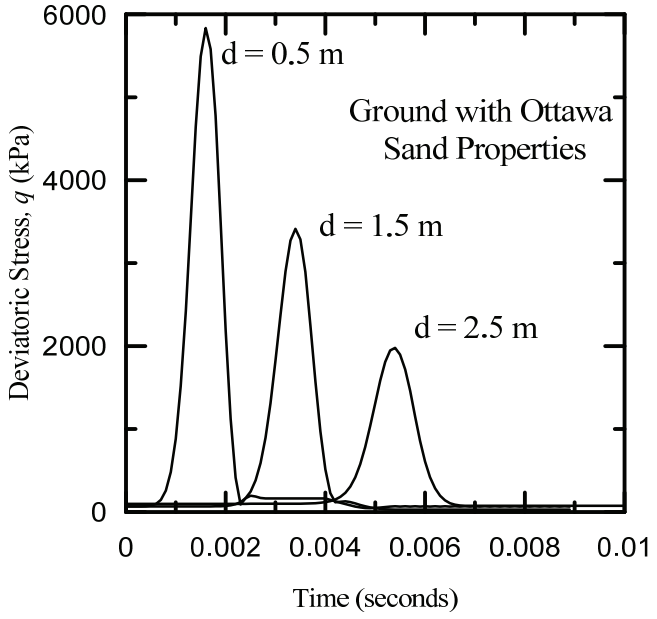

Figure 3.10. Shear stress at three points in the ground at different horizontal distance d radially outward from the outer edge of a 10 m deep tunnel subjected to a blast of C4 with a radius 0.1 m

In order to demonstrate the effect the explosion has on the ground surface, the ground displacement profiles are plotted in Figures 3.11 for three different points of time. This figure is for the 5 m deep tunnel in Ottawa sand with the blast generated using the C4 with a radius of 0.1 m. In order to show the most critical displacements of the ground surface, the case was selected where the tunnel is at 5 m depth and the C4 has a radius of 0.1 meters.

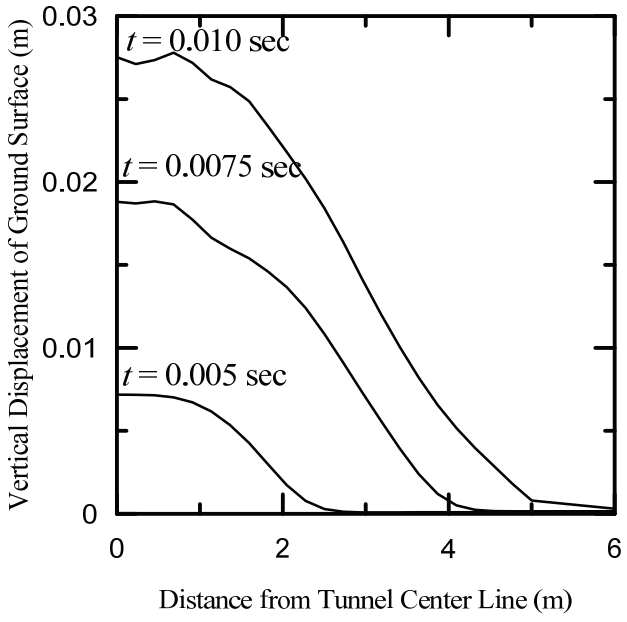

Figure 3.11. Vertical displacement of the ground surface above a 5 m deep tunnel in Ottawa sand due to a blast of C4 with a radius of 0.1 m

3.2.2 Effect of Soil Type

In order to determine the effect of soil type on the ground response, simulations were done using both Fontainebleau and Ottawa sand properties for the ground. Figures 3.12 and 3.13 show the maximum mean stress dissipation over horizontal distance measured radially outward from the tunnel along the horizontal line shown in Figure 3.8. For these figures, the history of mean stress versus time was collected for a continuous path of elements emanating horizontally out from the centroid of the tunnel and the maximum pressure experienced over time in each element is plotted as a function of the distance from the outer edge of the tunnel lining. It is evident that the rate of spatial dissipation of the stresses is faster for Ottawa sand. This is consistent with the split Hopkinson pressure bar test results (presented in chapter 2) in which Ottawa sand displayed greater amount of viscous dissipation.

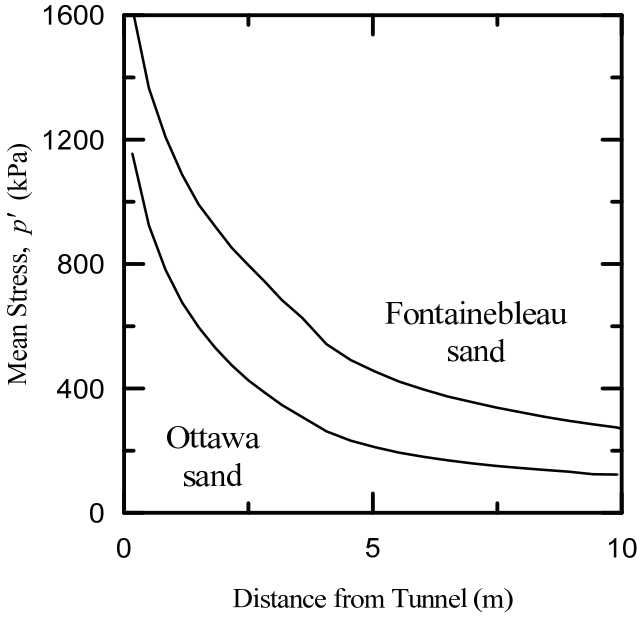

Figure 3.12. Maximum mean stress versus distance from a 10 m deep tunnel subjected to a C4 explosive of radius 0.05 m

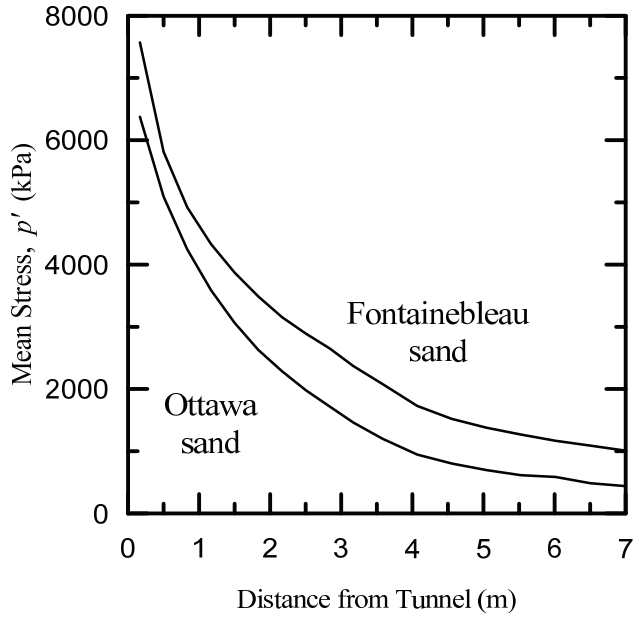

Figure 3.13. Maximum mean stress versus distance from a 10 m deep tunnel exploded with C4 of radius 0.10 m

Figures 3.14 and 3.15 show the maximum values of the shear stress along the horizontal path shown in Figure 3.8. The nature of the spatial dissipation exhibited by the shear stress is similar to that of the mean stress.

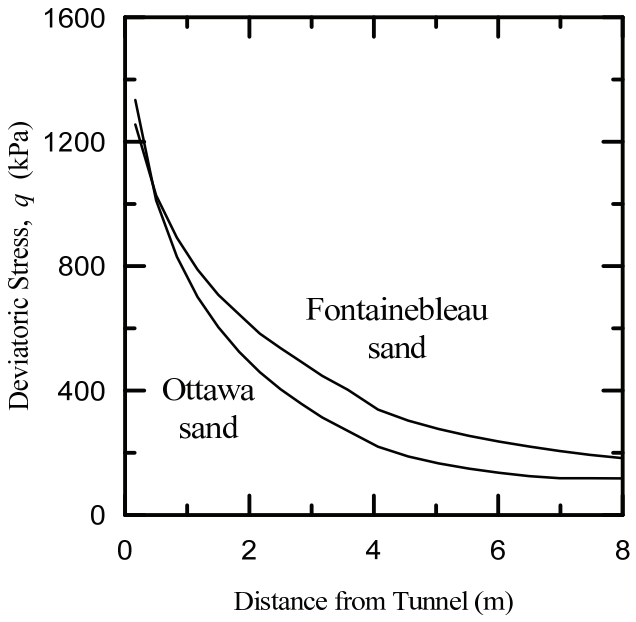

Figure 3.14. Maximum shear stress versus distance from a 10 m deep tunnel subjected to a C4 explosive of radius 0.05 m

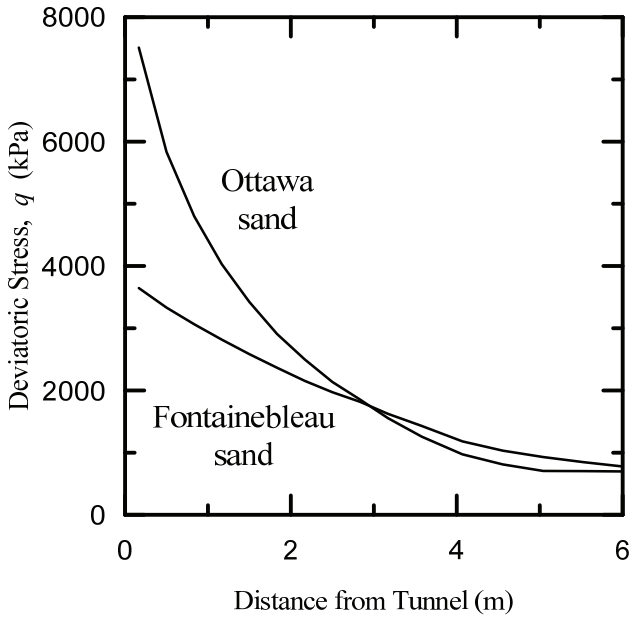

Figure 3.15. Maximum shear stress versus distance from a 10 m deep tunnel subjected to a C4 explosive of radius 0.1 m

Figures 3.16 and 3.17 show the variation of the maximum strain rate experienced by different points along the horizontal path described in Figure 3.8. The major principal strain ε_1 is plotted in these figures. The dissipation of the strain rates is greater in Ottawa sand than in Fontainebleau sand.

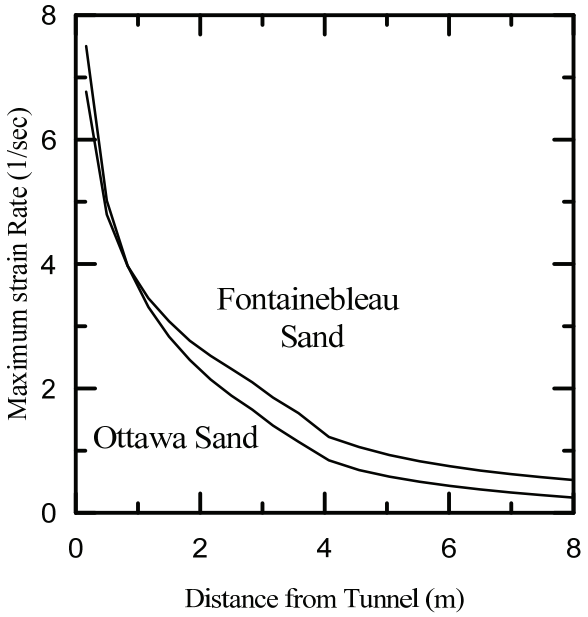

Figure 3.16. Maximum strain rate versus distance from 10 m deep tunnel subjected to a C4 explosive with radius 0.05 m

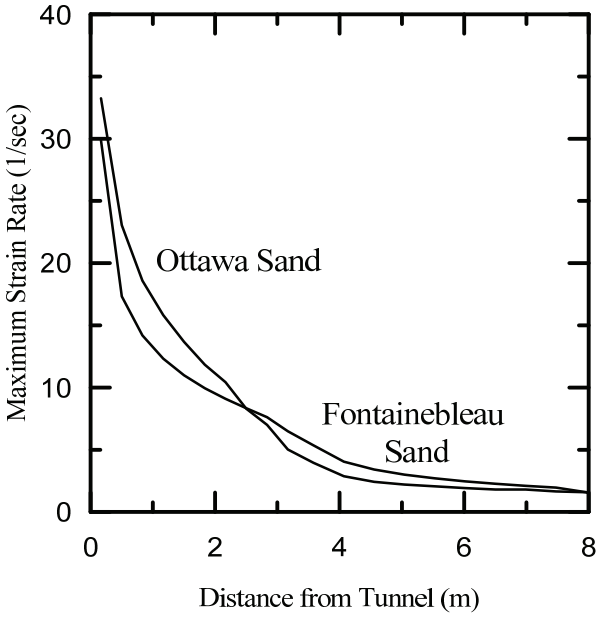

Figure 3.17. Maximum strain rate versus distance from a 10 m deep tunnel exploded with C4 of radius 0.10 m

Figures 3.18 and 3.19 show the mean stress versus shear stress (p'-q) plots of the soil element immediately adjacent to the tunnel and lying on the path shown in Figure 3.8 due to different charges of the C4 explosive. The soil element immediately adjacent to the tunnel was chosen because it experiences the greatest stresses and strain rates out of all the elements along this path.

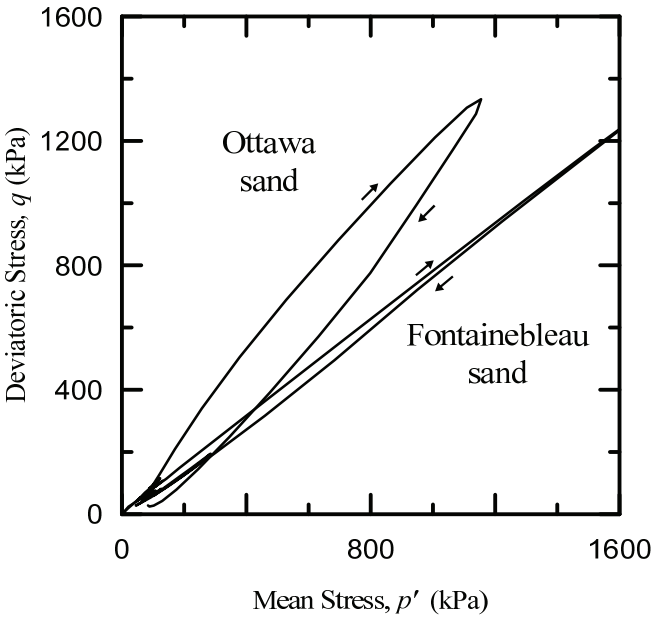

Figure 3.18. Mean stress versus shear stress at the soil element horizontally adjacent to a 10 m deep tunnel exploded with C4 of radius 0.05 m

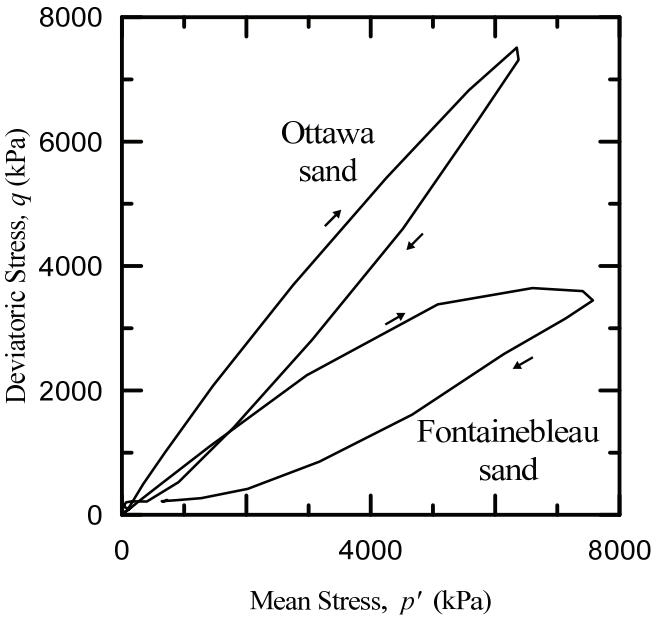

Figure 3.19 Mean stress versus shear stress at the soil element horizontally adjacent to a 10 m deep tunnel exploded with C4 of radius 0.1 m

Figures 3.20-3.23 show the void ratio versus mean stress (*e*-*p′*) plots for the two sands considered in the study. These results were obtained for the same element adjacent to the tunnel for which the *p′*-*q* plots were obtained in Figures 3.14-3.19.

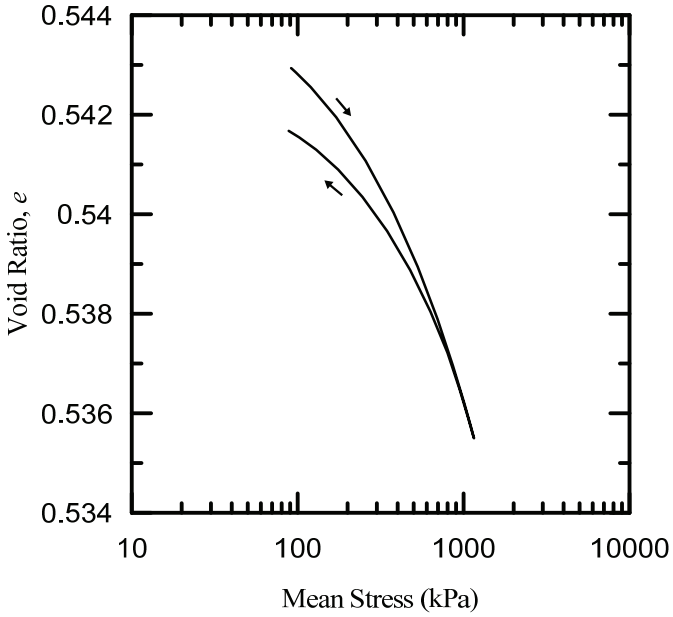

Figure 3.20. Mean stress versus void ratio at the soil element horizontally adjacent to a 10 m deep tunnel in Ottawa Sand blasted with C4 of radius 0.05 m

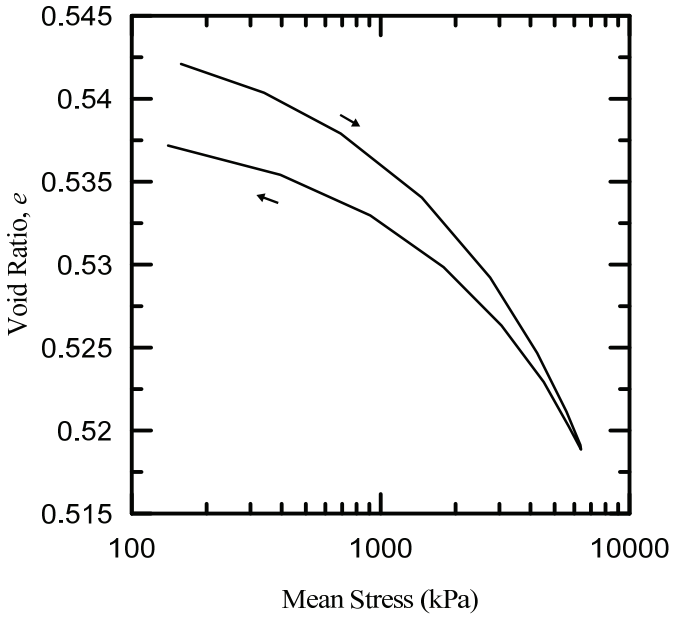

Figure 3.21. Mean stress versus void ratio measured at the soil element horizontally adjacent to a 10 m deep tunnel in Ottawa Sand exploded with C4 of radius 0.10 m

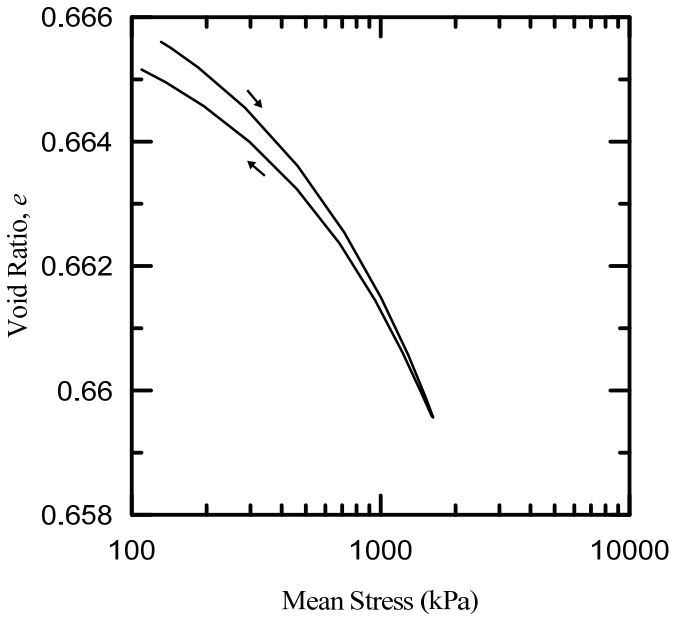

Figure 3.22. Mean stress versus void ratio measured at the soil element horizontally adjacent to a 10 m deep tunnel in Fontainebleau Sand exploded with C4 of radius 0.05 m

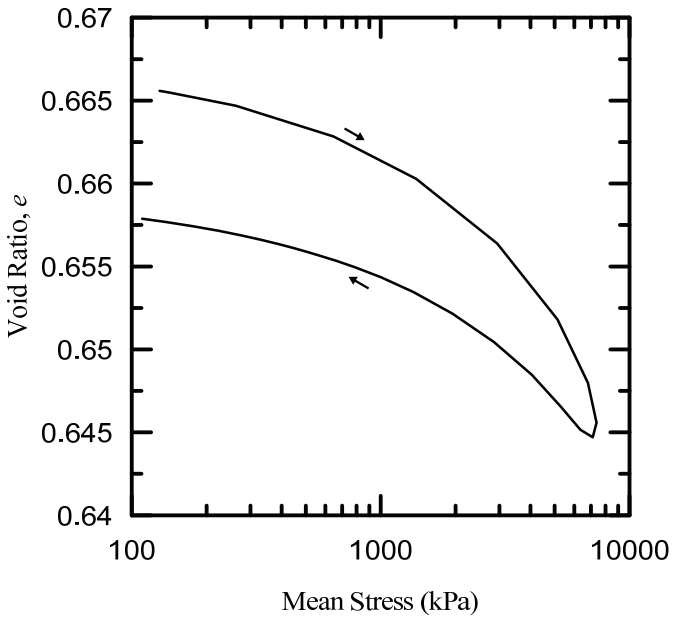

Figure 3.23. Mean stress versus void ratio measured at the soil element horizontally adjacent to a 10 m deep tunnel in Fontainebleau Sand exploded with C4 of radius 0.10 m

3.2.3 Effect of Tunnel Depth

The effect of tunnel depth is shown in Figures 3.24-3.29. Simulations were performed with tunnels in Ottawa sand that had their centroids at the depths of 10 m and 5 m. Figures 3.24 and 3.25 show the spatial variation of the maximum mean stress with distance from the tunnel along the horizontal path shown in Figure 3.8. The mean stress dissipates more quickly for the shallower tunnel. This is in part due to the lower confining stress around the shallower tunnel which results in lower values of the elastic modulus causing more plastic strains. Another possible cause for faster stress dissipation in the shallower tunnel is that it is closer to the ground surface which is effectively a free surface allowing the soil to displace rather than resisting the stress wave.

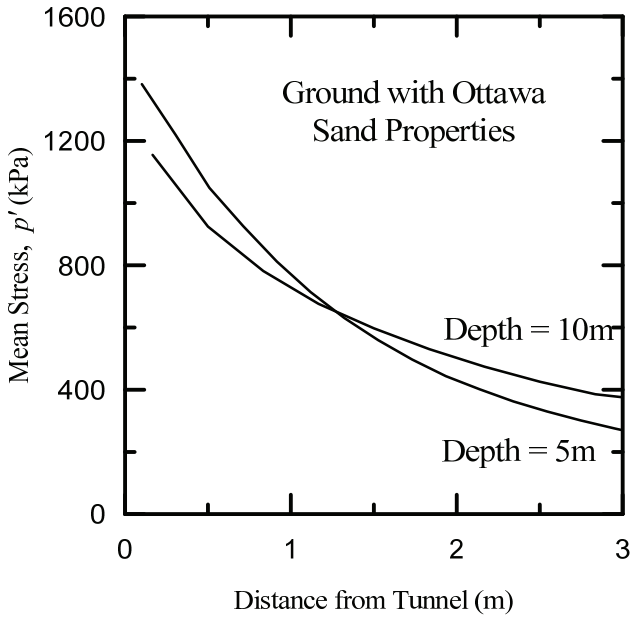

Figure 3.24. Maximum mean stress versus distance from a 5 or 10 m deep tunnel subjected to C4 explosive of radius 0.05 m

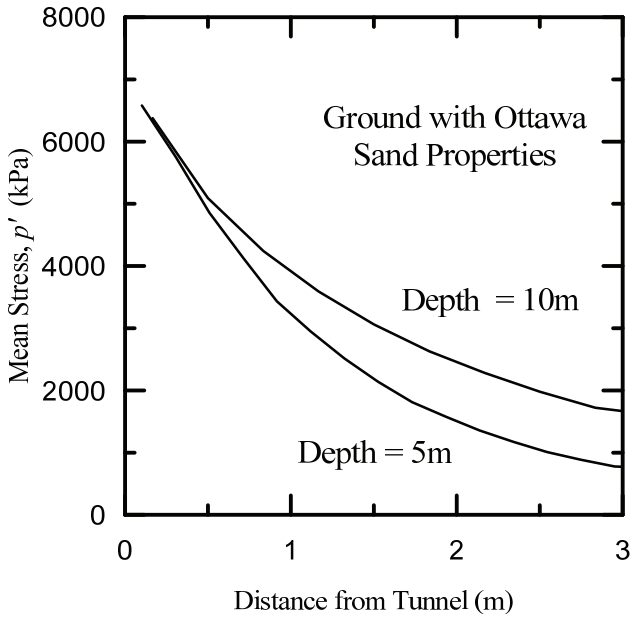

Figure 3.25. Maximum mean stress versus distance from a 5 or 10 m deep tunnel subjected to C4 explosive of radius 0.1 m

The maximum shear stress experienced at different points along the horizontal path described in Figure 3.8 is presented in Figures 3.26 and 3.27. The spatial dissipation of the shear stress is faster for the shallower tunnel.

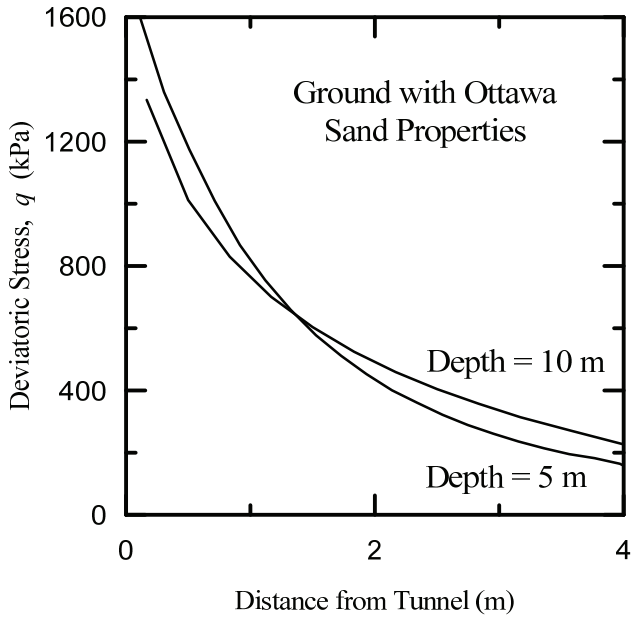

Figure 3.26. Maximum shear stress versus distance from a 5 or 10 m deep tunnel subjected to C4 explosive of radius 0.05 m

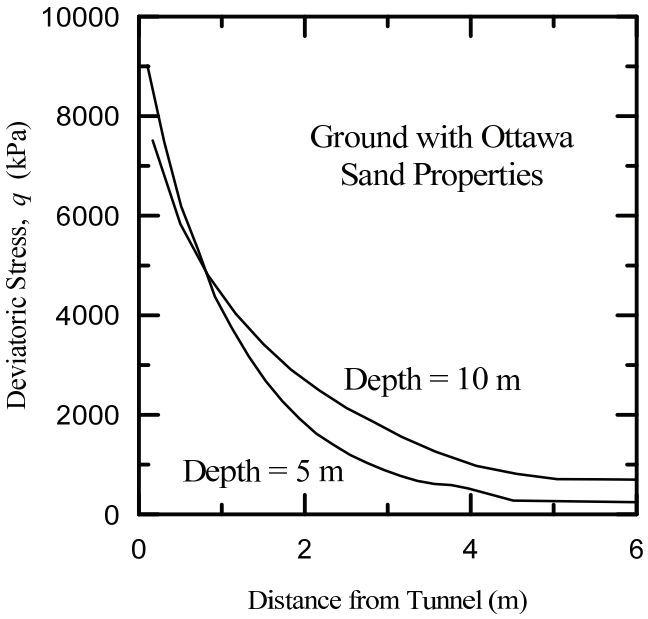

Figure 3.27. Maximum shear stress versus distance from a 5 or 10 m deep tunnel subjected to C4 explosive of radius 0.10 m

Figures 3.28 and 3.29 show the maximum rate of the major principal strain ε_1 experienced at different points along the horizontal path described in Figure 3.8. The strain rate is significantly greater in the ground adjacent to the 5 m deep tunnel. A reason for greater strain rate is the lower confining stress on the soil elements which results in a lesser modulus that allows more straining under the same amount of stress. Additionally, the lower elastic moduli results in a slower wave speed causing the material points to be loaded for longer periods of time, which also results in greater strains.

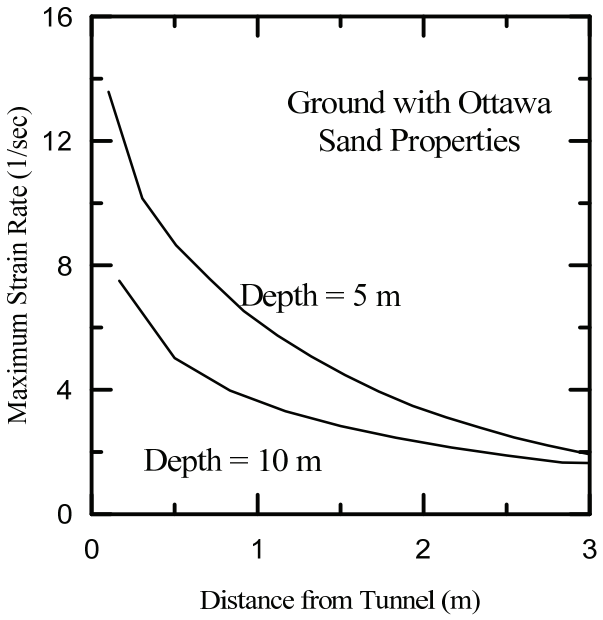

Figure 3.28. Maximum strain rate versus distance from a 5 or 10 m deep tunnel subjected to C4 explosive of radius = 0.05 m at the tunnel center

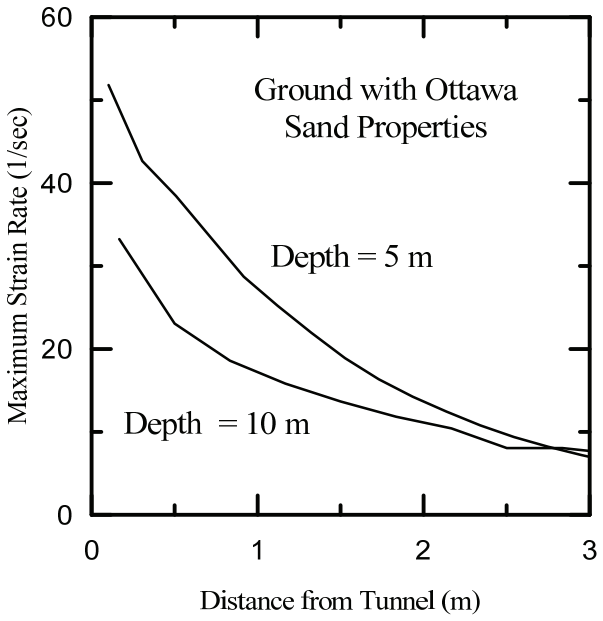

Figure 3.29. Maximum strain rate versus distance from a 5 or 10 m deep tunnel subjected to C4 explosive of radius 0.1 m

Figures 3.30 and 3.31 show the *e-p′* response of the soil element immediately adjacent to the tunnel on the horizontal path described in Figure 3.8. The soil element adjacent to the shallower tunnel experiences the greatest pressure of all elements along the horizontal path (see Figures 3.20 and 3.21) and therefore is expected to develop maximum plastic strains.

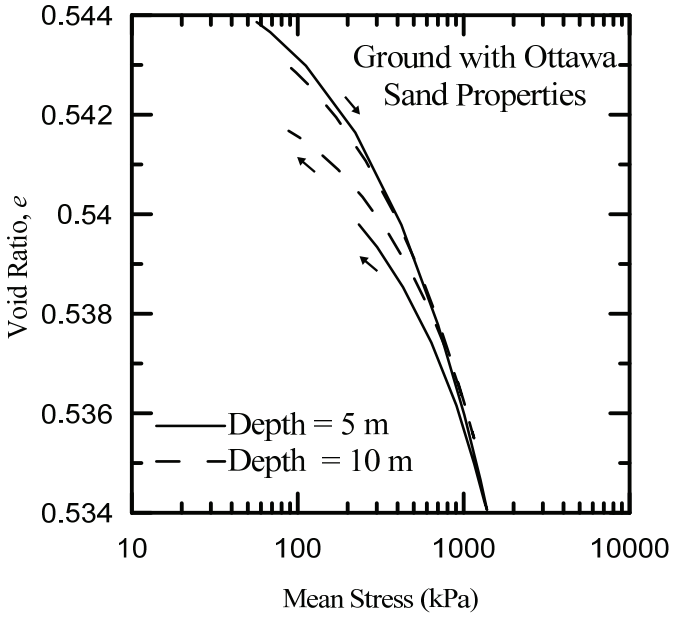

Figure 3.30. Mean stress versus void ratio measured at the soil element horizontally adjacent to a 5 or 10 m deep tunnel in Ottawa Sand exploded with C4 of radius 0.05 m

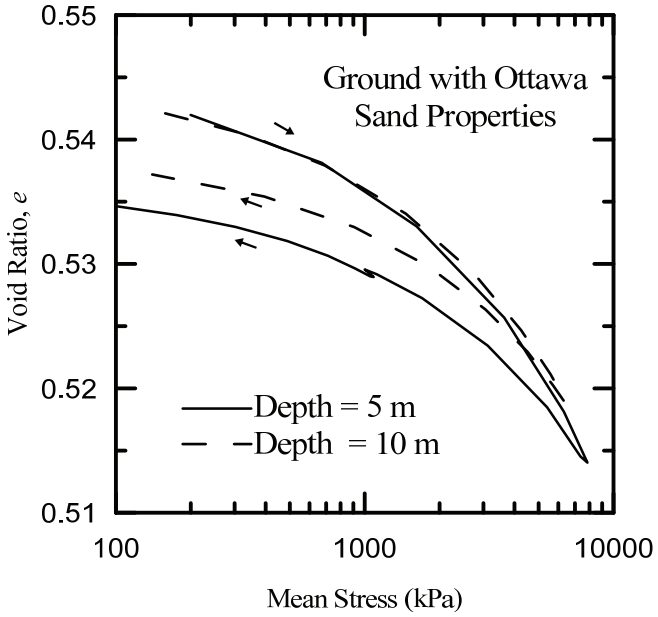

Figure 3.31. Mean stress versus void ratio measured at a soil element horizontally adjacent to a 5 or 10 m deep tunnel in Ottawa Sand exploded with C4 of radius 0.1 m

Figures 3.30 and 3.31 demonstrate the difference in the development of plastic strains in the soil adjacent to the two tunnels at different depths. The stress path in the case of the shallower tunnel unloads to a void ratio that is denser than that of the deeper tunnel. This is indicative of the development of greater volumetric plastic strains around the shallower tunnel. Greater initial confining pressure of the deeper tunnel resulting in greater bulk modulus contributes to this difference.

3.3 Conclusions

This chapter demonstrates the implementation of the constitutive model developed in chapter 2 in a finite element framework. By simulating an explosion inside a tunnel and analyzing the waves propagated through the soil it was shown how the different constitutive model parameters produce different ground response. The type of soil, the amount of explosion and the depth of the tunnel influence the response of ground surrounding the tunnels.

CHAPTER 4 - RESEARCH SUMMARY AND FUTURE DIRECTIONS

4.1 Research Summary

In this thesis, a constitutive model was developed which is capable of simulating the high strain-rate behavior of sands under multi-axial loading conditions. The model is developed from the modified Manzari-Dafalias two-surface plasticity model in conjunction with Perzyna's overstress theory of viscoplasticity (Perzyna 1963, 1966). The developed model is capable of distinguishing and simulating contractive and dilative sands that occur under different pressures and void ratios. The parameters of the model were calibrated to simulate the mechanical behavior of Ottawa and Fontainebleau sands. The critical state parameters of the model were adjusted to account for the large pressures (> 100MPa) experienced in the split Hopkinson pressure bar tests and during blast loading in soil. The model was implemented in the commercial finite element code Abaqus through user material subroutine and was used to analyze static and transient problems. A semi-implicit Backward-Euler algorithm was used to implement the model in Abaqus. Static drained triaxial tests and dynamic split Hopkinson pressure bar tests on Ottawa and Fontainebleau sands were simulated as validation of the model.

The constitutive model was subsequently applied in two dimensional (plane strain) finite element analysis of tunnels subject to blast. It was assumed that circular underground tunnels constructed in sandy soils were subjected to blast caused by the

explosion of C4. The blast was simulated using the JWL explosion model from which the pressure due to the blast acting on the inner tunnel lining as a function of time was obtained. This information was passed onto the finite element analyses of the tunnels which were performed with the assumption that the ground properties were similar to those of Ottawa or Fontainebleau sand.

It was found that the type of sand affected the propagation of the stress wave through the ground. The ground consisting of Ottawa sand, which had shown a greater degree of rate dependence and which was calibrated with a higher viscosity parameter, experienced greater plastic strains and was able to dissipate the stresses faster over a shorter distance. Also, the stress took longer time and distance to dissipate for deeper tunnels — this occurred because the soil modulus increased with depth due to an increase in the confining pressure. Further, it was observed that greater quantities of explosive generated greater magnitudes of blast waves which resulted in greater amounts of plastic strain in the soil.

4.2 Future Directions

In this analysis, the JWL loading was not coupled with the propagation of the stress wave through the soil model. In future studies, the use of JWL loading fully coupled with the finite element analysis may be considered for increased accuracy.

A simplification made in this research is the consideration of the boundary value problem as a plain strain problem. The rather unrealistic geometry of an infinitely long explosive creates difficulties in finding a suitable practical case to compare with. In the future simulations, it would be advantageous to study three-dimensional geometries so as to simulate a more realistic problem. The analysis could then be evaluated against other

studies. Tunnels of different geometries and tunnels in layered and sloping grounds may also be studied in the future.

This analysis dealt with the propagation of wave in soil due to blast in tunnels. In the future, several other boundary value problems may be studied using the developed constitutive model. Examples of practical problems that may be analyzed include blast in embankments and other vulnerable geo-structures, projectiles penetrating the ground and other geo-structures, blast loading directly on the soil and pile driving.

REFERENCES

1. Abaqus v6.9 user's manual (2009), *Abaqus Inc., DS Simulia*, Providence, RI, USA.

2. Adachi, T., and Okano, M. (1974). "A constitutive equation for normally consolidated clay." *Soils and Foundations*, vol. 14, p. 55–73.

3. Adachi, T., Oka, F., and Mimura, M. (1987). ''Mathematical structure of an overstress elasto-viscoplastic model for clay.'' *Soils and Foundations*, vol.27 (3), p. 31–42.

4. Adachi, T., Oka, F., and Poorooshasb, H. B. (1990). ''A constitutive model for frozen sand.'' *Transactions of the ASME*, vol.112, p. 208–212.

5. Adachi, T., Oka, F., and Mimura, M. (1996). ''State of the art: Modeling aspects associated with time dependent behavior of soils.'' *Measuring and modeling time dependent soil behavior, ASCE, Geotechnical Special Publication No. 61* (T. C. Sheahan and V. N. Kaliakin, eds.), New York, p. 61–95.

6. Adachi, T., Oka, F., and Zhang, F. (1997). ''An elasto-viscoplastic constitutive model with strain softening.'', *Numerical Models in Geomechanics* (S. Pietruszczak and G. Pande, eds.), Balkema, Rotterdam, The Netherlands, p. 81–86.

7. Been, K. and Jefferies, M. G. (1985). “A state parameter for sands.” *Géotechnique*, Vol. 35 (2), p. 99-112.

8. Bessette, G. C.(2008). “Modeling blast loading on buried reinforced concrete structures with Zapotec”, *Journal Shock and Vibration*, vol.15 (2), p. 137-146.

9. Borja, R. I. (1992). ‘‘Generalized creep and relaxation model for clays.’’ *Journal of Geotechnical Engineering*, *ASCE,* vol.118 (11), p. 1765–1786.

10. Borja, R. I., and Kavazanjian, E. (1985). ‘‘A constitutive model for the stress–strain–time behaviour ‘‘wet’’ clays.’’ *Géotechnique*, vol.35 (3), p. 283–298.

11. Borja, R. I., Kavazanjian, E., Jr., and Hsieh, H. S. (1990). ‘‘Double-yield surface cam-clay plasticity Model: II. Implementation and verification.’’ *Journal of Geotechnical Engineering*, *ASCE,* vol.116 (9), p. 1402–1421.

12. Boukpeti, N., Mróz, Z. and Drescher, A. (2002). “A model for static liquefaction in triaxial compression and extension”. *Canadian Geotechnical Journal*, vol.39 (6), p. 1243–1253.

13. Boukpeti, N., Mróz, Z. and Drescher, A. (2004) “Modeling rate effects in undrained loading of sands.” *Canadian Geotechnical Journal*, vol.41 (2), p. 342–350.

14. Carraro, J. A. H. (2004). Mechanical behavior of silty and clayey sands. PhD Dissertation, Purdue University, West Lafayette, Indiana, USA.

15. Casagrande, A., and Shannon, W. L. (1948). “Strength of soils under dynamic Loads.” *Proceedings of the American Society of Civil Engineers*, vol. 74 (4), p.

591–608.

16. Chapra, S. C. and Canale, R. P. (1998). *Numerical methods for engineers*. McGraw-Hill Co.

17. Chakraborty, T. (2009). Development of a clay constitutive model and its application to pile boundary value problems. *PhD thesis,* Purdue University, West Lafayette, Indiana, USA.

18. Charlie, W. A., Dowden, N. A., Villano, E. J., Veyera, G. E., and Doehring, D. O. (2005). "Blast-induced stress wave propagation and attenuation: Centrifuge model versus prototype tests", *Geotechnical Testing Journal,* vol. 28 (2), p. 207-216.

19. Christensen R.W. and Wu T.H. (1964), "Analysis of clay deformation as a rate process", *Journal of Soil Mechanics and Foundation Division, ASCE*, vol. 90 (6), p. 125-157.

20. Cristescu, N. (1991). ''Nonassociated elastic viscoplastic constitutive equations for sand.'' *International Journal of Plasticity*, vol. 6, p. 41–64.

21. Dafalias, Y. F. (1982). ''Bounding surface elastoplasticity-viscoplasticity for particulate cohesive media.'' *International Union of Theoretical and Applied Mechanics Conference on Deformation and Failure of Granular Materials* (P. A. Vermeer and H. J. Luger, eds.), p. 97–107.

22. Dafalias, Y. F. (1986). "Bounding surface plasticity I: Mathematical foundation and hypoplasticity", *Journal of Engineering Mechanics*, vol. 112 (9), p. 966-987.

23. Dafalias, Y. F., Papadimitriou, A. G. and Li, X. S. (2004). "Sand plasticity model accounting for inherent fabric anisotropy." *Journal of Engineering Mechanics*, *ASCE*, Vol. 130 (11), p. 1319-1333.

24. Dafalias, Y. F. and Hermann, L. R. (1982). "Bounding surface formulation of soil plasticity," *Soil Mechanics – Transient and Cyclic Loads*", (eds. Pande and Zienkiewicz), Wiley, New York, p. 253-282.

25. Dafalias, Y. F. and Manzari, M. T. (2004). "Simple plasticity sand model accounting for fabric change effects." *Journal of Engineering Mechanics*, *ASCE*, vol. 130 (6), p. 622- 634.

26. Dafalias, Y. F. and Popov, E. P. (1975). "A model of nonlinearly hardening materials for complex loading." *Acta Mechanica*, Vol. 21 (3), p.173-192.

27. Dano C, Hicher PY, Taillez S. (2004). Engineering properties of grouted sand. *Journal of Geotechnical and Environmental Engineering,* vol. 130 (3), p. 228–238.

28. Davies, R.M., (1948). "A critical study of the Hopkinson Pressure Bar," Philosophical Transactions of the Royal Society of London, A240, p. 375-457.

29. Davies, M. C. R. (1994) "Dynamic soil structure interaction resulting from blast loading.", *Centrifuge 94, Lee and Tan (eds.),* Balkema, Rotterdam.

30. De, A. (2008). "Centrifuge modeling of explosion craters formed over underground structures.", *Geosustainability and Geohazard Mitigation. Proceedings of GeoCongress 2008, ASCE*, New Orleans, Loisiana, USA, p.

311-318

31. De, A. and Zimmie, T. F. (2006). "Modeling of surface blast effects on underground structures.", *Geotechnical Engineering in the Information Technology Age, Proceedings of GeoCongress 2006 , ASCE,* Atlanta, Georgia, USA, p. 208-215.

32. De, A., and Zimmie, T. F. (2007). "Centrifuge modeling of surface blast effects on underground structures.", *Geotechnical Testing Journal, ASTM*., vol.30 (5), p. 427-431.

33. di Prisco, C., Imposimato, S., and Vardoulakis, I. (2000). ''Mechanical modelling of drained creep triaxial tests on loose sand.'' *Géotechnique*, vol. 50 (1), p. 73–82.

34. di Prisco C., Imposimato S., Aifantis E. C., (2002). "A visco-plastic constitutive model for granular soils modified according to non-local and gradient approaches", *International Journal of Numerical and Analytical Methods in Geomechanics,* vol. 26, p. 121-138.

35. Desai, C. S., and Zhang, D. (1987). ''Viscoplastic model for geological materials with generalized flow rule.'' *International Journal of Numerical and Analytical Methods in Geomechanics*, vol.11, p. 603–620.

36. Di Benedetto, H., Tatsuoka, F. and Ishihara, M. (2002), "Time-dependent deformation characteristics of sand and their constitutive modeling", *Soils and Foundations*, vol.42 (2), p. 1-22.

37. di Prisco, C., and Imposimato, S. (1996). ‘‘Time dependent mechanical behaviour of loose sands.’’ *Mechanics of Cohesive-Frictional Materials*, vol.1 (1), p.45–73.

38. di Prisco C., Imposimato S., (2003). “Non local numerical analyses of strain localization in dense sand.” *Mathematical and Computer Modelling*, vol.37, p. 497-506.

39. Drucker, D.C. and Prager, W. (1952), “Soil mechanics and plastic analysis or limit design.” *Quarterly of Applied Mathmatics,*, vol. 10, 157-165.

40. Einav, I. and Randolph, M. F. (2005). “Combining upper bound and strain path methods for evaluating penetration resistance.” *International Journal for Numerical Methods in Engineering,* vol.63 (14), p. 1991 – 2016.

41. Feldgun, V.R., Kochetkov, A.V., Karinski, Y.S., and Yankelevsky, D.Z. (2008a). “Internal blast loading in a buried lined tunnel”, *International Journal of Impact Engineering*, vol.35, p.172–183.

42. Feldgun, V.R., Kochetkov, A.V., Karinski, Y.S. and Yankelevsky, D.Z. (2008b). “Blast response of a lined cavity in a porous saturated soil”, *International Journal of Impact Engineering*, vol.35(9), p.953-966.

43. Fragaszy, R. J.and Taylor, T. (1989). “Centrifuge modeling for projectile penetration studies.” *Geotechnical Testing Journal*, vol.12 (4), p.281-287.

44. Gaudin, C., Thorel, J. L., Garnier, J., and Serratrice, J.-F. (2003). “Modelling in triaxial cells of the behavior of a soil of a restraining structure” *Deformation characteristics of geomaterials; Proceedings of the third international*

symposium on deformation characteristics of Geomaterials; IS Lyon, Framce, p. 669-675.

45. Hardin, B. O. and Richart, F. E., Jr. (1963). "The nature of stress-strain behavior of soils." *Journal of Soil Mechanics and Foundations Division, ASCE,* vol. 89 (1), 33-65.

46. Herrman, L. R., Kaliakin, V., Shen, C. K., Mish, K. D. and Zhu, Z-Y (1987). Numerical implementation of plasticity model for cohesive soil. *Journal of Engineering Mechanics*, vol. 113 (4) p. 500-519.

47. P. Y. Hicher, C. S. Chang and C. Dano, (2008). "Multi-scale modeling of grouted sand behavior," *International Journal of Solids and Structures, Pergamon Press,* Vol. 45, (16), p. 4362 – 4374.

48. Holsapple, K.A. and Schmidt, R.M. (1980). "On the scaling of crater dimensions. I. Explosive processes", *Journal of Geophysical Research*, vol.85 (B12), p. 7247-7256.

49. Holsapple, K.A. and Schmidt, R.M. (1982). "On the scaling of crater dimensions. II. Impact processes", *Journal of Geophysical Research*, vol.87 (B3), p.1849-1870.

50. Hopkinson, B., (1914). "A method of measuring the pressure in the deformation of high explosives or by the impact of bullets " *Philosophical Transactions of the Royal Society of London,* A213, 437-452.

51. Hsieh, H. S., Kavazanjian, E., and Borja, R. I. (1990). ''Double-yield surface cam-

clay plasticity model. I: Theory.'' *Journal of Geotechnical Engineering*, *ASCE,* vol.116 (9), p.1381–1401.

52. Jung, B. C. and Biscontin, G. (2006). "Modeling of strain rate effects on clay in simple shear", *Proceedings of GeoCongress 2006, ASCE,* Atlanta, Georgia, USA, p.1-6.

53. Kaliakin, V. N. (1985). "Bounding surface elastoplasticity viscoplasticitv for clays." *PhD dissertation*, University of California.

54. Kaliakin, V. N. and Dafalias, Y. F. (1990a). "Theoretical aspects of the elastoplastic-viscoplastic bounding surface model for cohesive soils." *Soils and Foundations*, vol. 30 (3), p.11-24.

55. Kaliakin, V. N. and Dafalias, Y. F. (1990b). "Verification of the elastoplastic-viscoplastic bounding surface model for cohesive soils" *Soils and Foundations*, vol. 30 (3), p. 25-36.

56. Kaliakin, V. N. and Dafalias, Y. F. (1991). "Details regarding the elastoplastic-viscoplastic bounding surface model for isotropic cohesive soils", *Civil Engineering Report No. 91-1*, University of Delaware, Newark, Delaware.

57. Karinski, Y. S., Feldgun, V. R. and Yankelevsky, D. Z. (2008). "Explosion-induced dynamic soil-structure interaction analysis with the coupled Godunov-variational difference approach", *International Journal for Numerical Methods in Engineering*, vol.77(6), p.824 – 851.

58. Kolsky, H., (1949). "An investigation of the mechanical properties of materials at

very high rates of strain," *Proceedings of the Physical Society.,* B 62 p.676-700

59. Krieg R D. (1972) "A simple constitutive description for cellular concrete." *Albuquerque, USA: Sandia National Laboratories.*

60. Krieg, R. D. (1975). "A practical two-surface plasticity theory." *Journal of Applied Mechanics*, vol. 42, p. 641-646.

61. Kutter, B. L., and Sathialingam, N. (1992). "Elastic-viscoplastic modeling of the rate-dependent behavior of clays." *Géotechnique*, vol. 42 (3), p. 427–441.

62. Kutter, B.L., O'Leary, L. M., Thompson, P. Y. and Lather, R. (1988). "Gravity-scaled tests on blast induced soil-structure interaction." *Journal of Geotechnical Engineering, ASCE*, vol. 114 (4), p. 431-447.

63. Laine, P. and Sandvik. A. (2001). "Derivation of mechanical properties for sand.", *Proceedings of the 4th Asia–Pacific conference on Shock and Impact Loads on Structures.* Singapore, p.361–368.

64. Larcher, M., Casadei, F., (2010). "Explosions in complex geometries - a comparison of several approaches." *International Journal of Protective Structures*, vol.1 (2), p. 169–195.

65. Lee, E. L., Finger, M., and Collins, W. (1973). ''JWL equation of state coefficients for high explosives,'' *Technical Report UCID-16189*, Lawrence Livermore National Laboratory, Livermore, CA.

66. Lee, K. L., Seed, H. B., and Dunlop, P. (1969). "Effect of transient loading on the strength of sand." *Proc., 7th Int. Conf. on Soil Mech. and Found. Engrg.,*

Mexico City, Mexico, p. 239-247.

67. Li, X. S. & Wang, Y. (1998). Linear representation of steady-state line for sand. *Journal of Geotechnical and Geoenvironmental Engineering*, ASCE, 124, (12), p. 1215- 1217.

68. Li X. S. and Dafalias Y. F. (2002) "A sand model with state-dependent dilatancy." *Géotechnique,* vol. 52 (3), p 173–186.

69. Li X. S. and Dafalias Y. F. (2000) "Dilatancy of cohesionless soils." *Géotechnique,* vol. 50 (4), p 449–460.

70. Loukidis, D. (2006). "Advanced constitutive modeling of sands and applications to foundation engineering.", *PhD thesis*, Purdue University, West Lafayette, USA.

71. Loukidis D, Salgado R. (2009) Modeling sand response using two-surface plasticity. *Computers & Geotechnics*; vol. 36(1–2), p. 166–186.

72. Lu, Y., Wang, Z. and Chong, K. (2005). "A comparative study of buried structure in soil subjected to blast load using 2D and 3D numerical simulations." *Soil Dynamics and Earthquake Engineering*, vol.25, p.275–288.

73. Lubliner, J. (2005) "Plasticity Theory", Revised edition (PDF), *University of California at Berkley*.

74. Luong, M.P., (1980), Stress-strain aspects of cohesionless soils under cyclic and transient loading, *in Pande, G.N., and Zienkiewicz, O.C., eds., Proceedings of International Symposium on Soils under Cyclic and Transient Loading*:

Rotterdam, Netherlands, A.A. Balkema, p. 315–324.

75. Manzari, M. T. and Dafalias, Y. F. (1997). "A critical state two-surface plasticity model for sands." *Géotechnique*, vol. 47(2), p. 255-272.

76. Martindale, H. F. (2011). ") Rate dependent behavior of clay." *Master Thesis*. University of Connecticut, Storrs, Connecticut.

77. Mitchell, J. K. and Soga, K. (2005). "Fundamentals of soil behavior", Edition 3, *John Wiley & Sons, Inc*, 592p.

78. Murayama, S., and Shibata, T. (1961). ''Rheological properties of clays.'' *Proceedings of 5th International Conference on Soil Mechanics and Foundation Engineering*, vol.1, p.269–274.

79. Murthy, T. G., Loukidis, D., Carraro, J. A. H, Prezzi, M. & Salgado, R. (2006). Undrained monotonic behavior of clean and nonplastic silty sands. *Géotechnique, vol* 57 (3), p. 273–288.

80. Naghdi, P. M., and Murch, S. A. (1963). ''On the mechanical behavior of viscoelastic/plastic solids.'' *Journal of Applied Meteorology*, vol.30, p.321–328.

81. Nagy, N. M., Eltehawy, E.A., Elhanafy, H.M., Eldesouky,A (2009). "Numerical modelingModeling of geometrical analysisGeometrical Analysis for underground structuresUnderground Structures*." 13th International Conference on aerospace sciences & aviation technology , ASAT- 13,* May 26 – 28, 2009, Military Technical College, Kobry Elkobbah, Cairo, Egypt

82. Nagy, N., Mohamed, M., Boot, J.C., (2010) "Nonlinear numerical modeling for the effects of surface explosions on buried reinforced concrete structures." *Geomechanics and Engineering*, vol. 2, (1), p.1-18

83. Nash, K. L. and Dixon, R. K. (1961). "The measurement of pore pressure in sand under rapid triaxial test." *Proceedings of the Conference on "Pore Pressure and Suction in Soils",* Butterworths, London. p. 21-25.

84. Oka, F., and Adachi, T. (1985). ''An elasto-plastic constitutive equation of geologic materials with memory.'' *Proceedings of 5th International Conference on Numerical Methods in Geomechanics*, p.293–300.

85. Oka, F., Adachi, T. and Mimura M. (1988). ''Elasto-viscoplastic constitutive models for clays.'' *Proceedings of International Conference on Rheology and Soil Mechanics*, Elsevier, Science, New York, p. 12–28.

86. Oka, F., Adachi, T., Yashima, A. (1994) " Instability of an elasto-viscoplastic constitutive model for clay and strain localization", *Mechanics of Materials*, vol.18, p.119–129.

87. Oka, F., Higo, Y. and Kimoto, S. (2002). "Effect of dilatancy on the strain localization of water-saturated elasto-viscoplastic Soil." *International Journal of Solids and Structures,* vol. 39, p. 3625–3647.

88. Oka, F., Kodaka, T. and Kim, Y. (2004). "A cyclic viscoelastic-viscoplastic constitutive model for clay and liquefaction analysis of multi-layered ground.", *International Journal for Numerical and Analytical Methods in Geomechanics*,

vol. 28 (2), p. 131-179.

89. Olszak, W., and Perzyna, P. (1966a). ‘‘On elastic-viscoplastic soils, rheology and soil mechanics.’’ *International Union of Theoretical and Applied Mechanics Symposium, Grenoble*, Springer, Berlin.

90. Olszak, W., and Perzyna, P. (1966b). ‘‘The constitutive equations of the flow theory for a nonstationary yield condition.’’ *Proceedings of 11th International Congress of Applied Mechanics*, Springer, Berlin, p.545–553.

91. Olszak, W., and Perzyna, P. (1970). Stationary and nonstationary viscoplasticity, McGraw-Hill, New York [Kanninen, F. (1969) ‘‘Inelastic behavior of solids.’’ Battelle Institute Materials of Science Colloquia, Columbus and Atwood Lake, Ohio], p.53–75.

92. Ortiz, M. and Simo, J. C. (1986), “An analysis of a new class of integration algorithms for elastoplastic constitutive relations”. *International Journal for Numerical Methods in Engineering,* vol.23, p.353-366.

93. Perzyna, P. (1963). “The constitutive equations for rate sensitive plastic materials.” *Quarterly of Applied Mathematics,* vol. 20, p. 321-332.

94. Perzyna, P. (1966). “Fundamental problems in viscoplasticity.”, *Advances in Applied Mechanics*, vol. 9, p. 244–377.

95. Pierce, S. J., (1989). “High intensity compressive stress wave propagation Intensity Compressive Stress Wave Propagation through unsaturated sands.” *Master’s Thesis*, Colorado State University, Fort Collins, Co.

96. Preece, D. S., Weatherby, J. R., Blanchat, T. K., Davie, N. T., Calderone, J. J., Togami, T. C. and Benham, R. A. (1998). "Computer and centrifuge modeling of decoupled explosions in civilian tunnels." *Report: Sandia National Laboratories*, Albuquerque, NM, USA.

97. Roscoe, K. H. & Burland, J. B. (1968). "On the generalized behavior of 'wet' clay." *Engineering Plasticity*, (eds. J. Heyman & F.A. Leckie), Cambridge University Press, 535-609.

98. Roscoe, K. H., Schofield, A. N. & Wroth, C. P. (1958). "On the yielding of soils." *Géotechnique*, vol. 8, No. 1, 22-53.

99. Savvidou, C., Schofield, A.N . (1986). " Centrifuge and laboratory tests, modeling the penetrator concept for the disposal of HGW in deep ocean sediments." Department of the Environment, London (United Kingdom). Radioactive Waste Management Research Programme ; Cambridge Univ. (United Kingdom). Dept. of Engineering

100. Schmidt, R.M., Holsapple, K.A. (1980). "Theory and experiments on centrifuge cratering." *Journal of Geophysical Research*, vol.85 (B1), p. 235-252.

101. Seed, H. B. and Lundgren, R. (1954). "Investigation of the effect of transient loading on the strength and deformation characteristics of saturated sands.", *Proceedings of 57th Annual Meeting of the Society*, *ASTM,* West Conshohocken, Pennsylvania, no. 54, p. 1288-1306.

102. Sekiguchi, H. (1984). ''Theory of undrained creep rupture of normally consolidated clay based on elasto-viscoplasticity.'' *Soils and Foundations*, vol.24 (1), p.

129–147.

103. Semblat JF, Luong MP, Gary G (1999). “) 3d-Hopkinson bar: new experiments for dynamic testing on soils.”. *Soils and Foundations* vol. 39 (1) p. 1-10.

104. Semblat, J. F., Gary, G. and Luong, M.P. (1995). “Dynamic response of sand using 3D-Hopkinson bar”, *Proceedings of 1st International Conference on Earthquake Geotechnical Engineering*, Tokyo, p. 14-16.

105. Sheahan TC. (1991). “An experimental study of the time-dependent undrained shear behavior of resedimented clay using automated stress path equipment.”. *Sc.D Thesis,* MIT, Cambridge, MA.

106. Sloan, S. W. and Booker, J. R. (1992). Integration of Tresca and Mohr-Coulomb constitutive relations in plane strain elastoplasticity. *International Journal for Numerical Methods in Engineering*, vol.33 (1), p.163-196.

107. Tasneem, N. (2005). “Study of the wave shaping techniques of the Split-Hopkinson Pressure Bar using finite element analysis.” *Master’s Thesis*, Witchita State University. Witchita, Kansas.

108. Tatsuoka, F., de Magistris, F. S., Hayano, K. Momoya, Y., and Koseki J. (2000). ‘‘Some new aspects of time effects on the stress strain behaviour of stiff geomaterials.’’ *Proceedings of 2nd Symposium on Geotechnical Engineering on Hard Soils-Soft Rocks conference, Napoli (A. Evangelista and L. Picarelli, eds.),* Balkema, Rotterdam, The Netherlands, vol. 2, p. 1285–1371.

109. Tatsuoka,F., Ishihara,M., Di Benedetto, H. and Kuwano,R. (2002), “Time-

dependent deformation characteristics of geomaterials and their simulation", *Soils and Foundations*, vol.42(2), 103-129.

110. Tong, X. and Tuan, C. (2007). "Viscoplastic cap model for soils under high strain rate loading". *Journal of Geotechnical and Geoenvironmental Engineering*, *ASCE*, vol. 133 (2), p. 206-214.

111. Veyera, G.E. and Ross, C.A. (1995). "High strain rate testing of unsaturated sands using a split-Hopkinson pressure bar", *Proceedings of 3rd International Conference on Recent Advances in Geotechnical Earthquake Engineering and Soil Dynamics*, St-Louis, USA, p. 31-34.

112. Wang, Z., Hao, H. and Lu, Y. (2004). "A three-phase soil model for simulating stress wave propagation due to blast loading", *International Journal of Numerical and Analytical Methods in Geomechanics*, vol.28, p. 33–56.

113. Whitman, R. V. and Healy, K. A. (1962). "Shear strength of sands during rapid loading," *Journal of the Soil Mechanics and Foundations Division*, *ASCE,* vol. 88 (SM2), p. 99-132.

114. Wu, X. J., Gorham, D. A. (1997). "Stress equilibrium in the split Hopkinson pressure bar test". *Journal de Physique IV* vol. 7 (C3), p. 91-96.

115. Yamamuro, J. A. and Abrantes, A. E. (2003). "Behavior of medium sand under very high strain rates." *Proceedings of 1st Japan-U. S. Workshop on Testing, Modeling, and Simulation*, Boston, MA, USA, p. 61-70.

116. Yamamuro, J. A., and Lade, P. V. (1993). "Effects of strain rate on instability of

granular soils." *Geotechnical Testing Journal*, vol.163, p. 304–313.

117. Yang, Y., Xie, X. Wang, R., (2010). "Numerical simulation of dynamic response of operating metro tunnel induced by ground explosion", *Journal of Rock Mechanics and Geotechnical Engineering,* vol. 2 (4), p373-384.

118. Yu, H.S. (1998). "CASM: A unified state parameter model for clay and sand", *International Journal for Numerical and Analytical Methods in Geomechanics*, vol.22 (8), p. 621-653.

119. Zelikson, A. Boisson, J.Y., Leguay, P., Hembise, O. and Bardey, P. (1986). "Instrumented projectiles in centrifuge modeling of sea bed penetration.", *International Journal of Soil Dynamics and Earthquake Engineering*, vol.5 (4), p. 239-247.

120. Zhou, H. and Randolph, M.F. (2007). "Computational techniques and shear band development for cylindrical and spherical penetrometers in strain-softening clay". *International Journal of Geomechanics*, vol. 7 (4), p. 287–295.

121. Zienkiewicz, O. C. and Cormeau, I. C. (1974). "Viscoplasticity, plasticity and creep in elastic solids: A unified numerical solution approach." *International Journal of Numerical Methods in Engineering*, vol. 8, p. 821–845.

122. Zienkiewicz, O.C., Humpheson, C. and Lewis. R.W. (1975). "Associated and non-associated viscoplasticity and plasticity in soil mechanics." *Géotechnique*, vol. 25, p. 671–689.

APPENDIX A - SPLIT HOPKINSON PRESSURE BAR TEST

The split Hopkinson pressure bar (SHPB) is used to measure the dynamic stress strain behavior of specimens subjected to large strain rates (Al-Mousawi et al. 1997). The split Hopkinson pressure bar uses one dimensional wave propagation through steel cylinders to create uniaxial stress conditions in the material being tested (Tasneen 2005). The split Hopkinson pressure bar experiment can generate strain rates as high as 10^4/second with loading rise times (i.e., the taken for the load to reach its maximum value from zero) as short as 10^{-6} seconds (Pierce 1989).

Hopkinson (1914) developed the original Hopkinson apparatus which measured the maximum stress caused by an explosive force by propagating the wave into a dynamic pendulum. This method did not allow for measurement of the stress-time history of the pulse travelling through the bars. Davies (1948) updated the Hopkinson apparatus by adding a bar condenser unit to measure the displacements at the end of the bar. The stress caused by wave propagation in one dimension is given by the following equation.

$$\sigma = \rho C_0 \frac{\partial u}{\partial t} \tag{A.1}$$

where ρ is the density of the bar, C_0 is the wave speed in the bar and $\partial u / \partial t$ is the particle velocity at a point (u is the displacement and t is the time). Noting that the

particle velocity doubles at the free end of the bar, where the bar condenser is located, due to the compressive wave reflecting back as a tensile wave, the stress can be determined from the readings of the bar condenser as

$$\sigma = \frac{1}{2}\rho C_0 \frac{\partial u}{\partial t} \tag{A.2}$$

Kolsky (1949) modified the Davies bar to allow for the testing of the dynamic stress strain behavior of different materials. The bar, illustrated in Figure A.1, was separated into two pieces (incident and transmitted bars). During an experiment the strain wave magnitude is measured in both the bars before and after it is transmitted through the specimen, which allows for the calculation of the stress and strain histories. The same type of bar condenser is used in this apparatus to measure the displacements on the transmitted bar as was used in the Davies bar. The strain measurements on the incident bar are taken with a cylindrical condenser used to determine the radial strains which are related to the longitudinal strains through Poisson's ratio.

Figure A1. Simplified diagram of experimental set up of split Hopkinson pressure bar apparatus

In an SHPB experiment, a striker bar is fired into the incident bar. As these bars collide they begin to compress at their adjacent ends. The equations for one dimensional wave propagation are derived from Newton's second law:

$$F = M\frac{\partial^2 u}{\partial t^2} \tag{A.3}$$

where F is the force and M is the mass. Taking elemental quantities of force and mass:

$$F = \sigma \partial a \tag{A.4}$$

$$M = \rho \partial V = \rho \partial a \partial x \tag{A.5}$$

where a is the cross sectional elemental area, ∂V is the elemental volume, x is the longitudinal direction and u is longitudinal displacement. Making the assumption that the material of the bar is linear elastic and behaves in accordance with the Hooke's law, the equations for one dimensional wave propagation along the bar can be derived as

$$\frac{\partial^2 u}{\partial x^2} = \frac{1}{C_0^2}\frac{\partial^2 u}{\partial t^2} \tag{A.6}$$

where dx is an elemental length along the bar (Figure A2). The wave speed C_0 along the bar is defined as

$$C_0 = \sqrt{E/\rho} \tag{A.7}$$

where E is the young's modulus of the bar and ρ is the density.

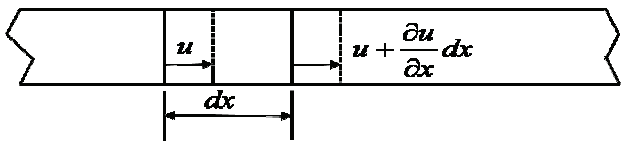

Figure A2. Simplified diagram of one-dimensional wave propagation

The general solution of equation (A.6) yields

$$u = f(x - C_0 t) + g(x + C_0 t) \tag{A.8}$$

where f and g are the functions defining propagation of the wave to the right and left respectively. Considering a wave moving in the positive x direction:

$$u = f(x - C_0 t) \tag{A.9}$$

Differentiation of the above equation leads to

$$v = \frac{\partial u}{\partial t} = -C_0 f' \tag{A.10}$$

and

$$\varepsilon = \frac{\partial u}{\partial x} = f' \tag{A.11}$$

where v is the particle velocity and f' is the derivative of f with respect to the argument $(x - C_0 t)$. Combining equations A.10 and A.11 gives

$$\frac{\partial u}{\partial t} = -C_0 \left(\frac{\partial u}{\partial x} \right) \text{ or } v = -C_0 \varepsilon \tag{A.12}$$

which through Hooke's Law can be written as

$$v = -C_0 \frac{\sigma}{E} = \frac{-\sigma}{\rho C_0} \tag{A.13}$$

This wave propagates down the incident bar until it reaches the sample. At the interface of the incident bar and the sample a portion of the wave is transmitted into the sample and a portion of the wave reflects back into the incident bar as a tensile wave. This splitting of the wave satisfies equilibrium of forces such that

$$(\sigma_I + \sigma_R) A = \sigma_s A_s \tag{A.14}$$

where σ_I is the stress from the incident wave, σ_R is the stress from the wave reflected back into the incident bar and σ_s is the stress transmitted into the sample, A is the area of the incident bar and A_S is the area of the sample. The transmitted stress wave propagates out of the sample into the transmitted bar generating a stress σ_T in the bar. The general shape of the strain waves corresponding to the stresses is presented in Figure A3.

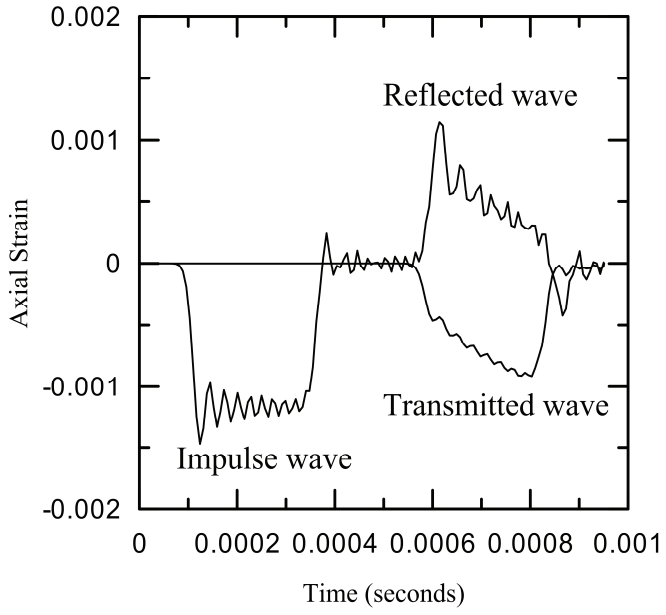

Figure A3. General shape of pulses measured in SHPB analysis

In order to find the stress and strain in the sample, measurements are taken on the bars in such a way that the behavior of the sample is not affected. Given the equilibrium of forces between the sample and the incident bar, the stress at the front edge of the sample can be calculated as

$$\sigma_{S1} = E\frac{A}{A_S}(\varepsilon_I + \varepsilon_R) \tag{A.15}$$

where ε_I and ε_R are the strains associated with the impulse and reflected wave respectively. The stress at the edge of the sample adjacent to the transmitted bar is:

$$\sigma_{S2} = E\frac{A}{A_S}(\varepsilon_T) \tag{A.16}$$

where ε_T is the strain associated with the transmitted wave. An average stress throughout the sample can be obtained as

$$\sigma_S = \frac{EA}{2A_S}(\varepsilon_I + \varepsilon_R + \varepsilon_T) \tag{A.17}$$

Assuming that the contact is maintained between the bars and the sample, the displacement and velocity at the two faces of the sample can be equated to those of the bars (Figure A.4). Thus the strain rate of the specimen can be calculated by the velocities of either end of the sample:

$$\dot{\varepsilon}_S = \frac{v_1 - v_2}{l_0} = \frac{C_0(\varepsilon_I - \varepsilon_R - \varepsilon_T)}{l_0} \tag{A.18}$$

and the strain in the specimen can be found by integrating the strain rate over the elapsed time, t.

$$\varepsilon_S = \int_0^t \dot{\varepsilon}_S = \frac{C_0}{l_0}\int_0^t (\varepsilon_I - \varepsilon_R - \varepsilon_T) \tag{A.19}$$

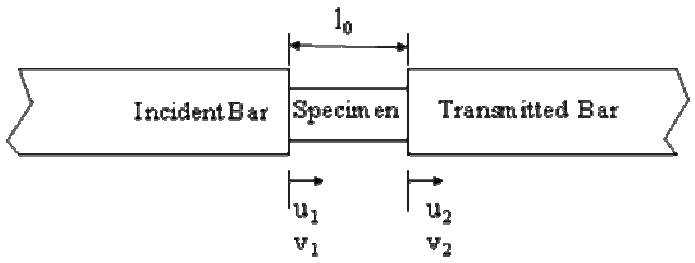

Figure A4. Simplified diagram of interfaces between the bars and the specimen

The assumption that there is stress equilibrium in the specimen (Wu and Gorham 1997) leads to the approximation of the relationship between the instantaneous values of strains in the bars as

$$\varepsilon_I = \varepsilon_T + \varepsilon_R \tag{A.20}$$

This leads to a simplification of equations (A.17), (A.18), and (A.19) as

$$\sigma_S = \frac{EA}{A_s}\varepsilon_T \tag{A.21}$$

$$\dot{\varepsilon}_S = -\frac{2C_0}{l_0}\varepsilon_R \tag{A.22}$$

$$\varepsilon_S = -\frac{2C_0}{l_0}\int_0^t \varepsilon_R \tag{A.23}$$

Using the above equations, the stress versus strain relationship for the material can be plotted for the duration of an experiment.

APPENDIX B - OVERSTRESS FUNCTION

Perzyna's overstress theory is used in the model described in this thesis to simulate viscoplasticity. The overstress function described by Perzyna (1966) is given by

$$\left\langle \Phi\left(\mathrm{F}\right)\right\rangle = \begin{cases} \mathrm{F} \text{ if } \mathrm{F} > 0 \\ 0 \text{ if } \mathrm{F} \le 0 \end{cases} \tag{B.1}$$

where, the parameter $\mathrm{F} = f_d - f_s$ quantifies the amount of overstress (f_d and f_s are the dynamic and static yield surfaces, respectively).

Unlike the conventional single surface plasticity constitutive models, there is no static yield surface (f_s) in the modified Manzari-Dafalias two surface model adopted in this study. The yield surface can move in the stress space because of the kinematic hardening. In the cutting plane algorithm used in this thesis, the predicted stress can be associated with an imaginary dynamic yield surface f_d, and the static yield surface f_s is identical to the yield surface described in section 2.1.2. During yielding of the material, s the distance between the static and dynamic yield surfaces are identical to the value of the yield function given in equation (2.2). Therefore, $\mathrm{F} = f$ is used to define the overstress in this thesis.

Furthermore, because the over stress is only calculated during the viscoplastic correction loop when it has already verified that $f > 0$, the conditional definition with the Macaulay brackets $\langle\ \rangle$ is dropped so that equation (B.1) becomes

$$\langle \Phi \rangle = f \tag{B.2}$$

APPENDIX C - ERROR CONTROL ALGORITHM

The implementation of the constitutive model, described in chapter 2, in the finite element software includes an error control algorithm. The algorithm breaks the time step *dT* from the finite element software into smaller sub-steps before they are run through the cutting plane algorithm. Initially, the finite element software passes the values of stress and the hardening tensors (σ_{ij}^{t} and α_{ij}^{t}) at the current time (*t*) and a time step, *dt*, to the error control algorithm. The error control algorithm then passes σ_{ij}^{t} and α_{ij}^{t} to the cutting plane algorithm where the time step in the cutting plane algorithm, *dt*, is equal to the time step from the finite element software (i.e., in the first pass, *dt* = *dT*). The resulting values of stress and hardening are stored as $\sigma_{ij}^{(t+dt),\mathrm{I}}$ and $\alpha_{ij}^{(t+dt),\mathrm{I}}$. The error control algorithm then passes the original values of stress and hardening (σ_{ij}^{t} and α_{ij}^{t}) back to the cutting plane algorithm with a reduced time step of $dt/2$ producing the values $\sigma_{ij}^{t+dt/2}$ and $\alpha_{ij}^{t+dt/2}$. These values are again fed into the cutting plane algorithm with a time step of $dt/2$ producing results which are saved as $\sigma_{ij}^{(t+dt),\mathrm{II}}$ and $\alpha_{ij}^{(t+dt),\mathrm{II}}$. The calculation of these stresses by using cumulative half steps through the cutting plane algorithm is illustrated in Figure C.1.

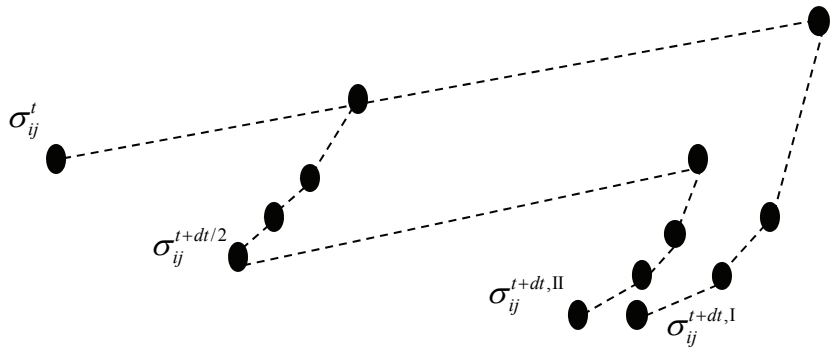

Figure C.1. Illustration of stress predictions using cumulative half steps in the cutting plane algorithm

Following Chapra and Canale (1998), the relative error can be calculated

$$ESNORM = \max\left(\frac{\left\|\sigma_{ij}^{(t+dt),\mathrm{II}} - \sigma_{ij}^{(t+dt),\mathrm{I}}\right\|}{\left\|\sigma_{ij}^{(t+dt),\mathrm{II}}\right\|}, \frac{\left\|\alpha_{ij}^{(t+dt),\mathrm{II}} - \alpha_{ij}^{(t+dt),\mathrm{I}}\right\|}{\left\|\alpha_{ij}^{(t+dt),\mathrm{II}}\right\|}\right) \tag{C.1}$$

If this relative error is less than a specified tolerance *STOL* (i.e., if *ESNORM* < *STOL*), then the step is accepted and the algorithm is complete. If the error is greater than the tolerance, then the step size *dt* is reduced and the error control algorithm enters an iterative loop. The time step is reduced following the equation

$$dt_{\text{new}} = \min\left(\frac{STOL}{ESNORM}, 0.8\right) dt_{\text{previous}} \tag{C.2}$$

The value of 0.8 is put in place to prevent the step size from being reduced too little in a step. Additionally, a lower limit of $(1.0 \times 10^{-6})dT$ is placed on dt_{new}.

With the new reduced value of *dt*, the cutting plane algorithm is again run to compare the solutions using one step with *dt* and two cumulative steps with *dt*/2 as described above and *ESNORM* is recalculated. If *ESNORM* is still greater than *STOL*, then the value of the time step is further reduced following equation (C.2). However, if

the calculated values of stress and hardening allow *ESNORM* to fall within the tolerance of *STOL*, then this iteration is accepted and the stresses and hardening tensors are saved.

It is necessary to introduce a pseudo time t_e to the error control algorithm. The time t_e is equal to the summation of the values of *dt* recorded from all the iterations in which *ESNORM* was within tolerance and the stress and hardening tensors were updated.

When the condition *ESNORM* < *STOL* is satisfied (i.e., when the chosen time step *dt* is sufficiently small), the subsequent time step may be increased for the next iteration using the following equation

$$dt_{\text{new}} = \min\left(\frac{STOL}{ESNORM} dt_{\text{previous}}, 1.1 dt_{\text{previous}}, dT - t_e \right) \tag{C.3}$$

where the new time step in the error control algorithm can increase based on the previous error levels, but not more than by 10%. Additionally, the new time step cannot be greater than the difference of the time step *dT* given by the finite element software and the summation of time steps t_e from the previously accepted iterations.

The error control algorithm iterates until the total time step *dT* from the finite element software is reached. A flow chart for the error control algorithm is presented in Figure C2.

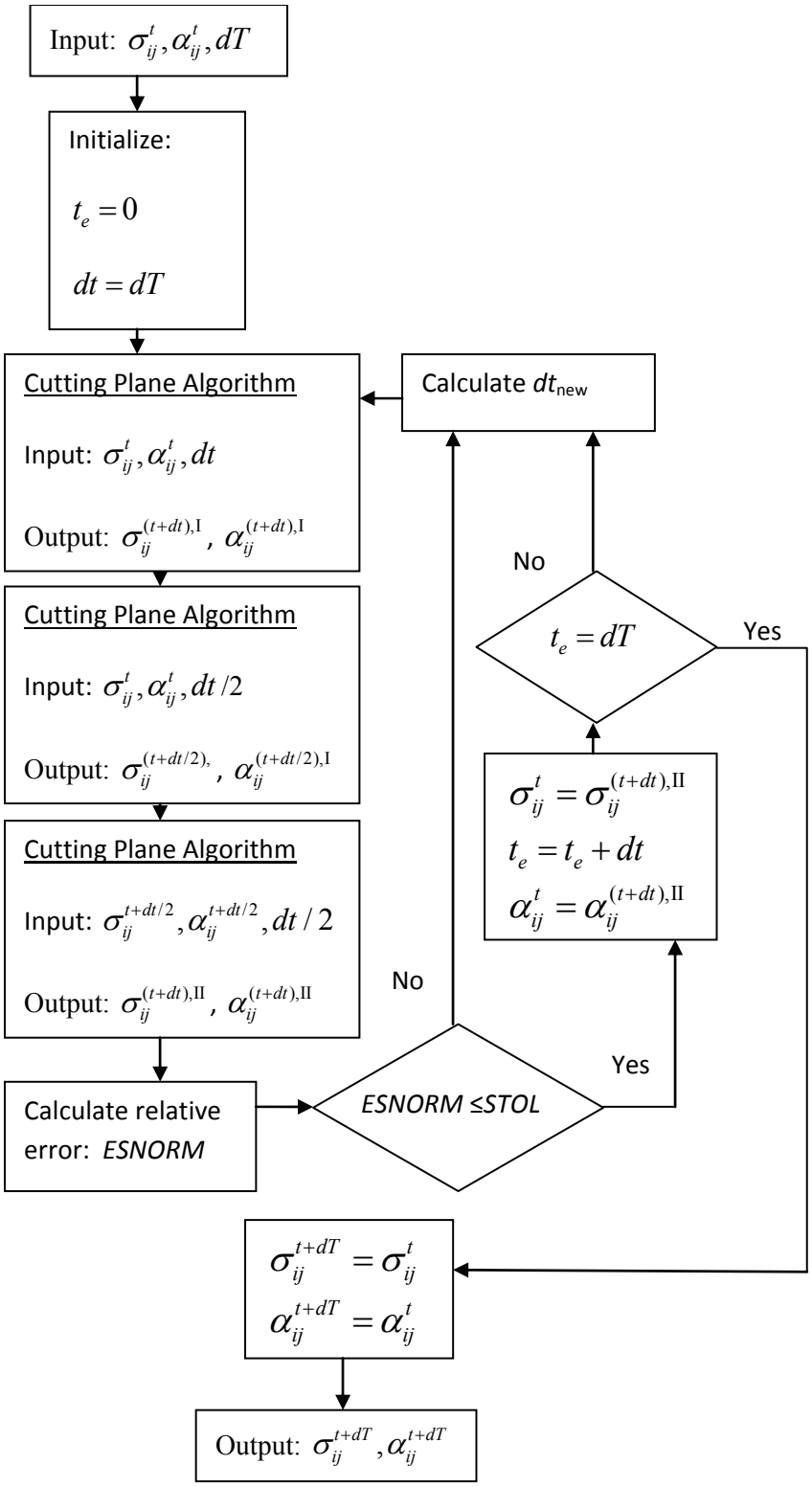

Figure C2. Flow chart for error control algorithm